

ORIGIN OF CARBONATE CEMENTS IN FLEMISH
BASIN UPPER JURASSIC SANDSTONE RESERVOIRS:
CONTROLS ON POROSITY DEVELOPMENT

Di Xiong

ABSTRACT

The Flemish Pass Basin is a deep-water basin located on the Grand Banks, eastern offshore Newfoundland, which is currently a hydrocarbon exploration target. Calcite cementation appears to act as an important controlling factor on reservoir quality in the Flemish Pass reservoir sandstones. This study investigates petrographic characteristics and the origin of carbonate cements in the Ti-3 Member, a primary clastic reservoir interval of the Bodhrán Formation (Upper Jurassic) in the Flemish Pass Basin.

The Ti-3 sandstones are quartzarenites to sublitharenites, and contain a high volume of poikilotopic (300-500 μ m) and minor fracture-filling (0.375-2mm) calcite cements. Grain contact features and high minus-cemented porosity (or intergranular volume, IGV) suggest that the calcite cements precipitated during an early stage of the diagenetic history. These cements postdate feldspar leaching and are followed by the corrosion of quartz grains. The intergranular calcite cements exhibit dull/moderate to bright luminescence under cathodoluminoscope. Intergranular calcite cements commonly host all-liquid inclusions mainly in the crystal core but rare primary two-phase (liquid and vapor) fluid inclusions have been observed in the rims of calcite cement grains and in the fracture-filling calcites. The primary two-phase fluid inclusions in the intergranular calcite have a mean homogenization temperature (T_h) of $70.2 \pm 4.9^\circ\text{C}$ and salinity estimates of 8.8 ± 1.2 eq. wt.% NaCl, while those in fracture-filling calcite have a higher mean T_h of $136.5 \pm 1.8^\circ\text{C}$ and salinity estimates of 10.0 ± 1.8 eq. wt.% NaCl. Fluid-inclusion gas ratios (CO_2/CH_4 and N_2/Ar) are consistent with diagenetic fluids that originated from modified seawater. The shale normalized REE (REE_{SN}) patterns of calcite cements are similar and exhibit slightly negative Ce anomalies. The mean $\delta^{18}\text{O}$ and $\delta^{13}\text{C}$ isotopic values of the intergranular calcite cement are $-8.3 \pm 1.2\text{‰}$, VPDB and $-3.0 \pm 1.3\text{‰}$, VPDB, respectively. The

fracture-filling calcites exhibit more depleted $\delta^{18}\text{O}$ but similar $\delta^{13}\text{C}$ isotopic ratios, with mean values of $-10.8 \pm 0.1\%$, VPDB and $-2.0 \pm 0.2\%$ VPDB, respectively. The Mn concentrations are generally higher than those of Fe and the Sr concentrations are normally over 1000ppm particularly for the intergranular calcite cements. Combined evidences from petrographic, microthermometric and geochemical analyses suggest that (1) the intergranular calcite cement precipitated from diagenetic fluids of mixed marine and meteoric waters in suboxic conditions; (2) this cement was sourced from the oxidation of organic matter and the dissolution of biogenic marine carbonates within sandstone beds or adjacent silty mudstones; and (3) the late phases of intergranular and the fracture-filling calcite cements were deposited from hot circulated basinal fluids.

Visual estimates of porosity from thin sections range from 1% to 28% and over 75% of initial porosity was lost due to the early calcite cementation. The reopening of secondary porosity (mostly moldic, enlarged pores) and throats by later calcite dissolution was the key process in improving the reservoir quality. Acidic fluids, released after the maturation of organic matter (e.g., hydrocarbon and coals), played a significant role in the porosity improvement.

ACKNOWLEDGEMENTS

I would like to express my greatest gratitude to my thesis supervisor Dr. Karem Azmy, who always encouraged and supported me with invaluable academic and professional guidance. I am also grateful for the financial support from Suncor Energy Inc. and Mitacs funding to Prof. Karem Azmy.

This study was not possible without technical supports from the people of the Core Research Equipment & Instrument Training (CREAIT) Network at Memorial University, including Glenn Piercey, Alison Pye and Helen Gillespie. Also, thanks to Nigel Blamey who helped to carry out the fluid-inclusion gas analyses. I would like to thank the people from Canada-Newfoundland and Labrador Offshore Petroleum Board (C-NLOPB) for their assistance in accessing well reports.

Finally, I would like to thank all my good friends who accompanied with me during two years, and my families for all their love and full support.

TABLE OF CONTENTS

ABSTRACT.....	II
ACKNOWLEDGEMENTS.....	IV
TABLE OF CONTENTS.....	V
LIST OF FIGURES	IX
LIST OF TABLES.....	XVI
CHAPTER I INTRODUCTION AND GEOLOGICAL SETTING.....	1
1.1 Introduction.....	1
1.2 Evolution of Mesozoic Offshore Newfoundland.....	3
1.3 Flemish Pass Basin	9
1.3.1 Location and Regional Geology	9
1.3.2 Tectonic and Geologic Evolution	11
1.3.3 Petrography and Diagenesis.....	14
1.3.4 Exploration Activity and Hydrocarbon Potential	16
CHAPTER II DATA COLLECTION AND METHODOLOGY.....	18
2.1 Introduction.....	18
2.2 Geological Information of Sampled Intervals.....	18
2.2.1 Mizzen F-09 Well	18

2.3 Methods.....	21
2.3.1 Optical Microscopy and Cathodoluminescence.....	21
2.3.2 Quantitative Mineral Liberation Analysis (MLA).....	22
2.3.4 Microthermometric Measurements.....	22
2.3.5 Fluid-Inclusion Gas Analysis.....	23
2.3.5 Stable C- and O- Isotopes	24
2.3.6 Minor and Rare Earth Elements.....	25
2.3.7 Porosity Loss Calculation.....	26
CHAPTER III RESULTS OF ANALYSIS ON Ti-3 SANDSTONES	27
3.1 Petrography.....	27
3.1.1 Quartz.....	30
3.1.2 Feldspar.....	30
3.1.3 Lithic Fragments	31
3.1.4 Accessory Minerals.....	31
3.1.4.1 Glauconite.....	31
3.1.4.2 Chlorite	32
3.1.4.3 Heavy Minerals.....	32
3.1.4.4 Carbonaceous Material	32

3.1.5 Bioclasts.....	33
3.1.6 Matrix.....	33
3.1.7 Authigenic Components.....	36
3.1.7.1 Carbonate Cement.....	36
3.1.7.2 Silica Cement.....	37
3.1.7.3 Pyrite.....	38
3.2 Microthermometry.....	38
3.3 Fluid-Inclusions Gas Ratios.....	47
3.4 Geochemistry.....	48
3.4.1 Oxygen and Carbon Isotopes.....	48
3.4.2 Minor and Rare Earth Element.....	49
CHAPTER IV DISCUSSION.....	53
4.1 Diagenesis and Paragenetic Sequence.....	53
4.1.1 Introduction.....	53
4.1.2 Quartz Overgrowth.....	54
4.1.3 Quartz Grain Corrosion.....	56
4.1.4 Calcite Cementation.....	57
4.1.5 Precipitation of pyrite and siderite.....	58

4.1.6 Precipitation of dolomite.....	60
4.1.7 Albitization of K-Feldspars.....	60
4.1.8 Dissolution.....	61
4.1.9 Compaction.....	61
4.2 Origin of Calcite Cement.....	62
4.2.1 Oxygen and Carbon Isotopes.....	63
4.2.2 Minor and Rear Earth Elements.....	70
4.2.3 Fluid-Inclusion Gas Analysis.....	74
4.3 Impacts on Sandstone Porosity.....	77
CHAPTER V CONCLUSIONS.....	80
REFERENCES.....	82
APPENDIX 1.....	110
APPENDIX 2.....	114
APPENDIX 3.....	117
APPENDIX 4.....	119
APPENDIX 5.....	121

LIST OF FIGURES

- Figure 1.1** Regional location and geological map of Mesozoic sedimentary basins and structures, eastern offshore Newfoundland. Yellow dashed line shows location of seismic-section in Figure 1.2 (modified from Tankard and Welsink 1989, Hesse and Abid 1998; Lowe et al., 2011).4
- Figure 1.2** West to east seismic-section across Jeanne d’Arc Basin, Central Ridge, Flemish Pass Basin, Beothuk Knoll, Flemish Graben and Flemish Cap showing Jeanne d’Arc Basin and Flemish Pass Basin separated by Central Ridge high formed at North Atlantic rift stage, and both basins confined to one main listric detachment fault and several syn-sedimentary faults. Te-Tertiary sequence, Cr-Cretaceous sequence, Jur-Jurassic sequence, Tr-Triassic sequence, BSM-Precambrian and Paleozoic basement (modified from Enachescu 1988).5
- Figure 1.3** Map showing three episodes of rifting events on the North Atlantic area. Rifting occurring in sequence oriented from south to north since the Mesozoic. Arrows demonstrate the orientations of each regional rifting event. First rifting phase (A) occurring during Late Triassic to Early Jurassic resulting in the break-up of North America and Africa at approximate 180 Ma. Second rifting phase (B) occurring during Late Jurassic- Early Cretaceous separating the Grand Banks from Iberia at approximate 120 Ma. Third rifting phase (C) occurring from late Early Cretaceous (Barremian-Albian) resulting in division of North Europe and North America at approximate 100 Ma (modified from Lowe, 2009).6

Figure 1.4 General regional stratigraphy and tectonics chart of the Jeanne d’Arc Basin showing the Jeanne d’Arc Formation, which is believed to be equivalent to the Ti-3 sandstones (modified from Sinclair, 1993).8

Figure 1.5 Tectono-structural subunits of the Flemish Pass Basin and approximate location of the Statoil Mizzen F-09 well (48°18’22.51” and W46°15’57”) (modified from Enachescu, 1987).10

Figure 1.6 Regional stratigraphy and syn-rift events of the Flemish Pass Basin. Four stratigraphic sequences have been documented and “S” represents the location of source rocks (modified from Foster and Robinson, 1993).12

Figure 1.7 Combined gamma-ray, lithologic, seismic markers, and stratigraphy for the Mizzen L-11 well. Red dots represent sample locations (modified from Lowe, 2009).15

Figure 2.1 Simplified stratigraphic framework for the Mizzen F-09 well showing the lithostratigraphy and the gamma-ray log of the Ti-3 Member (the Bodhrán Formation). Data acquired from Natural Resources Canada website (http://basin.gdr.nrcan.gc.ca/index_e.php) and Statoil Canada Resources (2011). ...19

Figure 3.1 QFR tenary diagram of sandstone petrography showing the composition of the Ti-3 sandstones Folk (1980). Q, quartz; F, feldspar; and R, rock fragments. Blue symbols represent results from MLA and red symbols are values based on visual estimates from thin-sections using conventional optical microscope.29

Figure 3.2 Photomicrographs of petrographic features of the Ti-3 sandstones. (a) Framework grains “floating” on the cement, Sample# 3342.6, polarized light, (b) enlarged pores, Sample# 3377.1, polarized light, (c) Moldic pore, Sample# 3382.8, polarized light, (d)

Point and line grain contact, Sample# 3377.9, polarized light, (e) Concavo-convex grain contact, Sample# 3389.6, crossed polars, and (f) Quartz exhibiting sweeping extinction, Sample# 3382.8, crossed polars.34

Figure 3.3 Photomicrographs of petrographic features of the Ti-3 sandstones. (a) Cathodoluminescence image showing bluish CL of some quartz grains (arrow), Sample# 3377.9, (b) Quartz showing pitted margin and embayment (arrow), Sample# 3382.8, crossed polars, (c) Quartz overgrowths (arrow), Sample# 3387.4, SEM, (d) Quartz overgrowths occurring in cemented interval, Sample# 3381.1, crossed polars, (e) Quartz replaced by calcite cement (arrow), Sample# 3386.5, crossed polars, and (f) Remnant feldspar exhibiting skeletal structure, Sample# 3382.8, SEM.35

Figure 3.4 Photomicrographs of petrographic features of the Ti-3 sandstones. (a) Feldspar showing partial dissolution and replacement by calcite cement. Sample# 3386.5, crossed polars, (b) Albitized K-feldspar engulfed by calcite cement (arrow), patchy albite in dark shades of grey and K-feldspar in light shades of grey, Sample# 3382.2, SEM, (c) Chert coated with micrite, Sample# 3382.2, crossed polars, (d) Sedimentary lithic fragment (arrow, possibly mudstone), Sample# 3357.7, polarized light, (e) Schist and metamorphic quartz, Sample# 3386.5, crossed polars, and (f) Siltstone, Sample# 3375.85, crossed polars.39

Figure 3.5 Photomicrographs of petrographic features of the Ti-3 sandstones. (a) Dolomite (arrow), Sample# 3382.8, SEM, (b) Ooid cored on quartz (arrow), Sample# 3382.8, crossed polars, (c) Deformed glaucinite (arrow), Sample# 3363.4, polarized light, (d) Chlorite (arrow), Sample# 3384.5, crossed polars, (e) Primary-origin chlorite-

muscovite matrix (arrow, possibly phyllite), Sample# 3387.8, crossed polars, and (f) Rutile growing with quartz, Sample# 3377.2, SEM.40

Figure 3.6 Photomicrographs of petrographic features of the Ti-3 sandstones. (a) Staurolite (arrow), Sample# 3386.5, crossed polars, (b) Wood tissue (arrow), Sample# 3357.2, polarized light, (c) Fossil fragments are recrystallized to calcite, Sample# 3382.8, crossed polars, (d) Radial ooid, Sample# 3381.1, polarized light, (e) Brachiopods, Sample# 3382.8, crossed polars, and (f) A transverse section of brachiopod showing dissolution, Sample# 3382.8, polarized light.41

Figure 3.7 Photomicrographs of petrographic features of the Ti-3 sandstones. (a) Algae (arrow), Sample# 3344.6, polarized light, (b) Lathy illite produced from altered feldspar filling pores (arrow), Sample# 3355.6, SEM, (c) Calcite cement stained dark red-purple, Sample# 3344.6, polarized light, (d) Twinning planes of calcite cements occurring uninterrupted on either side of grains, Sample# 3365.9, crossed polars, (e) Cathodoluminoscope image showing dull, to at times bright, CL of poikilotopic calcite cements, Sample# 3367.8, and (f) Spherulitic siderites (arrow) scattering on the poikilotopic calcite cement and on grain rims, Sample# 3385.7, polarized light.42

Figure 3.8 Photomicrographs of petrographic features of the Ti-3 sandstones. (a) Cathodoluminescence image of (Figure 3.7 f) showing dull CL of sediment components from cemented intervals containing siderite, Sample# 3385.7, (b) Minor fibrous and sparry calcite growing inside a bioclast (arrow), Sample# 3365.9, crossed polars, (c) Fracture-filling calcites, Sample# 3357.2, polarized light, (d) Dolomite rhomb scattering in interstitial spaces after calcite dissolution, Sample#

3348.6, polarized light, (e) Dolomite aggregates scattering in interstitial spaces after calcite dissolution, Sample# 3377.1, crossed polars, and (f) Minor dolomite on calcite cement remnants (arrow), Sample# 3387.8, polarized light.43

Figure 3.9 Photomicrographs of petrographic features of the Ti-3 sandstones. (a) Ankerite (arrow) seldom occurring as overgrowth of ferroan dolomite, Sample# 3387.4, SEM, (b) Spherulitic and subhedral pyrite replacing bioclasts, Sample# 3368.6, polarized light, (c) Late pyrite cements filling intergranular spaces Sample# 3355.6, polarized light, and (d) Late pyrite replacing calcite remnant, Sample# 3387.8, reflected light.44

Figure 3.10 Photomicrographs of primary fluid inclusions in a calcite cement from Ti-3 sandstones. Irregular-shaped mono-phase fluid inclusions likely occur in clusters (right), while rare two-phase fluid inclusions generally occur individually in the crystal rim (arrow).....46

Figure 3.11 Scatter diagrams of (a) Mn vs. Fe and (b) Mn vs. Sr for calcite cements.47

Figure 3.12 Shale-normalized (PAAS) REE patterns of calcite cements in the Ti-3 sandstones, Lennard Shelf cements reflecting seawater-like pattern (Nothdurft, 2004) and suspended load from modern river water reflecting fluvial input pattern (Goldstein and Jacobsen, 1988).50

Figure 4.1 Paragenetic sequence of the Ti-3 sandstones of the Bodhrán Formation based on petrographic relationships.55

Figure 4.2 Photomicrographs of petrographic features of the Ti-3 sandstones. (a) Bluish ultraviolet florescence (arrow) in calcite cement, Sample# 3367.8, (b) Siderites

growing into the corroded margin of detrital quartz, Sample# 3385.7, crossed polars, (c) Dissolution staining on the replaced cleavage planes of albitized K-feldspar, Sample# 3382.8, SEM, and (d) Calcite dissolution resulting in development of secondary pores, Sample# 3382.8, crossed polars.59

Figure 4.3 Photomicrographs of petrographic features of the Ti-3 sandstones. (a) Cement remnant, Sample# 3339.3, polarized light, (b) Microcracks occurring in quartz grains, Sample# 3387.8, crossed polars, (c) Quartz fracture healed by calcite cement (arrow), Sample# 3379.7, crossed polars, and (d) Sutured grain contact, Sample# 3382.8, crossed polars.62

Figure 4.4 Phanerozoic $\delta^{18}\text{O}$ trend of well-preserved marine biogenic carbonates. An estimated range of $\delta^{18}\text{O}$ of -1.5 to -0.5‰ VPDB during the Tithonian. The outlining area around the mean include 68% of all data (modified from Veizer et al., 1999).64

Figure 4.5 Scatter diagram of $\delta^{18}\text{O}$ vs. $\delta^{13}\text{C}$ for calcite cements. The square represents the estimated range of isotopic composition of well-preserved marine carbonates during the Tithonian Stage (Veizer et al., 1999).66

Figure 4.6 Temperature (T) vs. $\delta^{18}\text{O}_{\text{digenetic fluid}}$ for various $\delta^{18}\text{O}_{\text{calcite}}$ values that were reconstructed from the following equation: $10^3 \ln \alpha_{(\text{calcite-water})} = 2.78 \cdot 10^6 T^{-2} - 2.89$ (Friedman and O'Neil, 1977). The vertical bars indicate the $\delta^{18}\text{O}_{\text{fluid}}$ compositions based on the ranges of $\delta^{18}\text{O}_{\text{calcite}}$ values and homogenization Temperature (T_h) of each identified calcite cement phase. Details in text. Field A refers to the early

intergranular poikilotopic calcite and B to the late and fracture-filling calcite.	68
Figure 4.7 Schematic diagram summarizing the stages of formation of fluid inclusions in the calcite cements of the investigated sandstones. All-liquid fluid inclusions occur in the cores of poikilotopic calcite that precipitated at shallow burial, while liquid-vapor fluid inclusions form later in the crystal rims with progressive burial.	69
Figure 4.8 Phanerozoic $\delta^{13}\text{C}$ trend of well-preserved marine biogenic carbonates. An estimated range of $\delta^{13}\text{C}$ of 1.5 to 2.5‰ VPDB during Tithonian. The outlining area around the mean include 68% of all data (modified from Veizer et al., 1999).	71
Figure 4.9 Plot of CO_2/CH_4 vs. N_2/Ar for gas-inclusion analyses of the intergranular calcite cements from the Ti-3 sandstones (modified from Norman and Moore, 1999).	76
Figure 4.10 Diagram showing the intergranular volume vs. calcite cement volume in the Ti-3 sandstones, modified from Lundegard (1992).	77
Figure 4.11 Diagram showing the relationship between porosity distribution in sandstones intervals and calcite-cemented zones. The gray bar represents intervals with calcite cements over 30%. The porosity data are acquired from Natural Resources Canada website (http://basin.gdr.nrcan.gc.ca/index_e.php).	79

LIST OF TABLES

Table 3.1 Mineralogic composition (%) of the Ti-3 sandstones determined by the MLA.	27
Table 3.2 Heavy mineral composition (%) of the Ti-3 sandstones determined by the MLA.	33
Table 3.3 Statistics of microthermometric measurements of calcite cements in the Ti-3 sandstones.	45
Table 3.4 The weighted mean values of fluid-inclusion gas from sandstone samples with high volume of calcite cements by the incremental crush method. The ratios of N ₂ /Ar and CO ₂ /CH ₄ of quartz are proposed by Blamey et al (2014).	46
Table 3.5 Stable carbon and oxygen isotopic data of calcite cements. The V1, V2, and V3 values refer to measurements of fracture-filling calcites.	48
Table 3.6 Statistics of minor and rare earth element (REE) contents of calcite cements. The REE values of seawater from Nothdurft (2004) and those of river water from Goldstein and Jacobsen (1988) are also included. The Ce anomaly (Ce/Ce*) values were calculated based on the equation $Ce/Ce^* = 3(Ce/Ce_{shale}) / [(2La/La_{shale}) + (Nd/Nd_{shale})]$ of de Baar et al (1985).	51

CHAPTER I

INTRODUCTION AND GEOLOGICAL SETTING

1.1 Introduction

The Upper Jurassic sandstones of the Flemish Pass Basin is a part of a half graben bathymetric basin, located approximately 485 km northeast of St. John's, offshore Newfoundland. The basin was formed by continuous regional rifts during the break-up of North America and Africa in the Late Jurassic to Early Cretaceous, and is bounded by several syn-rift faults.

Hydrocarbon exploration in the Flemish Pass Basin began in the 1980s but, due to great water depth (400-1000m), it did not attract much exploration interest. However, with the improvement of industrial technology, deep-water drilling in the Flemish Pass Basin has become possible. Currently, the basin is a target area of hydrocarbon exploration. Unlike the adjacent prolific Jeanne d'Arc Basin, provenance, orientations, correlations, lateral reservoir quality variations and other depositional constraints of sandstones in the deep-water Flemish Pass Basin have been poorly elucidated until recently. Although a numbers of papers have been published on aspects of the geology of the Flemish Pass Basin (e.g., Foster and Robinson, 1993; DeSilva, 1999; Enachescu et al., 2005; Lowe et al., 2011; McDonough et al., 2011); little has been constrained on the timing, the geochemical conditions of precipitation and dissolution, or the sources of carbonate cements found in the Tithonian Ti-3 clastic reservoirs (informal name).

Abundant calcite cements have been recognized in the investigated core (Mizzen F-09) and act as main impediment to reservoir quality in the Flemish Pass sandstones (e.g., Haynes et al., 2013). Calcite cement has been suggested to be one of the dominant components during

diagenesis—filling in the pore spaces or being dissolved to form secondary porosity—and hence can be used to evaluate the reservoir quality of sandstone sequences (Bjørlykke et al., 1989; Hayes and Boles, 1993; Chowdhury and Noble, 1996). Therefore, unraveling the origin of cements is significant for better understanding and predicting porosity distribution and the overall diagenetic history of clastic reservoirs, which may assist in future hydrocarbon exploration and production.

The main objectives of this study are as follows:

- To identify the petrographic characterization and diagenetic evolution of sandstones in Flemish Pass Basin;
- To investigate and reconstruct the paragenetic sequence of multiple diagenetic events;
- To elucidate the origin and diagenetic environment of carbonate cements and their influence on porosity development and distribution.

Late Jurassic sandstones from Mizzen F-09 well were investigated in the current study. In order to interpret the burial history of cement in the Flemish Pass Basin sandstones, multiple techniques will be applied in the research. Examination of samples under the optical microscope, cathodoluminescence (CL) and scanning electron microscopy (SEM) provides fundamental petrologic and diagenetic information to reconstruct a paragenetic sequence and depict the evolution of porosity. Microthermometric (measuring homogenization and ice melting temperatures in fluid inclusions) and geochemical (minor and rare earth elements values, carbon and oxygen isotope values) studies as well as fluid-inclusion gas ratios yield abundant information on the diagenetic environment and are used to interpret the origin of carbonate cements.

1.2 Evolution of Mesozoic Offshore Newfoundland

The east coast of Newfoundland formed as a passive continental margin during the Mesozoic separation of Pangaea and the subsequent spreading of the Atlantic (Figure 1.1). The intracontinental double-failed rift arm produced a series of variably interconnected syn-rift basins spanning from Late Triassic to Late Cretaceous and corresponding to extensional and thermal subsidence stages (Enachescu, 1987, 1988; Tankard and Welsink, 1989; Foster and Robinson, 1993; Sinclair, 1993). These half-graben basins are confined to down-to-the-east basin bounding fault (Murre\Mercury fault) associated with antithetic and synthetic faults, and separated by pre-Mesozoic basement highs (Figure 1.2). The tectonic activity is subdivided into three major rift stages accompanied with salt tectonics, and with variable rates of deposition and erosion (Enachescu, 1987; Sinclair, 1988).

Three episodes of rifting events include (1) Late Triassic-Early Jurassic rift episode (the Tethys rifting stage); (2) Late Jurassic- Early Cretaceous rift episode (the North Atlantic rifting stage); and (3) Barremian – Albian rift episodes (the Labrador Sea rifting stage). The initial rifting phase (Late Triassic to Early Jurassic) resulted in the break-up of North America and Africa; the second rifting phase (Late Jurassic to Early Cretaceous) recorded the separation of the Grand Banks from Iberia; and the last rifting episode (Early Cretaceous, Barremian-Albian) involved the division of North Europe craton from Canada and propagation in Labrador Sea (Figure 1.3).

During the first rifting episode, syn-rift subsidence consisted of Triassic early continental red beds and evaporites overlying pre-rift metasedimentary basement. Early to Middle Jurassic post-rift strata are composed of carbonates and substantial fine-grained clastics, followed by

organic-rich carbonaceous shales of Kimmeridgian Egret Member (Late Jurassic), which are deemed to be key source rocks.

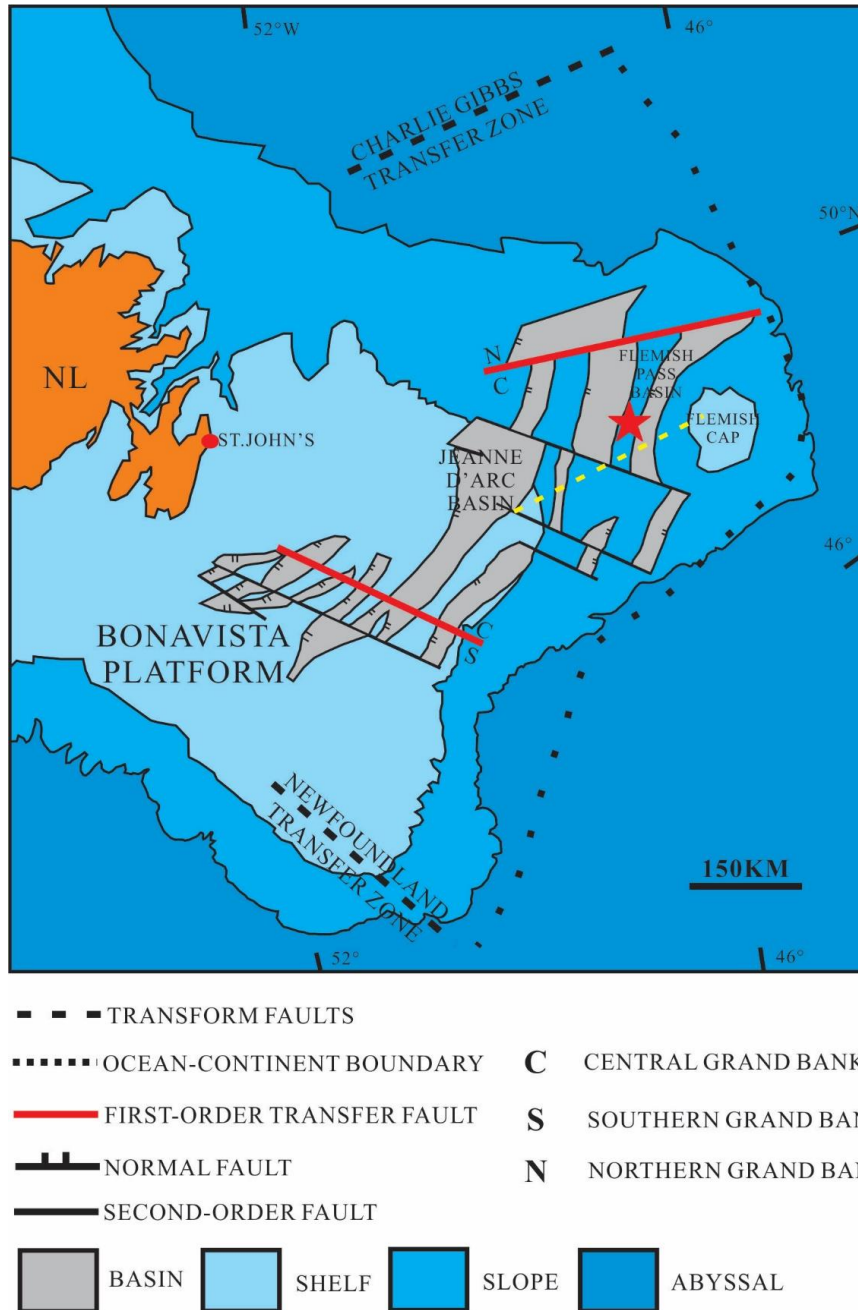


Figure 1.1: Regional location and geological map of Mesozoic sedimentary basins and structures, eastern offshore Newfoundland. Red star shows the location of the Flemish Pass Basin. Yellow dashed line shows location of seismic-section in Figure 1.2 (modified from Tankard and Welsink 1989, Hesse and Abid 1998; Lowe et al., 2011).

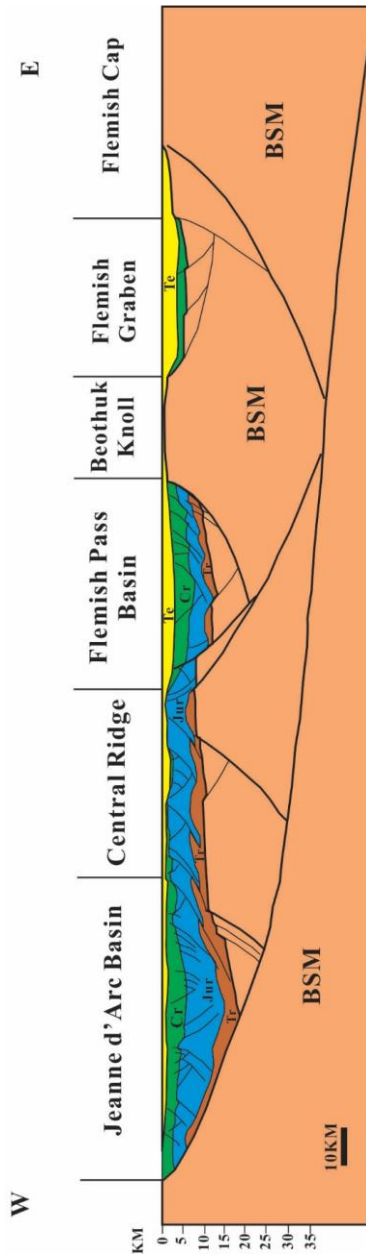


Figure 1.2: Interpretation based on a west to east seismic-section across Jeanne d'Arc Basin, Central Ridge, Flemish Pass Basin, Beothuk Knoll, Flemish Graben and Flemish Cap showing Jeanne d'Arc Basin and Flemish Pass Basin separated by Central Ridge high formed at North Atlantic rift stage, and both basins confined to one main listric detachment fault and several syn-sedimentary faults. Te-Tertiary sequence, Cr-Cretaceous sequence, Jur-Jurassic sequence, Tr-Triassic sequence, BSM-Precambrian and Paleozoic basement (modified from Enachescu 1988).

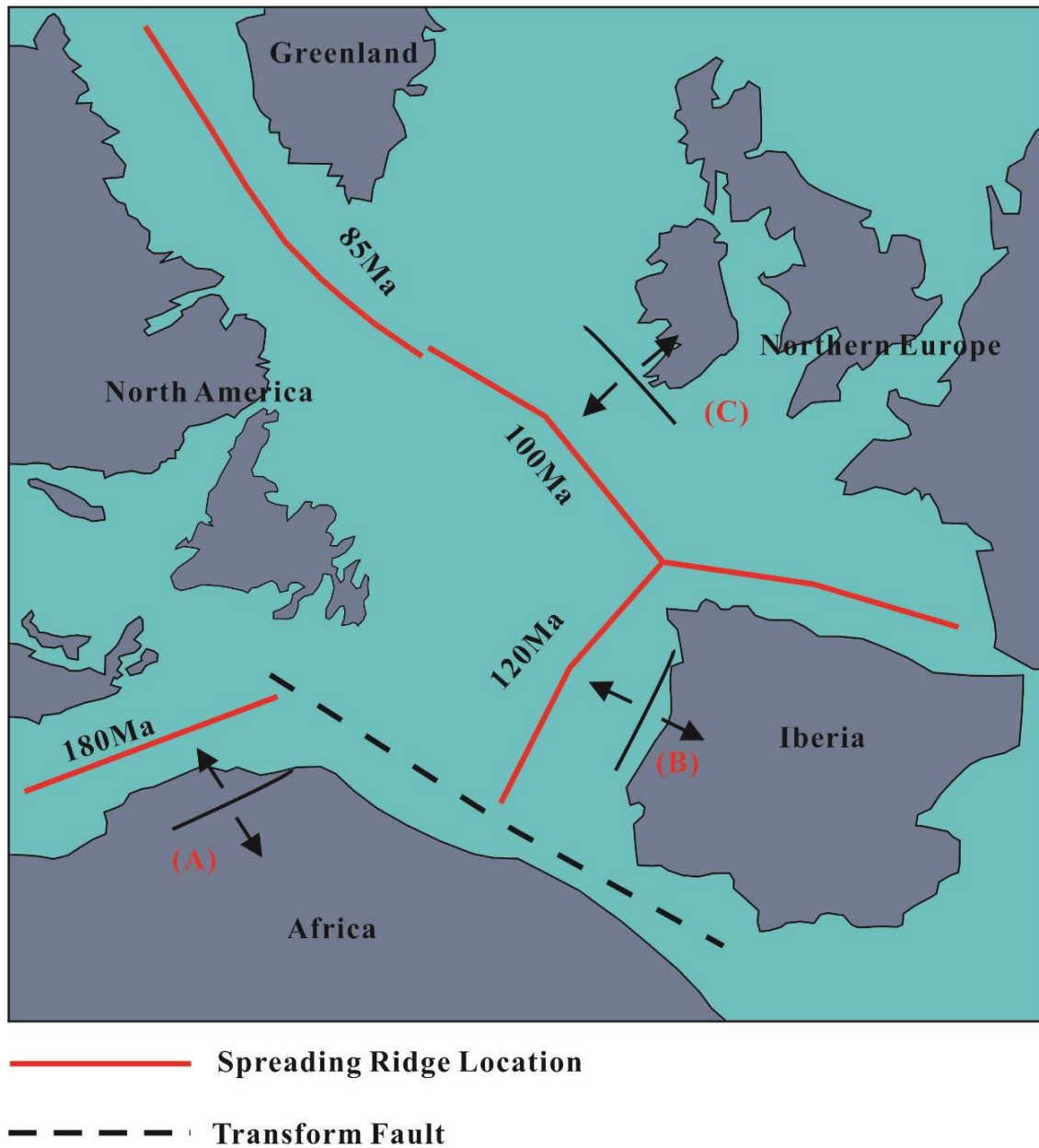


Figure 1.3: Map showing three episodes of rifting events on the North Atlantic area. Rifting occurring in sequence oriented from south to north since the Mesozoic. Arrows demonstrate the orientations of each regional rifting event. First rifting phase (A) occurring during Late Triassic to Early Jurassic resulting in the break-up of North America and Africa at approximate 180 Ma. Second rifting phase (B) occurring during Late Jurassic- Early Cretaceous separating the Grand Banks from Iberia at approximate 120 Ma. Third rifting phase (C) occurring from late Early Cretaceous (Barremian-Albian) resulting in division of North Europe and North America at approximate 100 Ma (modified from Lowe, 2009).

During the last two rifting episodes, a transgressive –regressive sedimentary sequence generally record a shift from terrestrial to marginal marine clastics, which include fluvial-deltaic and shallow marine sandstones that constitute the main petroleum reservoirs. The post-rift sedimentary subsidence after the Late Cretaceous comprises of deep-water shales with intermittent continental margin siliciclastics (Enachescu, 1987; Tankard and Welsink, 1989; McApline, 1990; Sinclair, 1993). These three rifting stages are associated with repeated subsidence and uplift, which resulted in the formation of the Grand Banks (Enachescu, 1987).

The Jeanne d’Arc Basin, a prolific hydrocarbon producing area with a maximum sediment thickness of approximately 20 km, is located on the edge of the Grand Banks (Fig 1.1). It has been extensively studied since 1970s (e.g. Enachescu, 1987, 1988; Tankard and Welsink, 1989; Brown et al., 1989; Sinclair, 1993, 1995; Pemberton et al., 2003; Magoon et al, 2005). The basin inherits integrated syn-rift successions due to the relatively stable subsidence through the continental rift stages and the constraining of the main listric fault (Enachescu, 1987; Enachescu and Hogg, 2005). It hosts four major offshore fields (Hibernia, Terra Nova, Hebron and White Rose) with petroleum reserves and resources of over 2 billion barrels of oil and over 5 trillion cubic feet of gas (C-NLOPB, 2014). Enachescu (1987, 2005) and Foster and Robinson (1993) indicated that Jeanne d’Arc and Flemish Pass basins are the two main basins of the northeastern Newfoundland continental margin sharing common tectonic activity and stratigraphic synchronism. Thus, the geological setting of the Jeanne d’Arc Basin has likely potential analogues in other syn-rift basins scattering along the offshore Newfoundland margin (Figure 1.4).

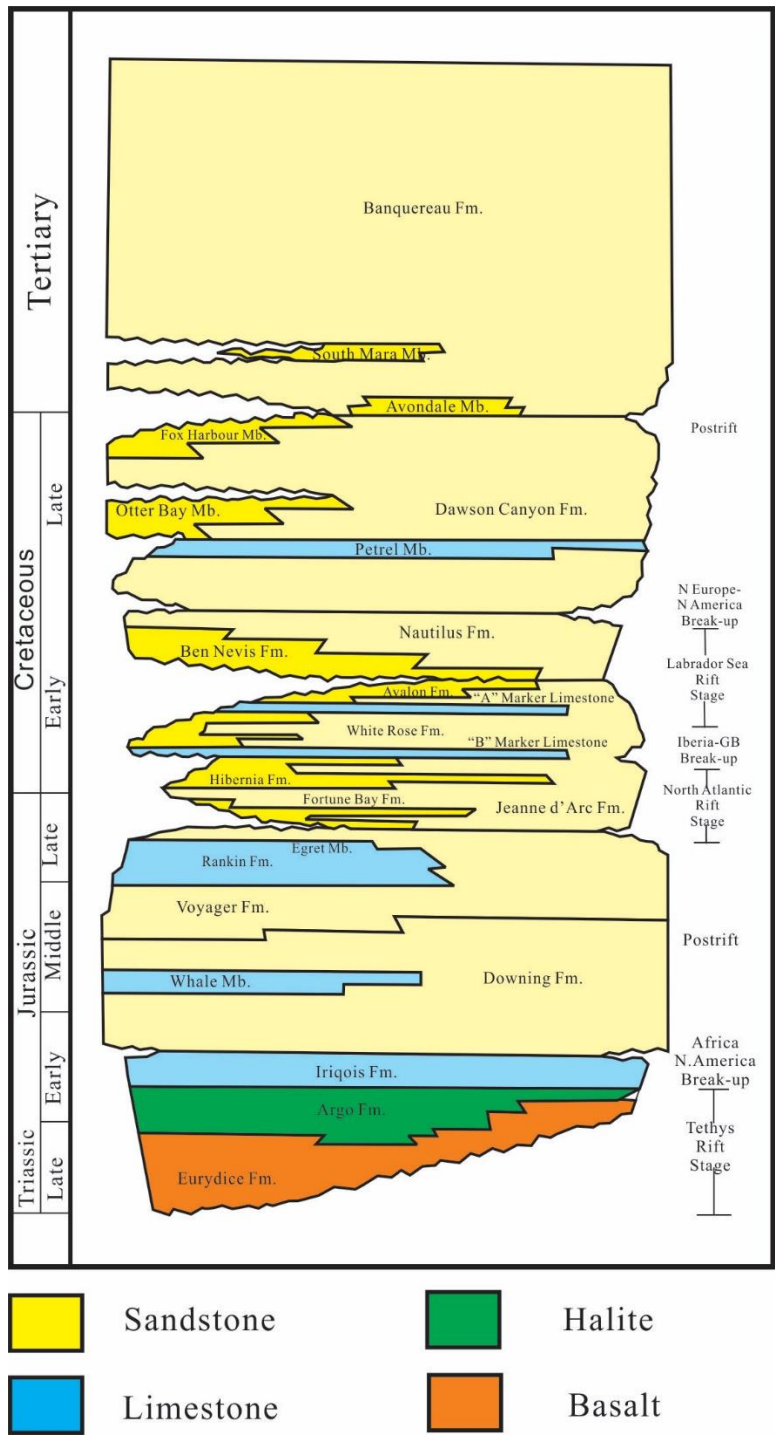


Figure 1.4: General regional stratigraphy and tectonics chart of the Jeanne d'Arc Basin showing the Jeanne d'Arc Formation, which is believed to be equivalent to the Ti-3 sandstones (modified from Sinclair, 1993).

1.3 Flemish Pass Basin

1.3.1 Location and Regional Geology

The Flemish Pass Basin is a half-graben bathymetric basin, situated approximately 485 km east of St. John's, Newfoundland, which formed during the Late Triassic to Early Cretaceous on the continental passive margin of the Grand Banks (Figure 1.1). It is bounded by the grand listric fault (Murre\Mercury) with a series of transform faults (Figure 1.2). It covers about 30,000 km² where present-day water depths range from 400 to 1,100 m (Foster and Robinson, 1993; DeSilva, 2000; Huppertz and Piper, 2009; Lowe, 2009). The Flemish Pass Basin is believed to be the outer part of "the double-failed rift" (Enachescu, 1988). Structurally, it is bounded to the east by the basement high of Flemish Cap and Beothuk Knoll, to the north by the Cumberland Ridge, to the south by the Avalon Uplift, and separated from the Jeanne d'Arc Basin to the southwest by the Central Ridge (Enachescu, 1987; Foster and Robinson, 1993). The Sackville Spur, a Late Cenozoic sediment drift, extends from the north-easternmost Grand Banks slope down onto the basin floor of Flemish Pass (Kennard et al., 1990). The Flemish Pass Basin is divided into two depocenters, the Baccalieu subbasin in the north and the Gabriel subbasin in the south (Figure 1.5; DeSilva, 1999). Similar to the Jeane d'Arc Basin, the Flemish Pass Basin turned into an active depocentre of siliciclastics during Later Jurassic to Early Cretaceous, and these are considered main reservoir rocks. The input of siliciclastic materials was controlled by the paleodrainage system and syn-deposition communication between basins and mainly influenced by the orientations of basement platforms (Tankard and Welsink, 1989; McAlpine, 1990; Sinclair, 1993; Enachescu et al., 2005). Lowe et al (2011) discussed the provenance of Late Jurassic and Early Cretaceous sandstones in Flemish Pass Basin and suggested that coarse sandstones were transported into the basin from west-northwest during the North Atlantic rifting

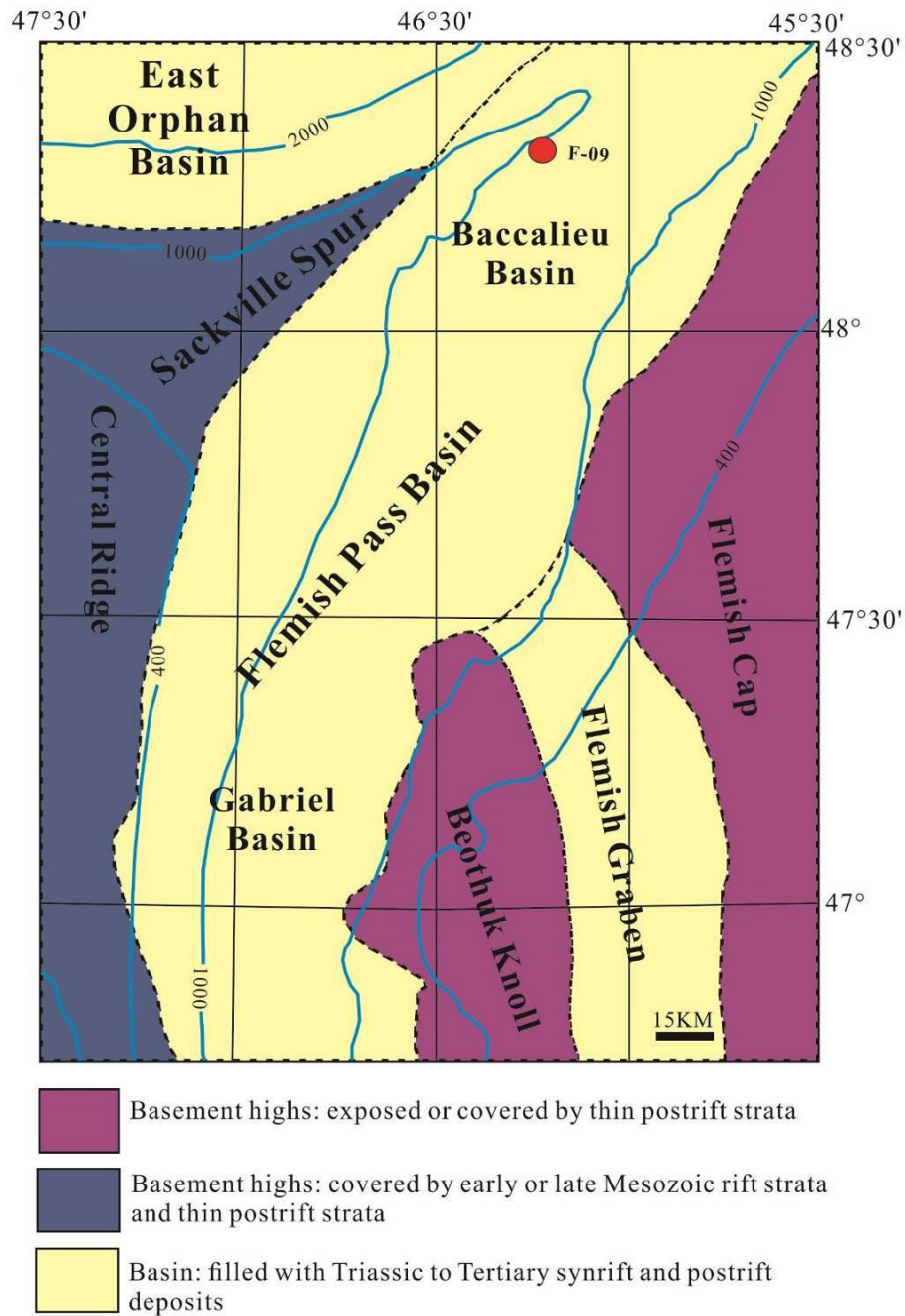


Figure 1.5: Tectono-structural subunits of the Flemish Pass Basin and approximate location of the Statoil Mizzen F-09 well (48°18'22.51" and W46°15'57") (modified from Enachescu, 1987).

stage, with the thickest accumulations in the west-northwest basin margin, and with decreasing reservoir grade toward the east,. Various sedimentary environments have been documented in the

Flemish Pass sandstones, including fluvial, shallow marine and submarine fan (DeSilva, 2000, Haynes et al., 2013).

1.3.2 Tectonic and Geologic Evolution

Foster and Robinson (1993) described the geologic evolution of the Flemish Pass Basin in details based on seismic data from seven exploration wells drilled during 1980s. The following section includes a summary of their study. The summarized stratigraphy of the Mesozoic syn-rift and post-rift sedimentary sequence is shown in Figure 1.6.

The geological history of the Flemish Pass Basin shows four megasequences from the Mesozoic to recent sediments (Foster and Robinson, 1993). These include (1) Upper Triassic (?) to Lower Berriasian megasequence (MS1); (2) Lower Berriasian to Aptian megasequence (MS2); (3) Aptian to Albian megasequence (MS3); and (4) Albian to Holocene megasequence (PR). The first three sequences occurred in fault-bounded depocentres with a change in orientation. During the Late Jurassic to Early Cretaceous rifting period, most of syn-rift sediments were deposited into the Baccalieu and Gabriel subbasins, which are located in the north and south of the Flemish Pass Basin, respectively (Foster and Robinson, 1993).

The base of MS1 (Late Triassic to Berriasian sediments) is defined by a regional unconformity overlain by Lower Cretaceous sediments and probable evaporites equivalent to those elsewhere along the margin of North Atlantic. The top of MS1 is marked by a regional non-erosional unconformity. Due to the depth of the MS1 sediments and poor resolution in seismic data, the lower part of this sequence is hard to identify. However, it shares similar characteristics (e.g., the Lower Jurassic evaporites, dolomites of Argo and Iroquois formations and mudstone of Pliensbachian-Callovian Downing formation) to those of the adjacent Jeanne d'Arc Basin (Foster and Robinson, 1993).

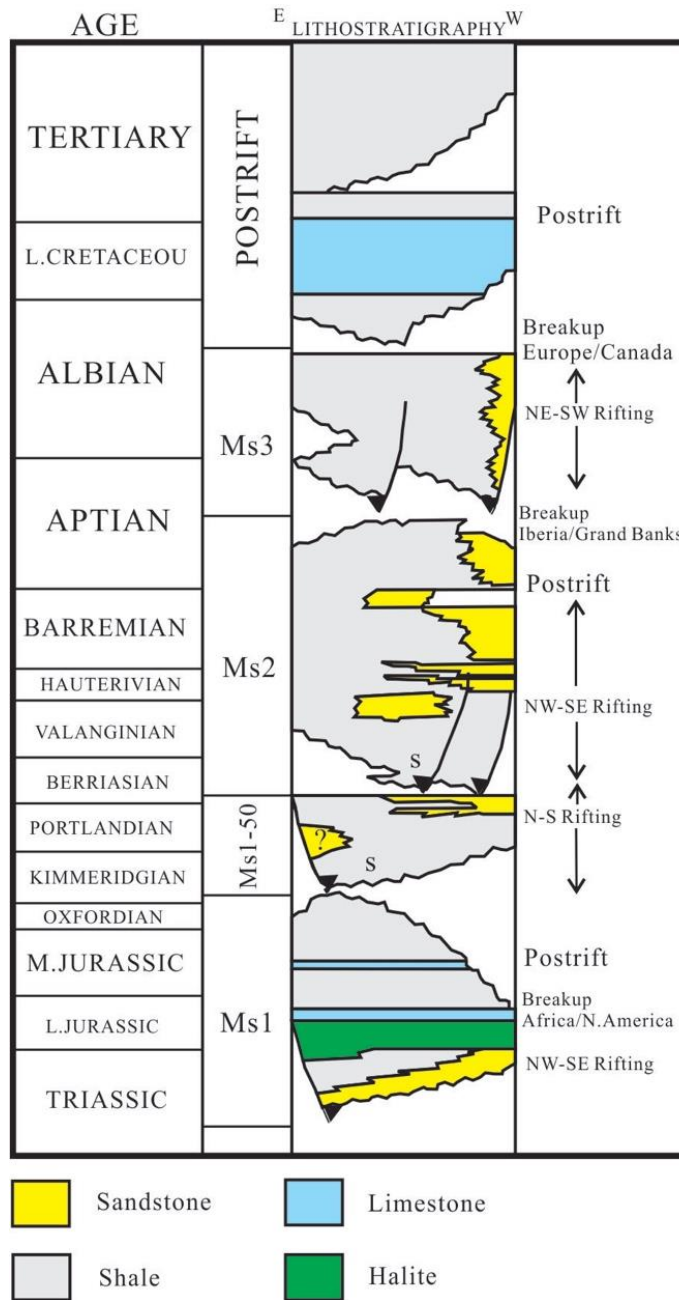


Figure 1.6: Regional stratigraphy and syn-rift events of the Flemish Pass Basin. Four stratigraphic sequences have been documented and “S” represents the location of source rocks (modified from Foster and Robinson, 1993).

The upper sedimentary section of MS1 (referred as MS1-50 from Kimmeridgian to Berriasian) is well defined by seismic mapping. MS1-50 is identified in the well Baccalieu I-78,

where the sedimentary facies reflect a shoaling from marine, shallow-marine or shoreline facies at the base to non-marine facies at the top (Lowe et al., 2009). A similar upward change from marine to shallow marine facies is also found in other wells (Foster and Robinson, 1993). Sediments were generally deposited in two east-west-directed subbasins separated by a structure high. The transgressive post-rift sediments overlap on the Kimmeridgian unconformity towards the south and east in the Baccalieu subbasin, and towards the northeast in the Gabriel subbasin, and this marks the base of MS1-50. The top of MS1-50 is a predominant sandy interval, overlain by mudstone rich in marine microfauna (Foster and Robinson, 1993). Earlier geochemical studies indicated that source rocks occur in lower part of MS1-50 sequence (Foster and Robinson, 1993).

MS2 deposits range in age from Lower Berrasian to Aptian, and extend approximately northeast- southwest where bounded by active southeastern boundary faults. The base of MS2 is marked by an unconformity correlated with regional subsidence and the top is defined by another unconformity that records a rotation of basin direction from northeast-southwest to approximately northwest-southeast during the Labrador Sea rifting event. The thickest MS2 sediments appear in the Gabriel subbasin, where a lower parasequence of mudstones and turbidities is overlain by an upper parasequence of prograding coarse clastic wedges separated by high stand shale intervals, the sediments in the Baccalieu subbasin are fine grained and poorly sorted (Enachescu, 1987; Foster and Robison, 1993).

Due to the rotation that occurred at the end of the second parasequence, northwest-southeast trending depocentres and faults formed upon a major unconformity during Aptian to Albian in MS3. Sediments were mainly deposited in the previous high that separated the Baccalieu and Gabriel subbasins. The top of MS3 is marked by another unconformity analogous

to that known in the Jeanne d'Arc Basin. Because of the lack of available cores, sediments of MS3 are interpreted by seismic facies analysis (Foster and Robinson, 1993). The depocentres were filled with the onlap of deep marine mudstones and turbidite sandstones. A channelized zone in the northern Barralieu subbasin is identified as the main pathway of sediments (Foster and Robinson, 1993).

The previous three parasequences are associated with rifting and faulting events, while the last parasequence, PR (Albian to present), has post-rift deposits overlying an unconformity. The subsequences include an active progradation beginning with a clastic shelf from the northwest, mudstone with possible interbedded sandstones and present day shelf-slope (Foster and Robinson, 1993).

1.3.3 Petrography and Diagenesis

The provenance of the Flemish Pass Sandstones was studied by Lowe (2009). Three Tithonian clastic intervals of the well Mizzen L-11 were analyzed, two from “Jurassic sandstone” (informal name) and one from the overlying “Baccalieu sandstone” (informal name) (Figure 1.7). In general, the Jurassic sections are quartz-rich with small volumes of lithic fragments and feldspars. Sandstones are pervasively cemented by ferroan dolomite. The cements are suggested to be formed early before intensive compaction due to high intergranular volume (IGV, estimated at approximate 40%) and lack of signs of plastic deformed clay-rich lithic fragment or sutured grain contacts. Pores consist of primary intergranular, secondary grain-dissolution and intragranular dissolution types. Quartz overgrowths are rare in the cemented section, likely due to dolomite cementation, but are more common in the samples without early dolomite cementation. Some of the quartz overgrowths exhibit abraded edges and occur in the silica-inhibiting dolomite cements, indicating that host quartz grains were reworked and those

1.3.4 Exploration Activity and Hydrocarbon Potential

Unlike the Jeanne d'Arc Basin, the Flemish Pass Basin has not attracted intensive exploration due to iceberg drifting and deep water depth (~1100m). Seven exploration wells drilled during 1980s and only three wells, Gabriel C-60, Baccalieu I-78, and Kyle L-11 penetrated the Mesozoic syn-rift sediments (Foster and Robinson, 1993). Among these wells, Baccalieu I-78 drilled 164m of Kimmeridgian source rock with 2.2 to 3.6wt% TOC and a mean Hydrogen Index of 395 to 391 (DeSilva, 1999). Although Gabriel C-60 did not penetrate the Kimmeridgian interval, oil was found in core cuts in Lower Cretaceous sandstones. The geochemical signatures indicated that the oil was derived from Kimmeridgian source rocks, deposited in oxidizing environment (DeSilva, 2000). In 2003, Mizzen L-11 was drilled in the northern Baccalieu sub-basin, which encountered 5m non-commercial light oil pay in Late Jurassic sandstone ("Baccalieu" sandstone) equivalent to the Jeanne d' Arc Formation of the Jeanne d'Arc Basin (Hogg and Enachescu, 2007). High porosity-permeability sandstone reservoirs of Late Jurassic to Early Cretaceous were confirmed by Mizzen O-16 and F-09 wells. The discovery well Mizzen O-16 was drilled in 2009, which tested heavier oil (21-22° API) from Late Jurassic sandstones. The Mizzen F-09, a delineation well, intersected four good quality Tithonian reservoirs, but had water and residual oil (Enachescu, 2014). These wells were drilled in an area known as the Mizzen Field, which is located at the apex of a north-south striking fault-bounded oblique horst block (Grushchitz et al., 2013). The seal rocks of the Mizzen Field are marine Berriasian-Valaninian shales (Grushchitz et al., 2013; Enachescu and Geoph, 2014). The source rocks referred to Type- II-III in the Flemish Pass Basin (McCracken et al., 2000, 2001) and Haynes et al (2012) show that the interbedded shales in Tithonian reservoirs have 8-12% TOC.

In May 2004, the Canada-Newfoundland Offshore Petroleum Board (C-NLOPB) in association with the Geological Survey of Canada released a report estimating the undiscovered hydrocarbon resources in the Flemish Pass Basin, which highlighted the desirable Egret equivalent source rocks and good sandstone reservoirs (C-NLOPB, 2004). The potential of the recoverable petroleum resources in the basin are calculated at 1.7 billion barrels, with expected field sizes ranging from 44 to 528 million barrels (Hogg and Enachescu, 2007). Potential extensive structural traps of faulted extensional anticlines have been discovered by several industrial 3D seismic surveys (Hogg and Enachescu, 2007). In 2009, Statoil announced first oil discovery in Mizzen project, which is estimated to hold 100-200 million barrels of oil. The C-NLOPB called for petroleum exploration bids in one parcel located in the Baccalieu subbasin and a large regional seismic program led by Husky Energy has been in progress since 2012. Statoil had explored another two oil discoveries, Harpoon and Bay du Nord. Harpoon project is located 10 km southeast of Mizzen discovery showing a light, high-quality oil. Bay du Nord project is the third oil discovery in the Flemish Pass Basin with estimated 300-600 million barrels of recoverable light oil.

CHAPTER II

DATA COLLECTION AND METHODOLOGY

2.1 Introduction

A multi-technique approach was applied in the current study to investigate the diagenetic evolution of the Ti-3 sandstones in the Flemish Pass Basin. Samples were collected from sandstone intervals of one delineation well (Mizzen F-09). Subsequently, a series of petrographic and geochemical analyses focused on unravelling the origin of calcite cements and its impact on reservoir quality.

2.2 Geological Information of Sampled Intervals

The Upper Jurassic clastic intervals of the Mizzen F-09 were sampled for petrography, microthermometry and geochemical analyses in this research. The core was selected carefully to cover the Mesozoic syn-rift clastic sequences, which have been considered to be equivalent to hydrocarbon reservoirs in the adjacent Jeanne d'Arc Basin (DeSilva, 2000; Enachescu et al., 2005; Haynes et al., 2013). The geological information, including borehole log, general lithology, and lithostratigraphy, were obtained from industrial well reports associated with the websites of the Canada-Newfoundland and Labrador Offshore Petroleum Board and Natural Resources Canada, BASIN Database (Fig. 2.1; Statoil Canada Resources, 2011; C-NLOPB, 2014; Natural Resources Canada, 2014).

2.2.1 Mizzen F-09 Well

The Mizzen F-09 well ($48^{\circ}18'22.51''\text{N}$, $46^{\circ}15'57''\text{W}$) is a deep-water delineation well located on the northern flank of an oblique-slipped horst block, referred as the Mizzen structure, in the Baccalieu subbasin (Figure 1.5; Gruschwitz, et al., 2013). It was drilled in mid-2011 by

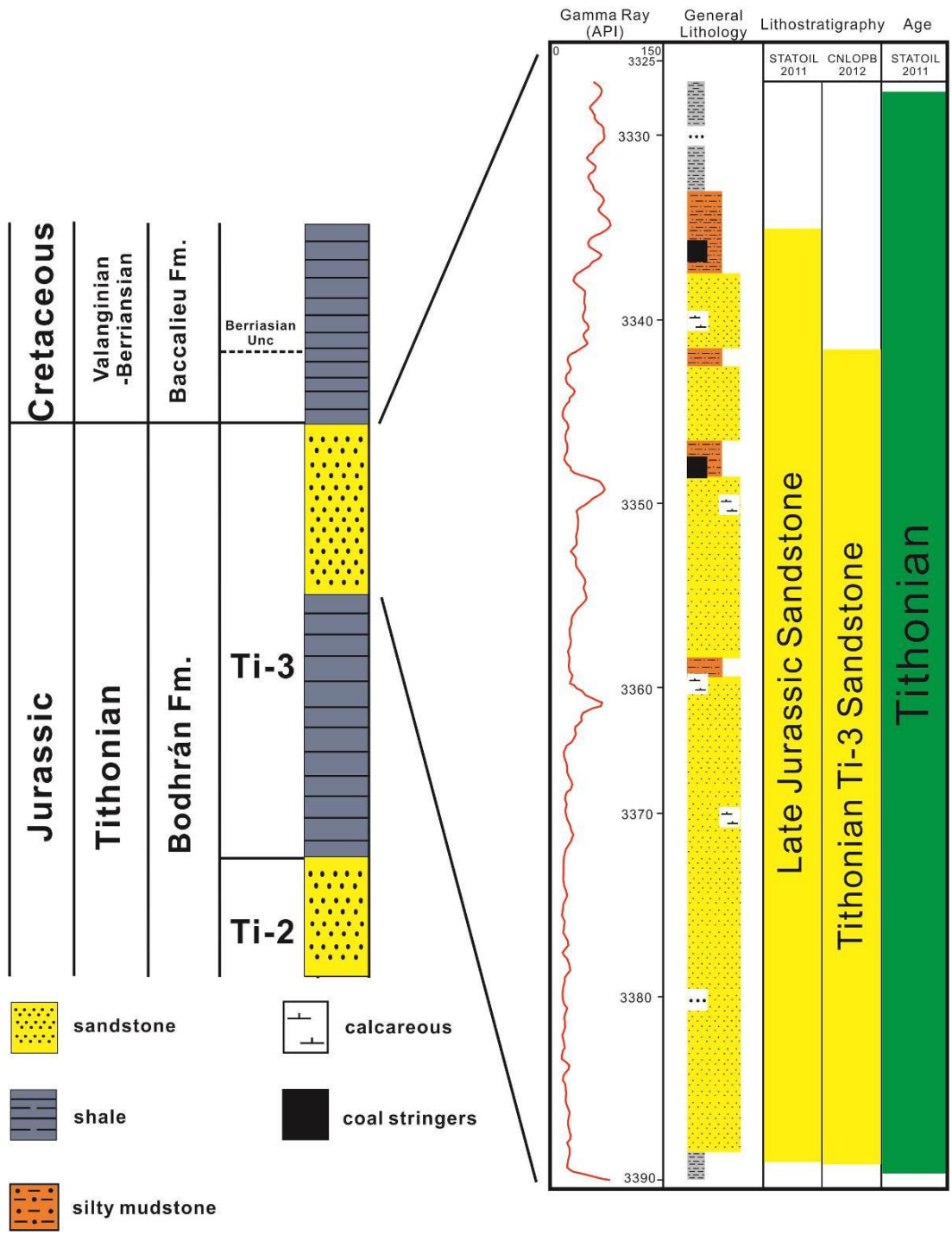


Figure 2.1: Simplified stratigraphic framework of the Mizzen F-09 well showing the lithostratigraphy and the gamma-ray log of the Ti-3 Member (the Bodhrán Formation). Data acquired from Natural Resources Canada website (http://basin.gdr.nrcan.gc.ca/index_e.php) and Statoil Canada Resources (2011).

Statoil Canada Ltd. and Husky Energy, encountered 1067m of seawater, to a total depth (TD) of 3762m and total vertical depth (TVD) of 3758.7m (C-NLOPB, 2014).

The well encountered good quality clastic reservoirs of the Upper Jurassic (Tithonian) Bodhrán Formation (informal name), which are chronologically and depositionally equivalent to the petroleum reservoirs of the Jeanne d'Arc Formation (Figure 2.1). It terminated in the Tithonian shale at 3762m, which has been considered to be the equivalent of source rocks in the Rankin Formation. Five informally named members (from base to top Ti-0 to To-4) of the Bodhrán Formation have been identified as potential reservoirs, among which the Ti-3 Member that has been deemed to be a primary reservoir interval (Haynes et al, 2013). The Ti-3 member represents a high net to gross ratio (over 75%) sandstone reservoir, with average porosities of >20% and average permeability of 1.2 Darcies (Haynes et al, 2013; Gruschwitz et al, 2013; C-NLOPB, 2014). However, pervasive carbonate cement has degraded the reservoir quality.

The Ti-3 Member has a thickness of approximately 60m (3389.95 to 3335.17m). It is underlain by lime mudstone above an erosional unconformity. The lithofacies, from bottom to top, include: well-sorted matrix-supported gravel to cobble conglomerate; fine to coarse-grained sandstone with isolated, well-rounded conglomerate and siltstone rip-up clasts; fine-to medium grained sandstone with occasional mudstone drapes and common carbonaceous laminae; and interbedded shale, siltstone and fine-grained sandstone (Haynes et al., 2013). The sedimentary facies of Ti-3 sandstone have been interpreted as syn-rift fluvial channel in the lower section and upper estuarine deposits, according to the general fining-upward hierarchy, predominantly unidirectional current flow sedimentary structures in the lower section, lower abundance of traceable bioclasts and the blocky nature of the gamma ray profile (Haynes et al, 2013; C-NLOPB, 2014).

2.3 Methods

In order to interpret the burial diagenesis history and origin of calcite cement in the Flemish Pass Basin sandstones, a multidisciplinary approach had been applied in this research. One hundred and ten core samples were collected from the Ti-3 sandstones of the borehole Mizzen F-09. Selected samples are focused on, but not limited to, sandstones with massive carbonate cements. All samples were thin sectioned for petrographic examinations. Mirror-image slabs from each thin section were polished and cleaned before microsampling and geochemical analyses. The thin sections were impregnated with blue epoxy to facilitate the identification of ore spaces (e.g., Blamey et al, 2014). They were also stained with Alizazin Red-S and postassium ferricyanide solutions to determine carbonates cement types (Lindholm and Finkelman, 1972). Petrographic analyses, by optical microscope, cathodoluminoscope, and scanning electron microscope (SEM), provide essential petrologic and diagenetic characterizations to reconstruct paragenetic sequence. The preliminary petrographic analysis and visual estimates of mineralogic composition allowed the selection of representative samples for the sophisticated MLA (Mineral Liberation Analysis). Microthermometric measurements and various geochemical analyses yielded information used to propose explanations for the diagenetic environment and the origin of calcite cement.

2.3.1 Optical Microscopy and Cathodoluminoscopy

Thin sections were examined under a Nikon Eclipse E600POL microscope with 4×, 10×, and 20× lenses to identify mineralogical composition as well as petrographic and diagenetic features, and to quantify cement and porosity contents. Photomicrographs were taken by an attached Nikon DXM 1200F digital camera.

Cathodoluminescent (CL), the visible radiation light emitted by minerals subjected to high-energy electron bombardment, is an important petrological technique. It provides valuable information about the cement phases and diagenetic history (Sippel, 1968). It is also an indispensable method to better understand cement history, distinguishing authentic silica overgrowths from detrital quartz grains and calcite cementation sequence (e.g., Sprunt and Nur, 1979; Machel and Burton, 1991). Cathodoluminescence has been widely used in studies of carbonate diagenesis (e.g., Burley et al., 1989; Machel and Burton, 1991; Machel 2000; Azomani et al., 2013; Olanipekun et al., 2014). Frank et al (1982) and Barnaby and Rimstidt (1989) proposed geochemical models and related Mn and Fe contents of cathodoluminescent calcite to particular potential redox conditions of precipitation. McLemore and Barker (1987) discussed the negative impact of volatilization in some organic-rich samples during CL examination that can also alter low-temperature fluid inclusions. In this study, cathodoluminescence (CL) was performed on polished thin sections to identify the cement generations by using a Technosyn cold cathodoluminoscope at about 12kv accelerating voltage and about 0.7mA current intensity.

2.3.2 Quantitative Mineral Liberation Analysis (MLA)

Six representative thin sections were prepared for quantitative mineral liberation analysis (MLA), which was conducted using the scanning electron microscope (SEM) facility at Memorial University of Newfoundland. The technique relies on backscattered electron imaging for distinguishing grain boundaries, and uses various x-ray emissions to classify grains of different minerals. This analysis yields precise results on mineral characteristics and contents.

2.3.4 Microthermometric Measurements

Much valuable data, such as pressure, temperatures and fluid compositions during burial history can be revealed by microthermometric analyses (Roedder, 1984; Goldstein and Reynolds,

1994; Goldstein, 2003; Bodnar, 2003). This analysis was conducted on double polished wafers using a Likhham THMSG 600 heating-freezing conjunction with an Olympus BX51 microscope. Calibration was done on a monthly basis using a CO₂ standard for -56.6°C whereas a water standard was used for ice melting at 0.0°C and the critical point at 374.1°C. Microthermometric measurements of homogenization temperature (T_h), initial melting temperature (T_i) and final melting temperature of ice ($T_m(\text{ice})$) of fluid inclusions were following procedures outlined by Shepherd et al. (1985). Aqueous fluid salinities were estimated using $T_m(\text{ice})$ and the equation modified by Bodnar (2003).

2.3.5 Fluid-Inclusion Gas Analysis

Inclusions may trap gases during diagenesis, which could to some extent reflect chemical compositions of the diagenetic fluids and burial environment (e.g., Blamey and Norman, 2002; Blamey, 2012; Azmy and Blamey, 2013). To determine fluid sources, a quantitative gas analysis of fluid inclusions was measured by the incremental crush fast scan method (e.g., Azmy and Blamey, 2013; Blamey et al, 2014) following procedures outlined in detail by Blamey (2012). Before analysis, thin sections were examined under ultraviolet light to exclude hydrocarbon contamination, which was performed using a CRAICQDI 202 UV unit mounted on a Zeiss imager D1m microscope. Selected samples were cleaned with alkaline solutions to remove surface organics, rinsed several times with deionized water and then dried at room temperature. Samples were crushed incrementally under a vacuum of $\sim 10^{-8}$ Torr producing 6 to 10 successive bursts. Data acquisition was carried out by means of two Pfeiffer Prisma quadrupole mass spectrometers (Blamey et al, 2014). Routinely the system analyses for the following: H₂, He, CH₄, H₂O, N₂, O₂, H₂S, Ar, CO₂, C₂H₄, C₂H₆, SO₂, C₃H₆, C₃H₈, C₄H₈, C₄H₁₀, and benzene (Blamey et al, 2014). The analysis was calibrated with commercial gas mixtures, in-housed fluid

inclusion gas standards as described by Norman and Blamey (2001). The concentration of each species is calculated by proprietary software to provide a quantitative analysis. Precision for the major gas species CO₂, CH₄, N₂, and Ar is better than 5% (Azmy and Blamey, 2013).

Blamey et al (2014) also performed separate crushes on quartz to clarify that initial crushes liberate exclusively calcite-hosted inclusions. Quartz grains were picked from calcite-dissolved sandstones and bulkly crushed under vacuum. The quartz fluid-inclusion gas weighted mean data shows a remarkably distinct high ratio of CO₂/CH₄ (96.8; Blamey et al., 2014) compared with that from calcite cement. Blamey et al (2014) proposed that incremental crushing releases gases from the soft and easily cleaved calcite before the hard quartz, so the quartz contamination is not a problem.

2.3.5 Stable C- and O- Isotopes

Stable isotope analysis is an essential tool for understanding the diagenetic history of carbonate cements. In the current study, stable isotopes were utilized to better understand the origin of the calcite cement and the variations in the diagenetic environments with progressive burial.

For C- and O-isotope analyses, the contents of calcite cement in the selected samples were evaluated based on visual estimates from the thin sections. Polished slabs were cleaned with deionized water and dried preparing for microdrilling. About 0.8 mg to 2.5 mg microsamples of calcite cement were drilled from each corresponding mirror-image slabs by a low-speed microdrill. The weighed powder samples were collected in the glass vials, and then reacted in inert atmosphere (He) with ultrapure orthophosphoric acid at 50°C in the Thermo-Finnigan Gas bench II. The CO₂ extracted from samples was carried by helium through chromatographic column and transferred to Thermo Finnigan DELTA V Plus isotope ratio mass spectrometer, in

which the gas was ionized and measured for isotopic ratios. Analytical errors of better than 0.1‰ (2σ) for the analyses were determined by repeated measurements of CBM ($\delta^{18}\text{O} = -8.58\text{‰}$ and $\delta^{13}\text{C} = +0.75\text{‰}$ vs. VPDB), NBS-19 ($\delta^{18}\text{O} = -2.20\text{‰}$ and $\delta^{13}\text{C} = +1.95\text{‰}$ vs. VPDB), and MUN-CO-1 ($\delta^{18}\text{O} = -13.40\text{‰}$ and $\delta^{13}\text{C} = -21.02\text{‰}$ vs. VPDB) during each test.

2.3.6 Minor and Rare Earth Elements

Major, minor elements and rare earth elements (REE) are frequently used as indicator proxy in geological research. By analyzing element concentrations, the modelling of water-rock interaction, the source of formation fluid and redox condition of deposit environment can be interpreted (e.g., Hutcheon et al, 1985; Meyers, 1989; Banner and Hanson, 1990; Denniston et al, 1997; Alibo and Nozaki, 1999). Major, minor and rare earth elements (REE) were analyzed by the Secondary Ion Mass Spectrometry (SIMS) at Memorial University of Newfoundland, which has a high spatial resolution that even can detect the quantity of elements less than 1 ppm. $^{16}\text{O}^-$ ions is accelerated at a few kV and shot onto a gold-coated polished sample mount. The sample then is “sputtered” and generate “secondary” ions, being detected by the mass spectrometer (Denniston et al, 1997). All samples were calibrated on international and in-house standards. The detailed principle and techniques are described in the website of Core Research Equipment & Instrument Training (CREAIT), Memorial University of Newfoundland (<http://www.mun.ca/research/resources/creait/physical-sci/maf/sims.php>). Samples were bombarded with an ion beam of O^- (5-15 μm wide) at 15-20 nA and 10 kV. Each spot was pre-sputtered for 120 seconds with a 25 μm square raster applied to the beam, then sputtered again using a 10 μm raster for 100 seconds. Positively charged sputtered secondary ions were transmitted into the mass spectrometer through a potential of 4.5 keV. To minimize interference, the instrument was operated at an energy offset of 80 eV with a Medium Contrast Aperture (150

μm) and Entrance and Exit Slits paired to give flat topped peaks at a Mass Resolving Power (MRP) of 2975. Count time was dependent of measured elements varied between 2 and 6 secs. OKA-C (calcite from Oka carbonatite complex, Quebec) and NBS 610 standards were analysed by SIMS and compiled results were compared to those by Gladney et al. (1987). The precision expressed as the relative standard deviation of the SIMS equipment is reasonably good: <6% for Mn, Sr, La, Ce, Nd, Dy and Sm while it is <20% for Fe, Yb and Y. The values of REE concentrations were normalized based on Post-Archen Australian Shale (McLennan, 1989).

2.3.7 Porosity Loss Calculation

Quantitative estimation of the amounts of porosity loss by compaction or cementation were performed on samples containing calcite cement and calculated by equations proposed by Lundegard (1992). Other cements were excluded as comparing to the volumes of calcite cement. The results were plotted in modified compactional porosity loss vs. cementational porosity loss diagram. The initial porosity of the Ti-3 sandstone is assumed as 45% (Lundegard, 1992).

$$\text{Compactional porosity loss (COPL)} = P_i - \left(\frac{(100 - P_i) * P_{igv}}{100 - P_{igv}} \right)$$

$$\text{Cementational porosity loss (CEPL)} = (P_i - \text{COPL}) * (C/P_{igv})$$

P_i means initial porosity; P_{igv} means intergranular volume, the sum of optical porosity and pore-filling cement

CHAPTER III

RESULTS OF ANALYSIS ON Ti-3 SANDSTONES

3.1 Petrography

During 1840s, Henry C. Sorby and others developed the foundation of petrography, a technique to study thin slices of rock with the aid of an optical microscope (Krumbein and Pettijohn, 1938; Williams et al., 1982). It has become an inevitable analytical tool for rock study. Petrography provides abundant information on framework mineral components, textural features and diagenetic alteration. Cathodoluminescent microscopy is applied for mineral identification and cement distribution (McLemore and Barker, 1987).

Modal analyses from optical petrographic examination of all thin sections are listed in Appendix 1. Six representative thin sections with typical textural and petrological features were selected for mineral liberation analyses (MLA) for high-resolution mineralogical analysis. Results from MLA study are listed in Table 3.1.

Sample#	Quartz (%)	Plagio-Feldspar	K-Feldspar	Lithic Fragment	Calcite	Dolomite	Pyrite	Illite	Mica	Chlorite	Other Heavy Minerals	Others
3344	48.6	1.0	1.3	5.7	39.2	0.1	0.5	0.7	1.7	0.1	0.4	0.8
3367	52.0	0.5	0.6	3.2	40.6	0.1	0.9	0.2	0.8	0.1	0.4	0.6
3368	74.8	1.0	1.2	6.6	3.0	0.5	8.8	0.8	2.2	0.2	0.4	0.5
3377.1	77.0	0.7	0.4	3.8	5.3	0.3	9.7	0.5	1.2	0.2	0.2	0.7
3382.8	48.5	0.9	0.6	4.4	41.4	0.7	0.8	0.2	1.1	0.2	0.2	1.0
3387.4	81.6	2.3	1.4	6.9	2.6	0.1	0.6	1.1	2.0	0.2	0.4	0.9

Table 3.1: Mineralogic composition (%) of the Ti-3 sandstones determined by the MLA.

The framework grains (detrital sand grains), matrix, cement, authigenic minerals, accessory minerals and pores constitute the basic compositions of sandstones. The framework grains or

detrital grains (0.06-2mm) are primarily quartz, feldspar and rock fragments. Other mineral grains, if present in small amounts, are accessory minerals (Folk, 1980). Folk (1980) proposed a classification for sandstones based on the amount of three framework grains (QFL). To define the modal composition of sandstones, the sum of QFL end members are normalized to 100% of all sand grains. Based on this classification scheme, petrographic examination and MLA results (Table 3.1, Appendix 1) indicate that the Ti-3 sandstones plot generally within the field of sublitharenites ($Q_{86.0} F_{3.1} R_{10.9}$) of high mineralogical maturity. However, a few data points plot within the fields of quartzarenites and a few as feldspathic litharenite (Figure 3.1).

The sources of framework minerals are influenced by the wide variety of igneous, metamorphic and sedimentary parent rocks (Boggs, 2009). In the Flemish Pass sandstones, quartz is a predominant framework grain, followed by lithic fragments (sedimentary and metamorphic) and minor feldspar relics. Sorting and degree of roundness was visually evaluated using the scales of Pettijohn et al. (1987). For the investigated sandstone interval, detrital grains are moderately sorted, fine- to medium- grained, angular to subrounded, presenting tangential, flattened and rare concavo-convex grain contacts. Texturally, Ti-3 sandstones are submature to mature maturity based on the textural maturity scheme proposed by Folk (1980).

Accessory minerals include glauconite, chlorite and carbonaceous material. Heavy minerals, such as pyrite, rutile, apatite, titanite, epidote, staurolite and zircon, are also present in the Ti-3 sandstones (Table 3.2). Bioclasts, of algae, brachiopod, echinoderm and crinoid, are recorded and exhibit signs of replacement and dissolution. Authigenic minerals consist of pervasive calcite and, in order of abundance, pyrite, dolomite, quartz overgrowth and siderite. Grains sometime exhibit a “floating” feature in the sandstones, surrounded by calcite cements (Figure 3.2 a). The Ti-3 sandstones can be generally classified, based on the contents of calcite, into

intervals with extensive calcite cement and poor porosity and others with poor calcite and high volume of irregularly distributed pores (Appendix 1).

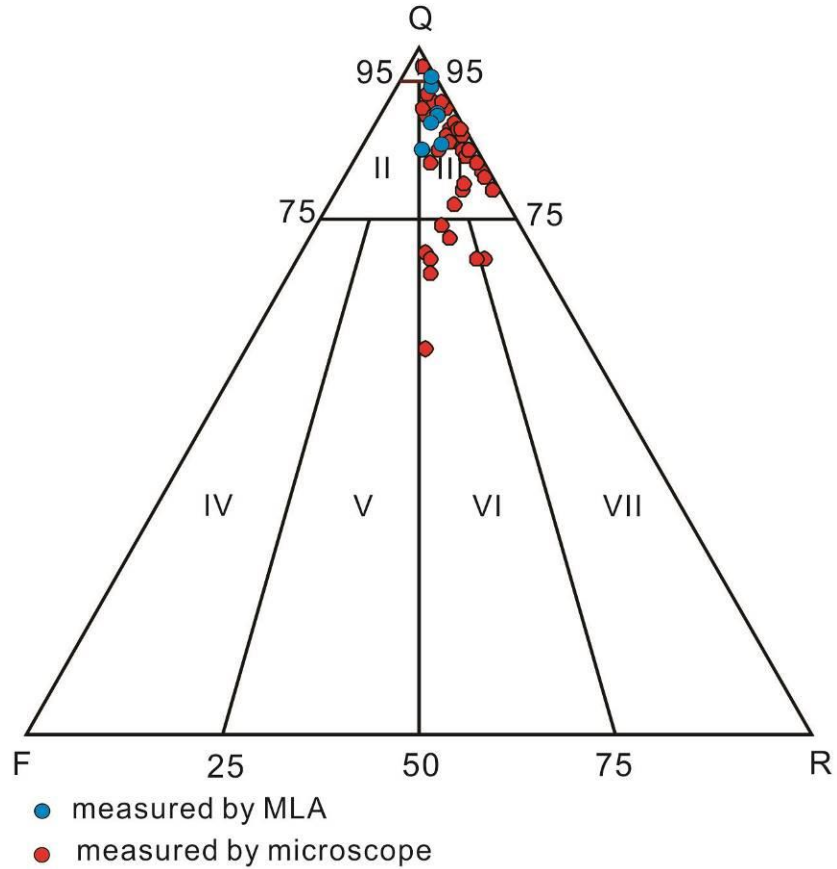


Figure 3.1: QFR triangular diagram of sandstone petrography showing the composition of the Ti-3 sandstones Folk (1980). Q, quartz; F, feldspar; and R, rock fragments. Blue symbols represent results from MLA and red symbols are estimates based on visual estimates from thin-section using conventional optical microscope.

The porosity is mainly secondary (oversized, elongated and moldic pores), and is commonly formed by the dissolution of calcite cements and bioclasts (Figure 3.2 b, c). Depending on the degree of dissolution, it ranges from 1% to 28% (Appendix 1). Enlarged pores are common in the high-porosity sandstone intervals and mainly originate from the dissolution of cements, while moldic pores occur commonly in the calcite-cemented sandstone intervals of bioclasts.

The framework minerals, accessory minerals, bioclasts and authigenic components are discussed below.

3.1.1 Quartz

Visual estimates from petrographic examinations indicated that quartz contents are between 69% and 97% of the detrital grains (Appendix 1). Based on the results from the MLA, quartz contents have average $63.8 \pm 14.2\%$ of modal mineralogy of all samples, ranging from 48.5% to 81.6% (Table 3.1). Detrital quartz grains are mainly fine- to medium-grained and subangular to subrounded. Grain-grain boundaries are easily detectable due to the absence of matrix and normally exhibit point, line and rare concavo-convex grain-grain contacts (Figure 3.2 d, e).

Quartz grains are predominantly monocrystalline with straight extinction, but some monocrystalline quartz grains exhibit sweeping extinction (Figure 3.2 f). A few quartz grains were sourced from plutonic or high-grade metamorphic rocks, since they appear blue to reddish-brown CL (Figure 3.3 a) under the cathodoluminoscope (e.g., Seyedolali, et al., 1997; Boggs and Krinsley, 2006; Trouw, et al., 2009). Less than 2% are polycrystalline and exhibit sutured grain-grain contact. Quartz grains normally exhibit embayed boundaries and corroded texture (Figure 3.3 b). Quartz overgrowths are not common in the cemented layers, but some quartz grains are engulfed by calcite cements and may still have irregular abraded quartz overgrowths, which cause grains to appear subhedral (Figure 3.3 c, d). Nonetheless, in some thin sections, it is likely to be difficult to identify authigenic quartz overgrowths due to etched and partial replaced grain boundaries (Figure 3.3 e).

3.1.2 Feldspar

Feldspars constitute only a small proportion of framework minerals in the Flemish Pass sandstone. They are less than 4% (Table 3.1) and even <2% in the highly mature sandstone

intervals (Appendix 1). K-feldspars and plagioclases occur in approximately equal amounts (Table 3.1).

All feldspars reveal alteration features, such as partial dissolution, replacement by calcite cement, or clay minerals (Figure 3.3 f and Figure 3.4 a). In addition, SEM images reveal partial albitization on K-feldspars (Figure 3.4 b), where albites replace K-feldspars as patches, and grow parallel to cleavage planes in parent grains.

3.1.3 Lithic Fragments

Lithic fragments constitute about $5.1 \pm 1.4\%$ of the detrital grains (Table 3.1). They have predominantly a sedimentary origin, including cherts, mudstones and silty clasts (Figure 3.4 c, d), whereas metamorphic rock fragments (MRF) occur frequently in the middle to lower part of the Ti-3 interval, such as schist, phyllite and metamorphic quartz (Figure 3.4 e). Siltstone fragments enclosed in calcite cement are present in some of the sandstone intervals (Figure 3.4 f). Minor carbonate grains occur in the sandstones as dolostone fragments, which could have been transferred from the underlying Ranking Formation, and as ooids (Figure 3.5 a, b).

3.1.4 Accessory Minerals

A small amount of accessory minerals is observed and include glauconite, chlorite, various heavy minerals and rare carbonaceous material.

3.1.4.1 Glauconite

Well-rounded glauconite pellets occur sporadically in the upper to middle part of Ti-3 sandstone interval. As glauconite can be used as typical paleo-environment indicator mineral, the changing amount of glauconite with depth may reflect gradual transformation to near shore

marine depositional environment (Selley, 1996). Some glauconite pellets exhibit deformed morphology between detrital grains (Figure 3.5 c).

3.1.4.2 Chlorite

Rare yellowish green and sheet-shaped ductile detrital chlorite grains are rarely embedded in the massive calcite cement (Figure 3.5 d). They exhibit gradient interference color from blue to light gray under the cross-polarized light. Boggs (2009) suggested that the source of detrital chlorite grains may be primarily derived from metamorphic rocks. The partial dissolution of chlorite grains may have released iron to precipitate ferroan calcite cements. In addition, minor deformed chlorite-muscovite matrix disseminated in the lower part of the Ti-3 sandstones (Figure 3.5 e) may have originated from the low-grade metamorphic rocks or from the alteration of biotite (van der Pluijm and Kaars-Sijpesteijn, 1984).

3.1.4.3 Heavy Minerals

Trace amounts of heavy minerals such as pyrite, rutile, apatite, titanite, epidote staurolite and zircon occur along with minor tourmaline, fluorite, ilmenite, and monazite (Figure 3.5 f and Figure 3.6 a). However, based on the existing morphology of pyrite in the investigated interval, we classified pyrite as one of authigenic minerals. Heavy minerals normally contribute to less than 1% of the Ti-3 sandstones (Table 3.1). The percentage composition of each heavy minerals is listed in Table 3.2.

3.1.4.4 Carbonaceous Material

Rare irregular-shaped carbonized plant tissue (?) occurs near the top part of the Ti-3 sandstones (Figure 3.6 b), which is consistent with estuarine depositional environment.

Sample#	Pyrite(%)	Tourmaline	Zircon	Epidote	Fluorite	Rutile	Apatite	Ilmenite	Titanite	Staurolite	Monazite	Corundum	Barite	Total
3367	0.87	0.01		0.08	0.01	0.19	0.02	0.01	0.01	0.02	0.01			1.23
3368	8.77	0.02	0.03	0.01		0.28	0.02		0.02	0.02	0.01			9.19
3344	0.47	0.01	0.01	0.28		0.07	0.03		0.01	0.01				0.89
3382.8	0.76		0.01	0.01	0.01	0.12	0.03	0.01	0.01	0.02				0.98
3377.1	9.65					0.15	0.03	0.01	0.01	0.01				9.86
3387.4	0.56		0.02			0.14	0.01	0.02	0.02	0.03		0.06	0.01	0.87

Table 3.2: Heavy mineral composition (%) of the Ti-3 sandstones determined by the MLA.

3.1.5 Bioclasts

Intact or partial dissolved bioclasts and recrystallized skeletal fragments of shallow marine organisms constitute about 9% of occur in the Flemish Pass Ti-3 sandstones (Figure 3.6 c-f) (Appendix 1). They include brachiopods, bivalves and algal aggregates.

Brachiopods are marine organisms that appeared in the early Cambrian. Calcitic brachiopod shells usually exhibit fibrous to prismatic structure (Figure 3.6 e, f).

Algal aggregates are clumped parts of micritic algae that precipitate in shallow-water environments (Figure 3.6 c). Pelloids are rounded particles ($\leq 500 \mu\text{m}$) consisting of homogenous mictite (Figure 3.7 a) that generally precipitate in shallow, restricted, low-energy marine environment (Adams et al., 1984; Flügel, 2004). Algal aggregates pelloids and are more abundant in the upper part of Ti-3 Member of the Bodhrán Formation.

3.1.6 Matrix

Matrix is fine-grained material consisting of particles about 0.03mm that infiltrate into interstitial spaces or infill void spaces as authigenic clay minerals precipitating from the alteration of unstable detritus (Boggs, 2009; Tucker, 2009).

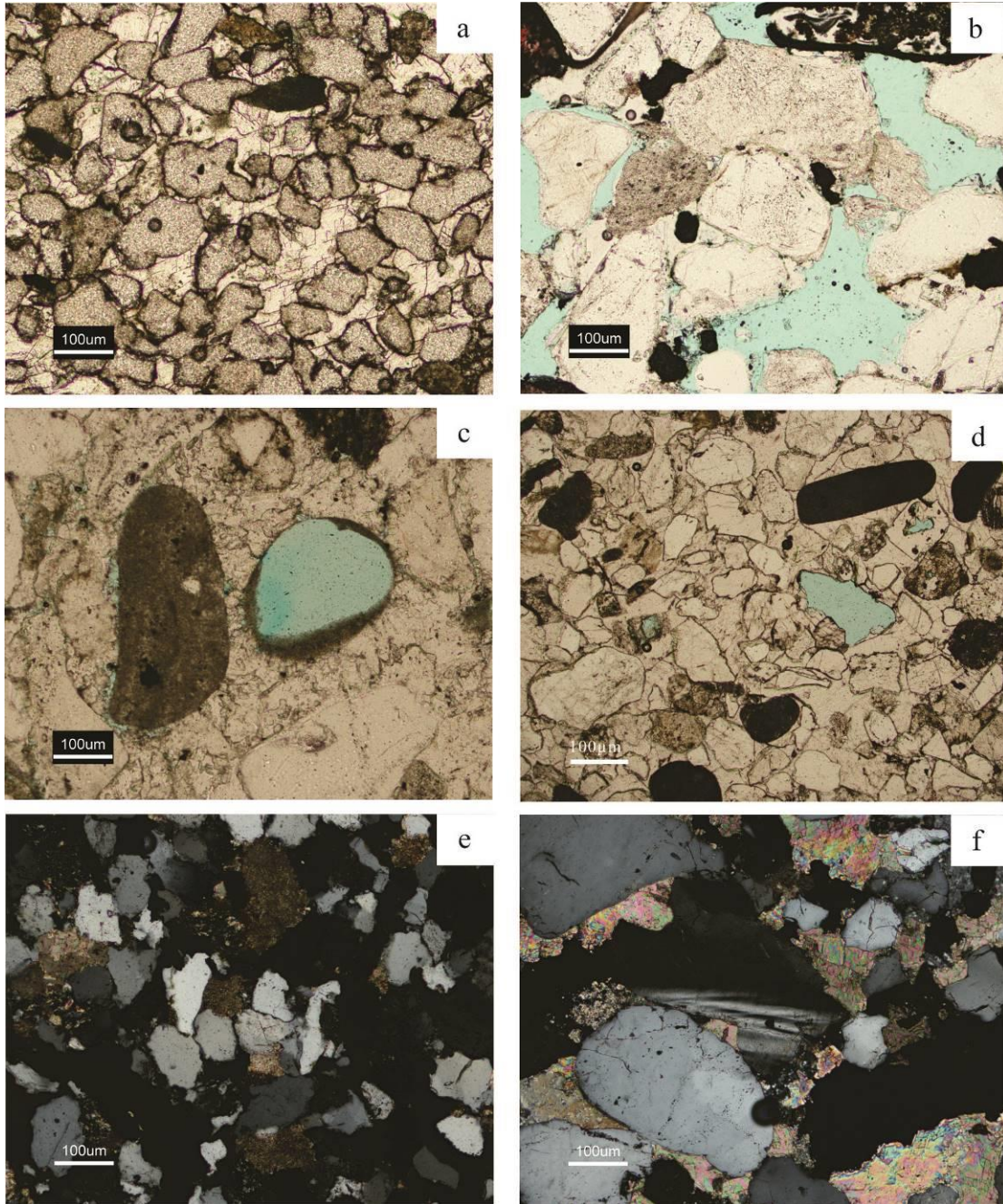


Figure 3.2: Photomicrographs of petrographic features of the Ti-3 sandstones. (a) Framework grains “floating” on the cement, Sample# 3342.6, polarized light, (b) enlarged pores, Sample# 3377.1, polarized light, (c) Moldic pore, Sample# 3382.8, polarized light, (d) Point and line grain contact, Sample# 3377.9, polarized light, (e) Concavo-convex grain contact, Sample# 3389.6, crossed polars, and (f) Quartz exhibiting sweeping extinction, Sample# 3382.8, crossed polars.

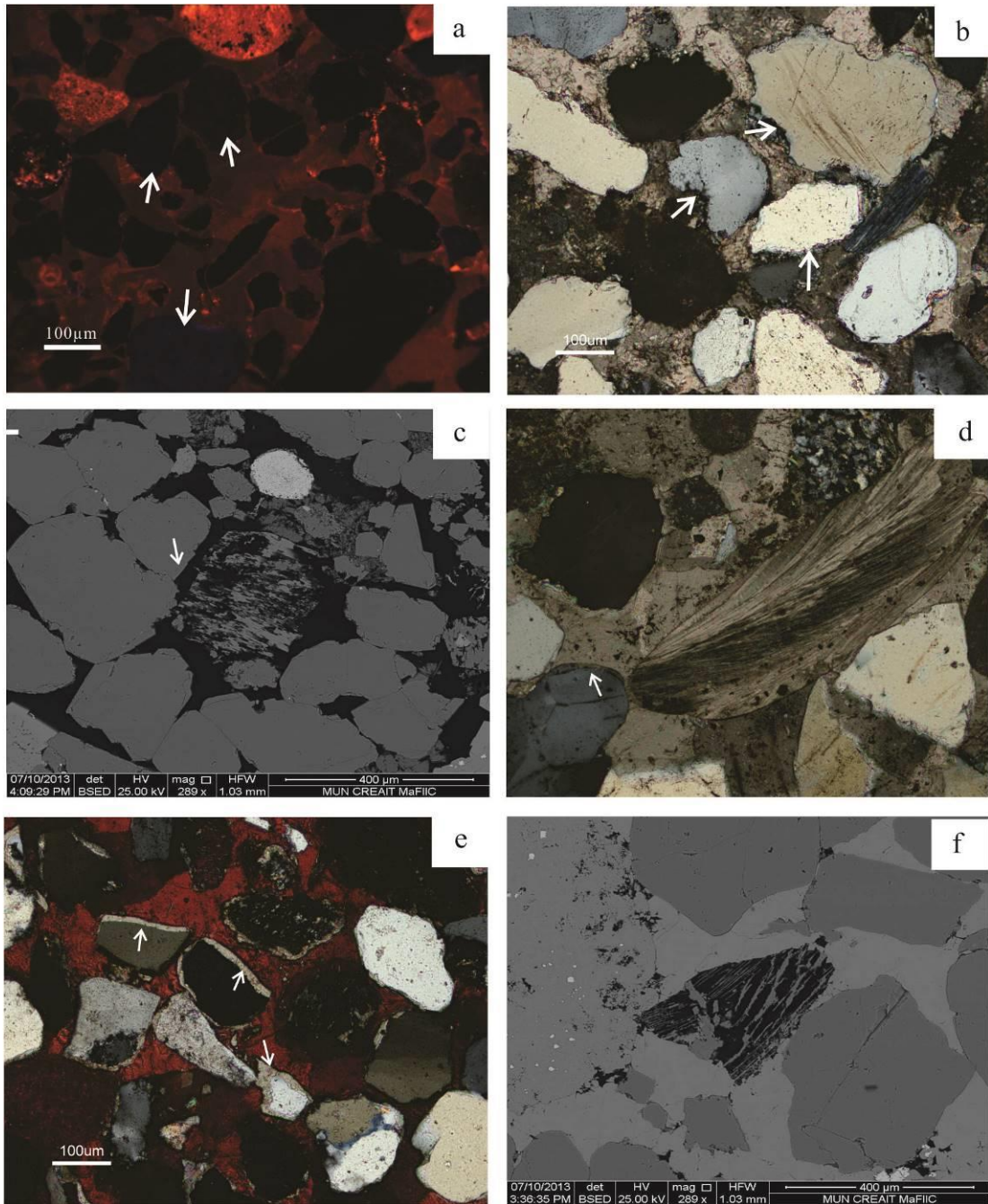


Figure 3.3: Photomicrographs of petrographic features of the Ti-3 sandstones. (a) Cathodoluminescence image showing bluish CL of some quartz grains (arrow), Sample# 3377.9, (b) Quartz showing pitted margin and embayment (arrow), Sample# 3382.8, crossed polars, (c) Quartz Overgrowths (arrow), Sample# 3387.4, SEM, (d) Quartz Overgrowths occurring in cemented interval, Sample# 3381.1, crossed polars, (e) Quartz replaced by calcite cement (arrow), Sample# 3386.5, crossed polars, and (f) Remnant feldspar exhibiting skeletal structure, Sample# 3382.8, SEM.

Most of the Ti-3 sandstones are generally matrix-free due to the high kinetic energy during transport and deposition. Nevertheless, fibrous or lathy illite occur around dissolved/altered feldspars (Figure 3.7 b). The MLA results indicate that matrix constitutes less than 1% of the Ti-3 sandstones.

3.1.7 Authigenic Components

Authigenic components in the sandstones are minerals precipitating or recrystallized in-situ after deposition. The source for authigenic minerals is internal from altered detritus or external from adjacent layers as result of compaction, which reflect the impact of diagenesis during sediment burial. The dominant authigenic mineral in the investigated sandstones is calcite that occludes porosity.

3.1.7.1 Carbonate Cement

Carbonate cement is the major authigenic cement in the investigated sandstones and occurs as coarse poikilotopic cement occluding pore spaces, or rarely as fibrous or sparry cement on bioclastic debris.

Calcite makes up the dominant pore-occluding cement in the investigated sandstone. The calcite constitutes 13% to 47% of rock composition in the cemented samples (Appendix 1). The MLA study indicates that it is a ferroan-calcite, consistent with the equally-distributed dark red-purple stain in the thin sections (Figure 3.7 c). The pervasive pore-filling calcite cement mainly occurs as poikilotopic cement (300-800 μ m) engulfing majority of grains, and partially dissolves feldspars and quartz (Figure 3.3 b, f). The twin planes of this calcite appear on either side of framework grains and bioclasts (Figure 3.7 d). All poikilotopic calcite cements exhibits uniform CL (dull to bright) without concentric zoning (Figure 3.7 e), However, the calcite crystals can

exhibit dull to no CL when sandstone intervals contain siderites (Figure 3.7 f and 3.8 a). In addition, minor early fibrous calcite occurs on the bioclasts (Figure 3.8 b).

Fracture-filling calcite cement (375 to 1400 μ m; Figure 3.8 c) is rare and appears in 0.8-14mm wide veins in the well-cemented samples of lower stratigraphic levels of the borehole. The staining color is identical to poikilotopic calcite, dark red-purple, showing that the vein is also iron-rich.

Rare dolomite cement dolomite in the Ti-3 sandstones has been stained into light blue color (Figure 3.8 d). It usually grows in the interstitial spaces between quartz grains within the intervals that have no pervasive calcite cement. It generally occurs as fine-grained dolomite aggregates (80-100 μ m, Figure 3.8 e) and individual euhedral to subhedral ferroan dolomite rhombs (35-180 μ m, Figure 3.8 d). Dolomite cement can also develop as overgrowth around calcite remnants, which is distinguished by staining colors (Figure 3.8 f). In addition, ankerite seldom occurs as overgrowth developing outside of the ferroan dolomite nucleus, which is easy to distinguish by MLA (Figure 3.9 a).

Authigenic siderite (<1%) only occurs in the lower part of the Ti-3 sandstones, at around 3385m in depth. Siderite normally disperse within calcite cement and also form along the boundaries of some detrital grains as very fine grained, dark spherulite-shaped crystal rim (Figure 3.7 f and 3.8 a).

3.1.7.2 Silica Cement

Silica cement (average 2.3%, Appendix 1) occurs as syntaxial overgrowths on some detrital quartz grains (Figure 3.3 c, d). The silica cement is less abundant in Ti-3 sandstones than in clastic reservoirs of the Hibernia field of the Jeanne d'Arc Basin (4.3% to 7.3%, respectively;

Brown et al., 1989; Hesse and Abid, 1998). The quartz overgrowths are more abundant in the sandstone intervals with poor calcite cements (Appendix I).

3.1.7.3 Pyrite

Pyrite is the second most abundant authigenic mineral in the Flemish Pass Ti-3 sandstones that ranges from 0% to 17%, with average of $4.4 \pm 3.6\%$ (Appendix 1). It occurs replacing bioclasts as small euhedral to subeuhedral cubes or fine crystals, or occluding intergranular pores and replacing calcite remnants as cements (Figure 3.9 b-d).

3.2 Microthermometry

Due to the scarcity of dolomite and siderite cements, the microthermometric and geochemical analyses are focused on the calcite cement.

The calcite cements in the Ti-3 sandstones host primary fluid inclusions including common mono-phase (all-liquid) fluid inclusions in the cores of calcite crystals and rare two-phase (liquid and vapor) fluid inclusions in the rims of those crystals and in the fracture-filling calcites (Figure 3.10). Table 3.3 summarizes the results of microthermometric measurements. All-fluid inclusions size varies from 5 to 12 μm and the two-phase fluid inclusions are <10 μm with approximate liquid: vapor ratios of 6:1. Microthermometric measurements of homogenization temperature (T_h), initial melting temperature (T_i) and final ice-melting temperature (T_m) were obtained from primary two-phase primary fluid inclusions. Measurements of T_i and T_m were also performed on several monophasic aqueous inclusions. Since freezing alters the fluid inclusion's morphology, homogenization temperatures of the two-phase inclusions were measured first (Lawler and Crawford, 1983). The estimated salinities were calculated based on T_m results (Bodnar, 2003).

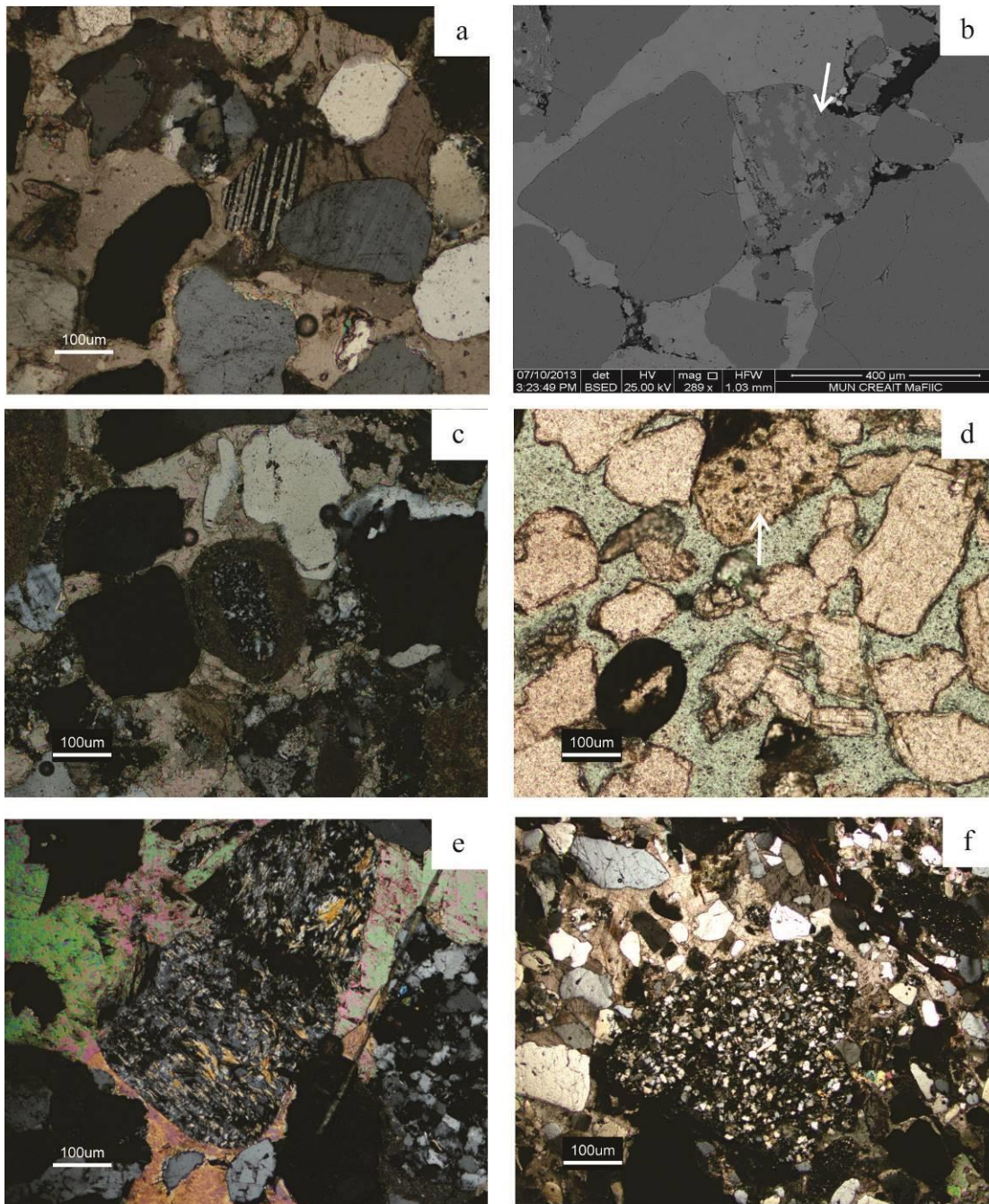


Figure 3.4: Photomicrographs of petrographic features of the Ti-3 sandstones. (a) Feldspar showing partial dissolution and replacement by calcite cement, Sample# 3386.5, crossed polars, (b) Albitized K-feldspar engulfed by calcite cement (arrow), patchy albite in dark shades of grey and K-feldspar in light shades of grey, Sample# 3382.2, SEM, (c) Chert coated with micrite, Sample# 3382.2, crossed polars, (d) Sedimentary lithic fragment (arrow, possibly mudstone), Sample# 3357.7, polarized light, (e) Schist and metamorphic quartz, Sample# 3386.5, crossed polars, and (f) Siltstone, Sample# 3375.85, crossed polars.

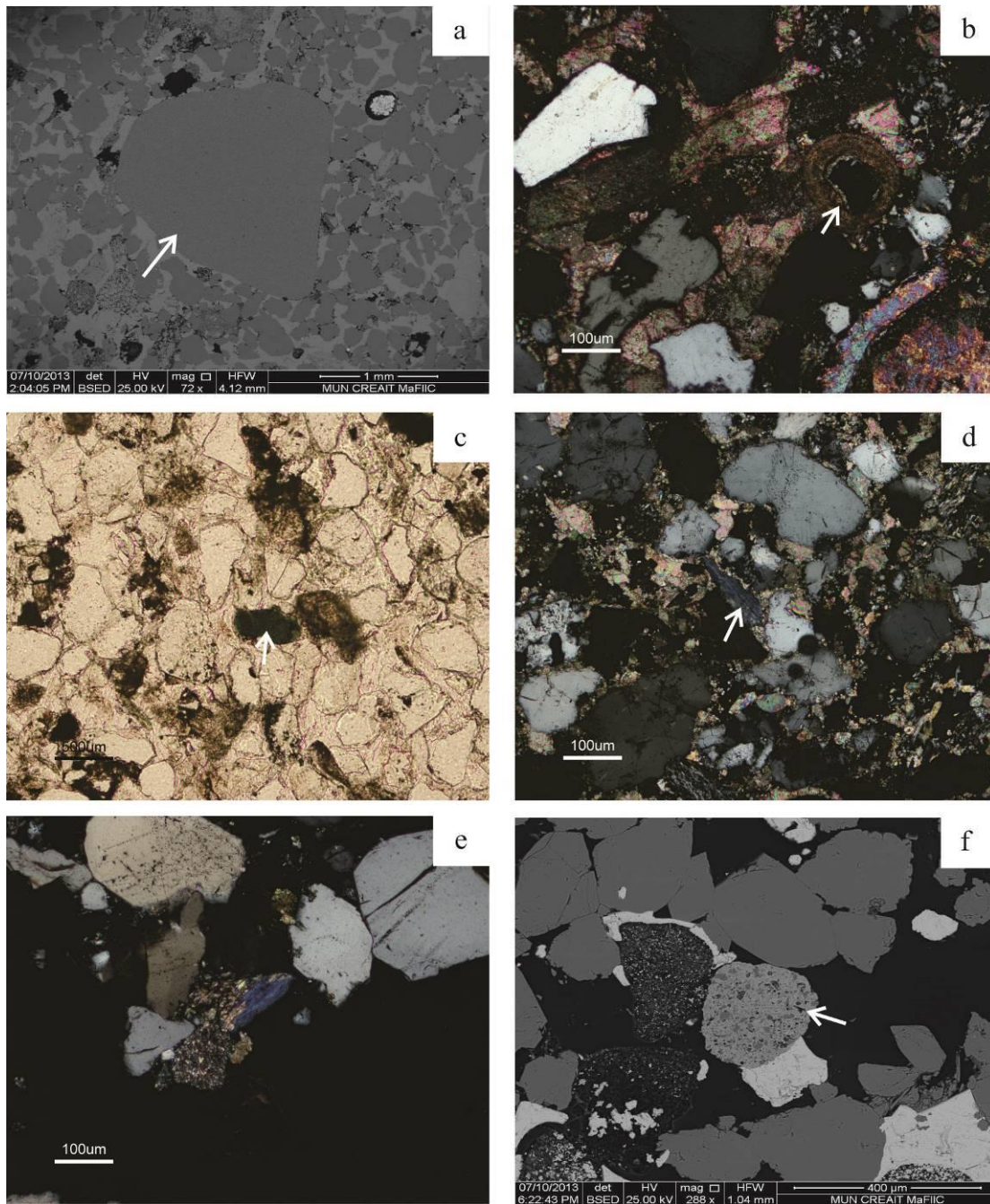


Figure 3.5: Photomicrographs of petrographic features of the Ti-3 sandstones. (a) Dolomite (arrow), Sample# 3382.8, SEM, (b) Ooid cored on quartz (arrow), Sample# 3382.8, crossed polars, (c) Deformed glauconite (arrow), Sample# 3363.4, polarized light, (d) Chlorite (arrow), Sample# 3384.5, crossed polars, (e) Primary-origin chlorite-muscovite matrix (arrow, possibly phyllite), Sample# 3387.8, crossed polars, and (f) Rutile growing with quartz, Sample# 3377.2, SEM.

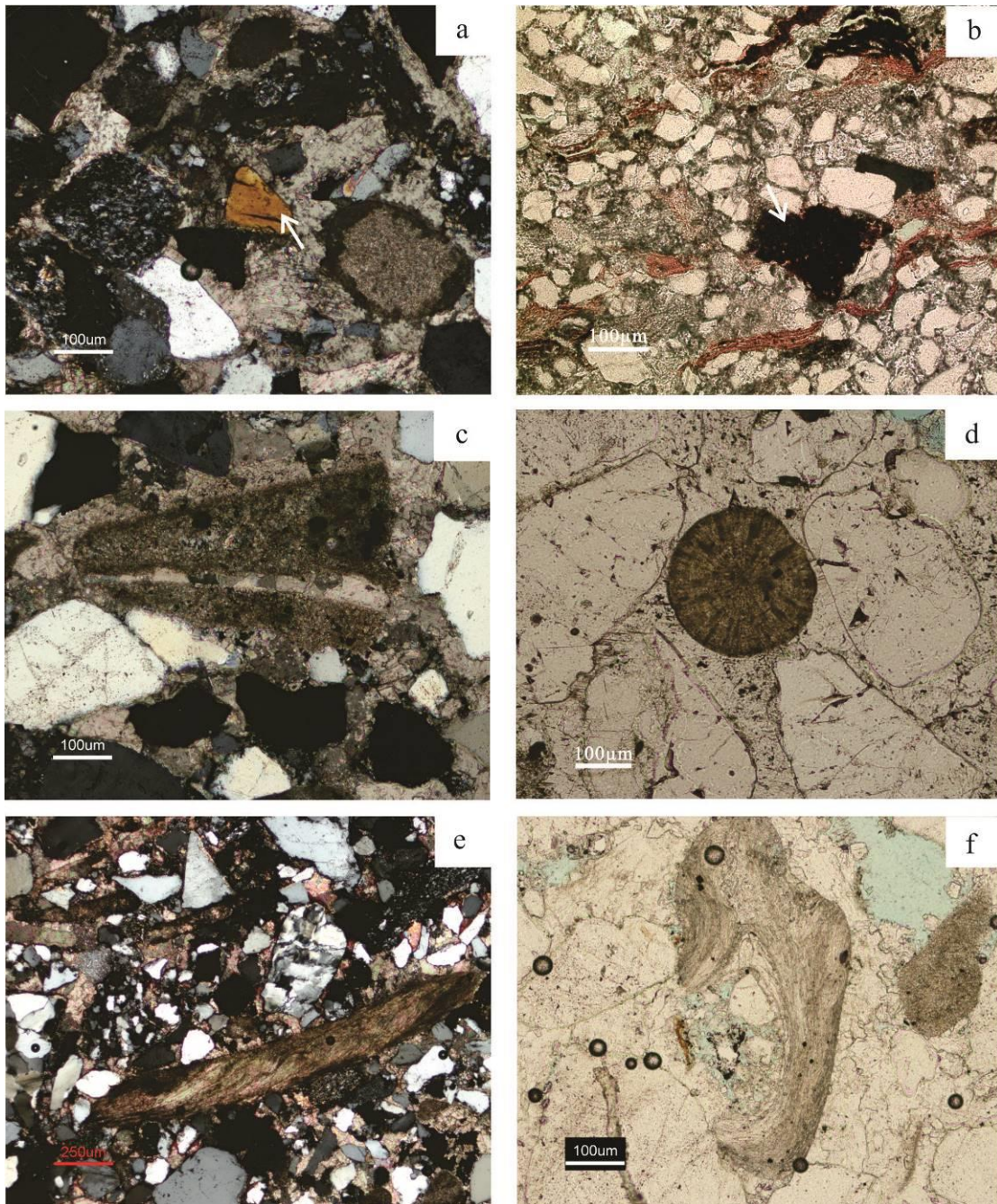


Figure 3.6: Photomicrographs of petrographic features of the Ti-3 sandstones. (a) Staurolite (arrow), Sample# 3386.5, crossed polars, (b) Wood tissue (arrow), Sample# 3357.2, polarized light, (c) Fossil fragments are recrystallized to calcite, Sample# 3382.8, crossed polars, (d) Radial ooid, Sample# 3381.1, polarized light, (e) Brachiopods, Sample# 3382.8, crossed polars, and (f) A transverse section of brachiopod showing dissolution, Sample# 3382.8, polarized light.

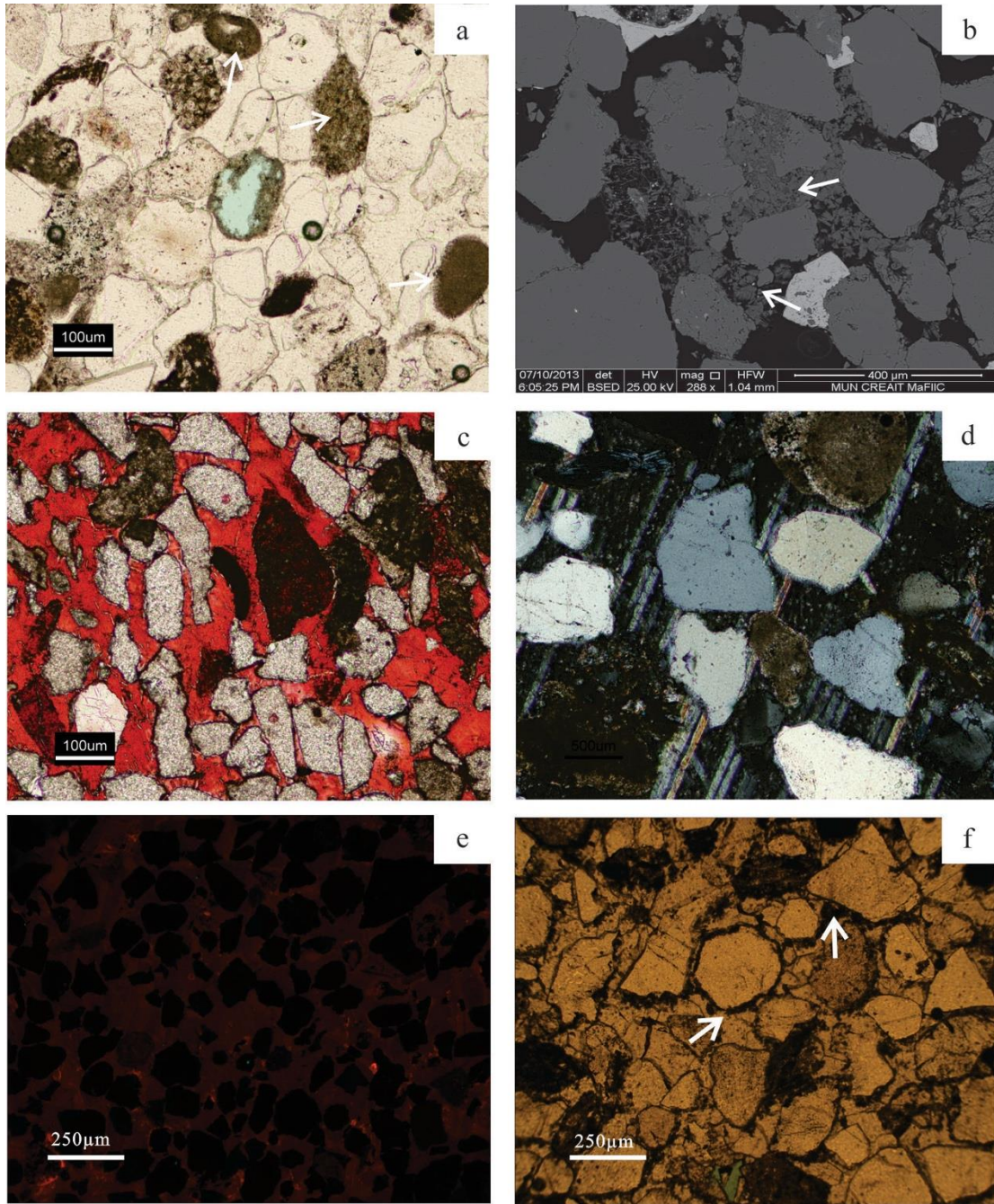


Figure 3.7: Photomicrographs of petrographic features of the Ti-3 sandstones. (a) Algae (arrow), Sample# 3344.6, polarized light, (b) Lathy illite produced from altered feldspar filling pores (arrow), Sample# 3355.6, SEM, (c) Calcite cement stained dark red-purple, Sample# 3344.6, polarized light, (d) Twinning planes of calcite cements occurring uninterruptedly on either side of grains, Sample# 3365.9, crossed polars, (e) Cathodoluminescence image showing dull, to at times bright, CL of poikilotopic calcite cements, Sample# 3367.8, and (f) Spherulitic siderites (arrow) scattering on the poikilotopic calcite cement and on grain rims, Sample# 3385.7, polarized light.

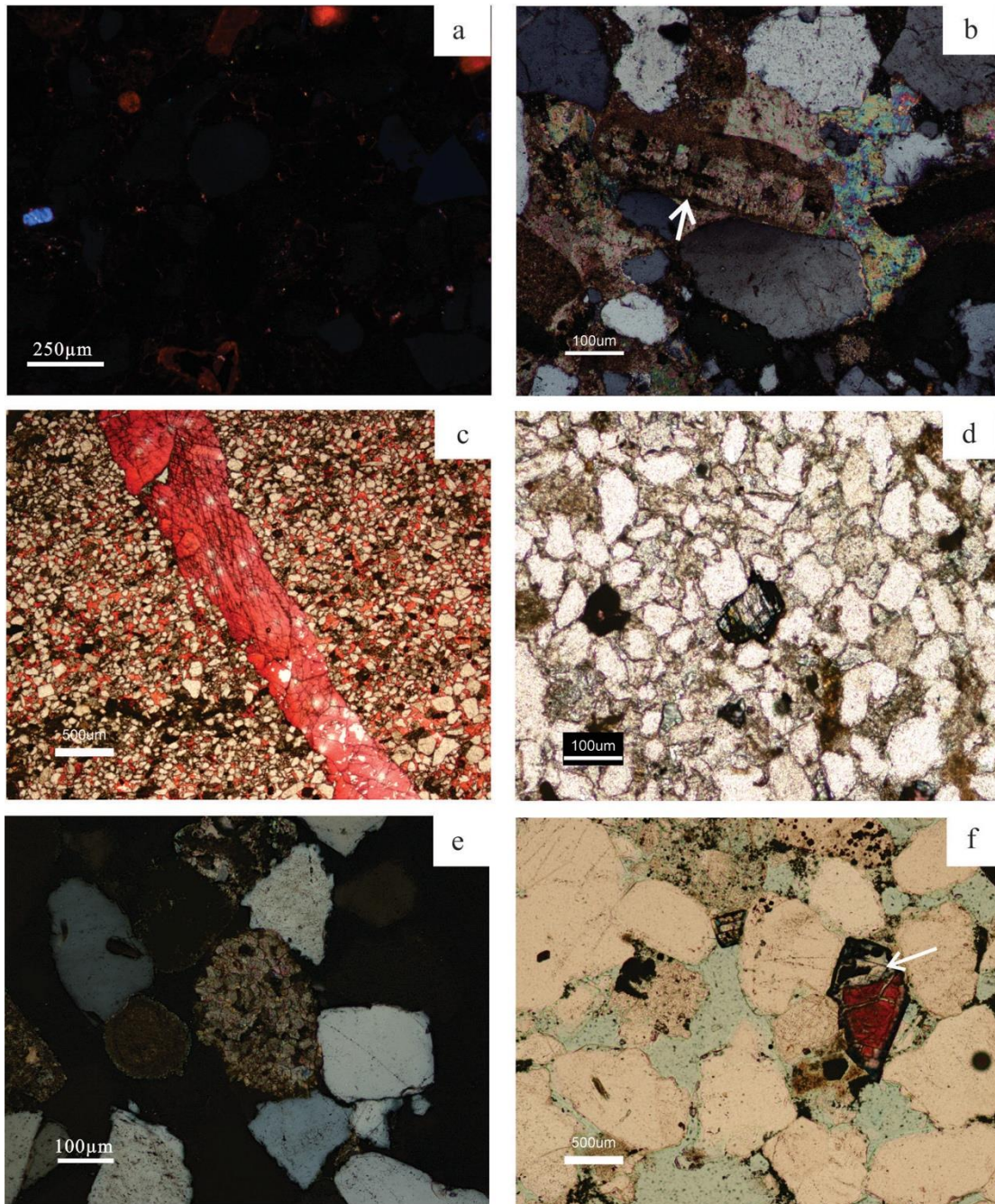


Figure 3.8: Photomicrographs of petrographic features of the Ti-3 sandstones. (a) Cathodoluminescence image of (Figure 3.7 f) showing dull CL of sediment components from cemented intervals containing siderite, Sample# 3385.7, (b) Minor fibrous and sparry calcite has filled inside a bioclast (arrow), Sample# 3365.9, crossed polars, (c) Fracture-filling calcites, Sample# 3357.2, polarized light, (d) Dolomite rhomb dispersed in interstitial spaces after calcite dissolution, Sample# 3348.6, polarized light, (e) Dolomite aggregates dispersed in interstitial spaces after calcite dissolution, Sample# 3377.1, crossed polars, and (f) Minor dolomite on calcite cement remnants (arrow), Sample# 3387.8, polarized light.

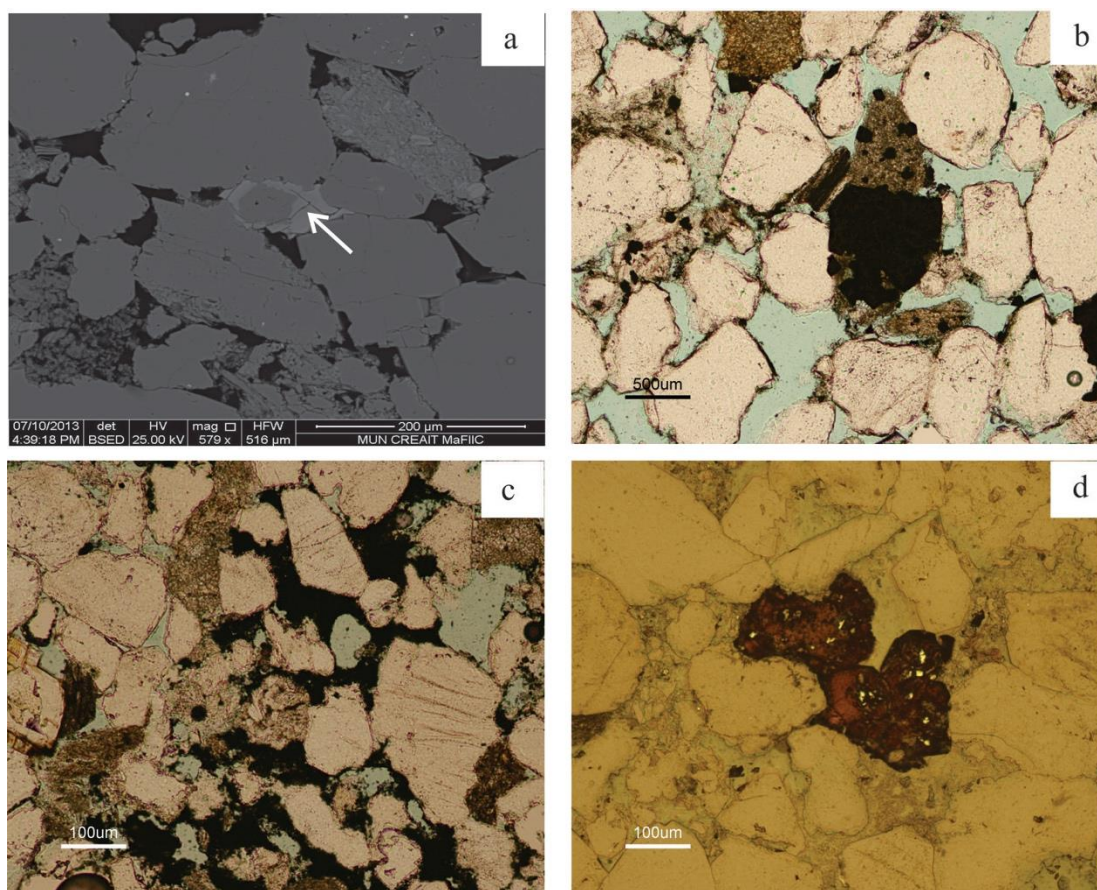


Figure 3.9: Photomicrographs of petrographic features of the Ti-3 sandstones. (a) Ankerite (arrow) seldom occurring as overgrowth of ferroan dolomite, Sample# 3387.4, SEM, (b) Spherulitic and subhedral pyrite replacing bioclasts, Sample# 3368.6, polarized light, (c) Late pyrite cements filling intergranular spaces Sample# 3355.6, polarized light, and (d) Late pyrite replacing calcite remnant, Sample# 3387.8, reflected light.

The values of T_h for two-phase fluid inclusions in the intergranular calcite cements range from 63.9 to 83.1°C ($72.3 \pm 5.4^\circ\text{C}$, $n=27$; Table 3.3); however, those of the fracture-filling calcites are much higher ($101.0 \pm 21.5^\circ\text{C}$, $n=16$; Table 3.3). The estimated mean salinities for intergranular and fracture-filling calcite cements are 8.8 ± 1.2 eq. wt.% NaCl, $n=13$ and 10.0 ± 1.8 eq. wt.% NaCl, $n=8$, respectively (Table 3.3), whereas all-fluid inclusion have a lower

salinity (3.0 ± 1.7 eq. wt.% NaCl, $n=28$; Table 3.3). All T_i values of two-phase inclusions from both types of calcites fall within the range between -45°C and -50°C (Appendix 2).

Type		T_h °C	$T_{m(ice)}$ °C	Eq. wt% NaCl
Poikilotopic calcite				
(All-liquid inclusion)	n		27	27
	Mean		-1.7	3.0
	S.D		1.1	1.7
	Max		-0.3	6.5
	Min		-4	0.5
Poikilotopic calcite (liquid-vapor inclusion)				
	n	27	13	13
	Mean	72.3	-5.8	8.8
	S.D	5.4	1	1.2
	Max	83.1	-4	11.2
	Min	63.9	-7.6	7.2
Fracture-filling calcite				
	n	16	8	8
	Mean	101.0	-6.7	10.0
	S.D	21.5	1.6	1.8
	Max	138.1	-5.8	11.5
	Min	75.3	-9.3	8.9

Table 3.3: Statistics of microthermometric measurements of calcite cements in the Ti-3 sandstones.

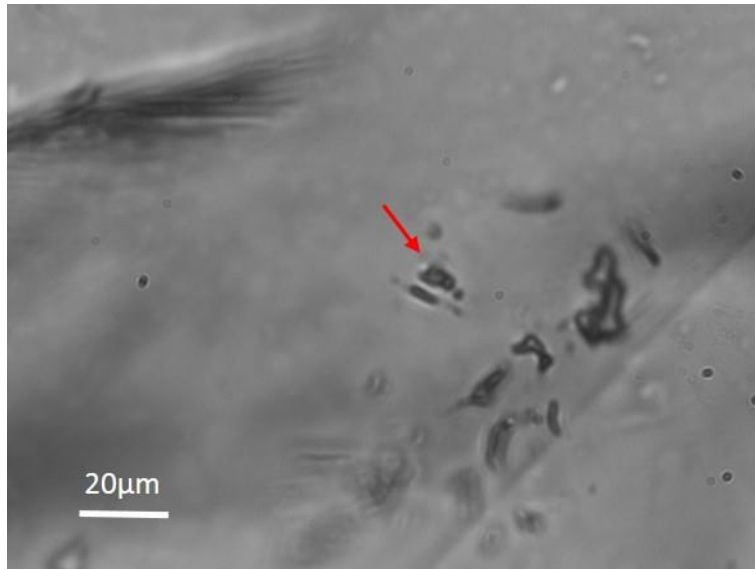


Figure 3.10: Photomicrographs of primary fluid inclusions in a calcite cement from Ti-3 sandstones. Irregular-shaped mono-phase fluid inclusions likely occur in clusters (right), while rare two-phase fluid inclusions generally occur individually in the crystal rim (arrow).

Sample#	N ₂	Ar	CO ₂	CH ₄	N ₂ /Ar	CO ₂ /CH ₄
3334.8	0.7436	0.0079	1.564	2.7185	94.17	0.57
3344.5	0.7391	0.0101	3.8043	1.7506	73.11	2.17
3367.8	1.1577	0.0217	5.0362	4.8585	53.25	1.04
3377.9	0.7015	0.0109	3.5181	2.8247	64.21	1.24
3379.7	1.0251	0.0198	7.8036	6.4294	51.70	1.21
3381.1	0.1295	0.0021	0.6956	0.2817	61.70	2.47

Table 3.4: The weighted mean values of fluid-inclusion gas from sandstone samples with high volume of calcite cements by the incremental crush method. The ratios of N₂/Ar and CO₂/CH₄ of quartz are proposed by Blamey et al (2014).

3.3 Fluid-Inclusions Gas Ratios

The geochemistry of parent diagenetic fluids can be better understood by combining results with those from fluid inclusion gas analysis (Blamey, 2012; Azmy and Blamey, 2013; Blamey et al., 2014). Six samples with high calcite cementation (>30%) were selected for fluid-inclusion gas analysis in the current study (Table 3.4, Appendix 3). Five samples show a relatively similar weighted mean ratio of CO₂/CH₄ and N₂/Ar ranging from 1.04 to 2.47 and 51.7 to 73.1, respectively. One sample (#3334.8) has lower weighted mean ratio of CO₂/CH₄ (0.57) and higher N₂/Ar (94.2).

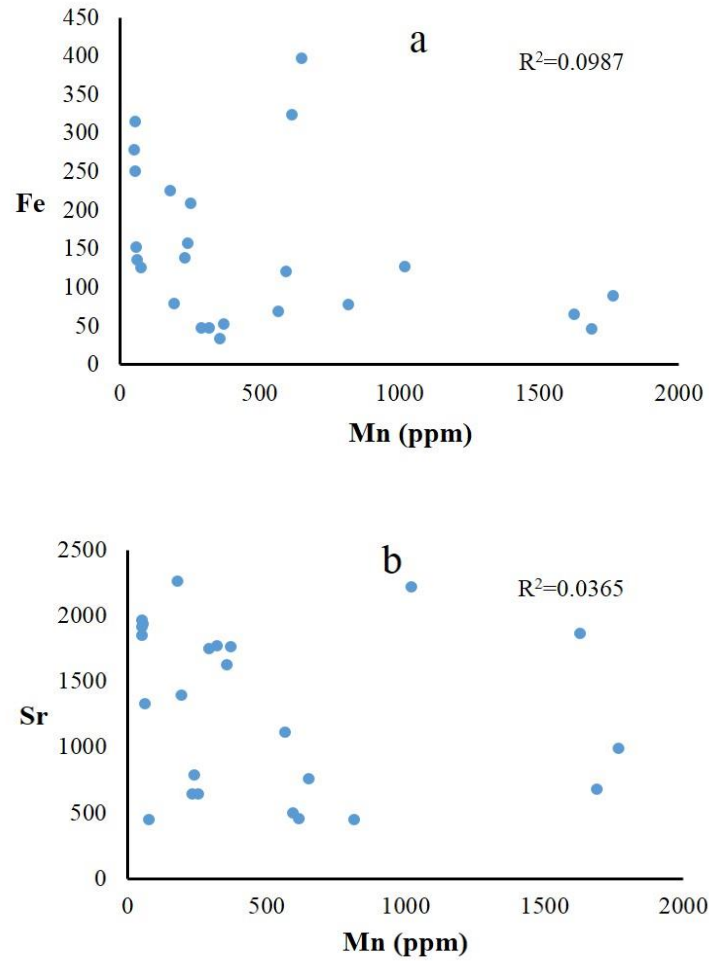


Figure 3.11: Scatter diagrams of (a) Mn vs. Fe and (b) Mn vs. Sr for calcite cements.

Sample#	$\delta^{13}\text{C}_{\text{VPDB}}$	$\delta^{18}\text{O}_{\text{VPDB}}$	Sample#	$\delta^{13}\text{C}_{\text{VPDB}}$	$\delta^{18}\text{O}_{\text{VPDB}}$
3335.6	-0.7	-8.9	3372.5	-3.4	-7.9
3340.6	-3.9	-10.6	3374	-2	-8.5
3342.6	-4.4	-11	3375	-2.8	-9
3344.6	-1.2	-7.1	3375.85	-4.2	-8.9
3351.3	-1.3	-7.2	3377.9	-4.8	-8.1
3357.2	-0.7	-8.4	3379.7	-4.3	-7.5
3360.4	-4.1	-7.8	3381.1	-2.6	-9.1
3363.4	-3.9	-7.9	3384.8	-2.5	-8.7
3365.9	-0.1	-7.7	3385.7	-3	-7.2
3367.8	-3.5	-8.2	3386.5	-4.7	-8
3369.4	-3.2	-8.2	V1	-2.1	-10.8
3369.9	-2.8	-5.3	V2	-1.8	-10.7
3371.1	-3.1	-9	V3	-2.2	-10.7

Table 3.5: Stable carbon and oxygen isotopic data of calcite cements. The V1, V2, and V3 values refer to measurements of fracture-filling calcites.

3.4 Geochemistry

3.4.1 Oxygen and Carbon Isotopes

The C- and O- isotopic measurements of the intergranular calcite cements in the Ti-3 Member sandstones of the Bodhrán Formation (Table 3.5) show that the $\delta^{13}\text{C}$ values have a slightly broad range of -4.8 to -0.1‰ VPDB (mean $-2.9 \pm 1.32\%$, VPDB, $n=23$). The $\delta^{18}\text{O}$ isotopic values cluster around -8‰ VPDB, ranging from -11.0 to -5.3‰ VPDB (mean $-8.3 \pm 1.23\%$ VPDB, $n=23$). The mean $\delta^{13}\text{C}$ and $\delta^{18}\text{O}$ values of the fracture-filling calcites are $-2.0 \pm 0.2\%$ VPDB, $n=3$ and $-10.8 \pm 0.1\%$ VPDB, $n=3$, respectively.

3.4.2 Minor and Rare Earth Element

The concentrations of minor elements (e.g., Fe, Mn, Sr) in calcite cement are tabulated in Appendix IV and summarized in Table 3.6. The contents of Mn vary from 54 to 1527 ppm with a mean value of 508 ± 515 ppm and Fe ranges from 28 to 494 ppm with a mean value of 126 ± 110 ppm (Table 3.6, Appendix 4). In the analyzed samples, Mn contents are higher than those of Fe except for only one sample (# 3379.1; Table 3.6). The Sr mean concentrations show a relatively narrower range of variations (from 1145 to 1725 ppm; Table 3.6) except for Sample# 3344.6, which has considerably lower Sr (653 ppm). No significant correlation was found between Mn and Fe, or Mn and Sr (Figure 3.11)

Shale normalization of REE contents was calculated based on the equation of Bau and Dulski (1996). The mean total REE ($\sum\text{REE}$) values of investigated calcite cements vary from 4 ± 0.5 ($n=7$) to 15 ± 5 ppm ($n=6$) (Table 3.6). The mean Ce anomaly values (de Baar et al., 1985) display a narrow range and are close to unity (Table 3.6). The shale normalized REE distribution patterns (relative to PAAS) of calcite cements (REE_{SN}) are generally consistent, exhibiting the same medium REEs-enrichment and slight heavy REEs-depletion (Figure 3.12).

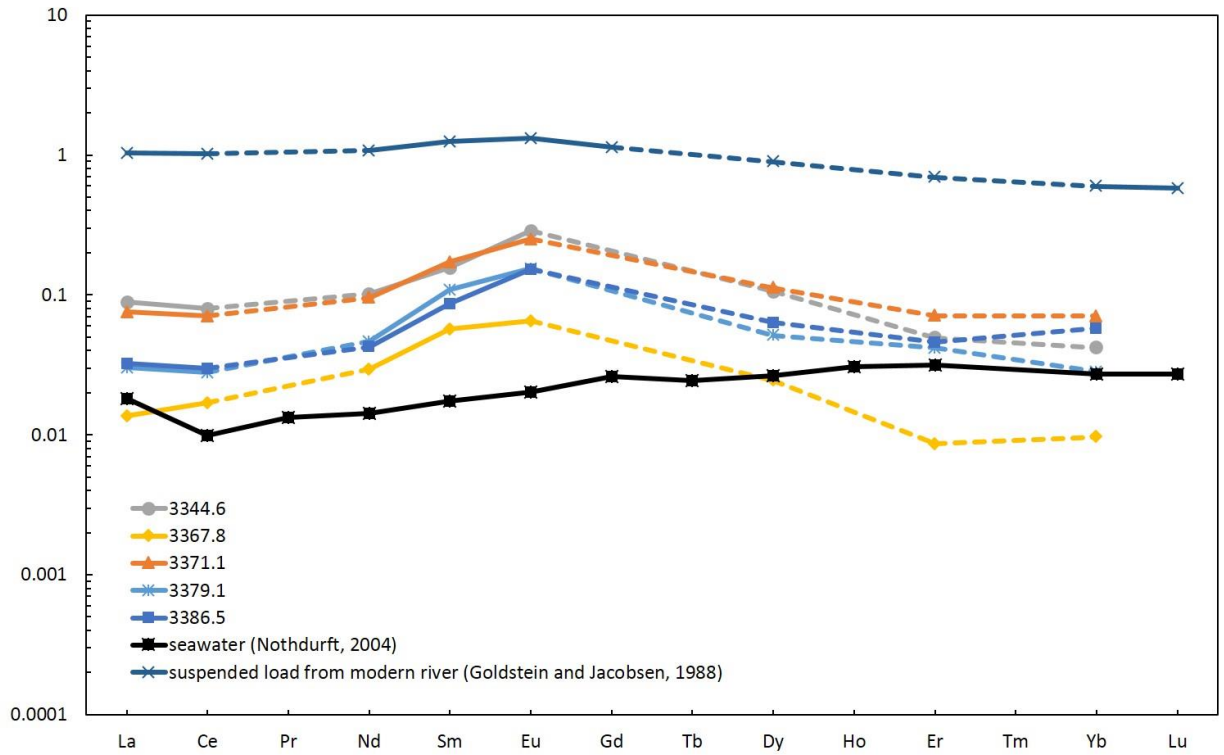


Figure 3.12: Shale-normalized (PAAS) REE patterns of calcite cements in the Ti-3 sandstones, Lennard Shelf cements reflecting seawater-like pattern (Nothdurft et al., 2004) and suspended load from modern river water reflecting fluvial input pattern (Goldstein and Jacobsen, 1988).

Sample#		Fe (ppm)	Mn (ppm)	Sr (ppm)	Mn/Fe	La (ppb)	Ce (ppb)	Pr (ppb)	Nd (ppb)	Sm (ppb)	Eu (ppb)	Gd (ppb)	Tb (ppb)	Dy (ppb)	Ho (ppb)	Er (ppb)	Tm (ppb)	Yb (ppb)	Lu (ppb)	ΣREE (ppm)	Ce/Ce*	
3344.6	n	11	5	5	5	6	6		6	6	6			6		6		6		6	6	
	Mean	134	651	653	5.5	3411	6387		3447	869	310			494		140		119		15	0.86	
	S.D	117	88	257	3.5	1485	2237		885	269	73			141		91		39		5	0.05	
	Max	397	819	1114	10.6	5818	10296		4945	1208	426			630		289		192		24	0.93	
	Min	37	569	444	1.6	1874	3382		2050	546	183			257		30		64		8	0.79	
3367.8	n	11	4	4	4	7	7		7	7	7			7		7		7		7	7	
	Mean	40	338	1725	7.9	520	1359		994	315	70			114		26		27		4	0.90	
	S.D	9	31	60	1.9	219	296		148	64	19			24		16		15		0.5	0.11	
	Max	58	374	1759	11.1	885	1942		1183	378	104			141		50		45		5	0.09	
	Min	28	295	1621	6.2	249	1015		750	176	44			77		6		5		3	0.78	
3371.1	n	13	5	5	5	13	13		13	13	13			13		13		13		13	13	
	Mean	120	222	1145	1.6	2881	5644		3234	962	273			526		202		199		14	0.86	
	S.D	58	29	623	0.6	2837	6158		2998	913	251			549		201		223		14	0.18	
	Max	225	243	2260	2.5	8941	18967		9997	2877	798			1642		600		693		44	0.90	
	Min	44	181	640	0.8	346	669		549	227	49			98		38		36		2	0.71	
3379.1	n	16	6	6	6	10	10		10	10	10			10		10		10		10	10	
	Mean	225	61	1572	0.4	1158	2230		1576	604	167			241		119		79		6	0.78	
	S.D	126	8	549	0.2	695	1059		662	318	117			107		151		44		3	0.07	
	Max	494	77	1964	0.6	3027	4689		2784	1297	491			470		538		152		12	0.95	
	Min	70	54	446	0.2	433	889		825	227	75			115		14		21		3	0.38	
3386.5	n	10	4	4	4	8	8		8	8	8			8		8		8		8	8	
	Mean	60	1527	1436	22.4	1229	2389		1443	481	166			295		130		163		6	0.84	
	S.D	28	296	627	10.2	1573	3220		1985	646	201			369		128		171		10	0.10	
	Max	127	1769	2218	36.4	5155	10358		6464	2019	601			1072		375		453		26	0.98	

Table 3.6 continued

	Min	34	1022	676	8.1	124	211		81	24	29		17	17	36	1	0.76			
Seawater	Value					691	787	118	479	96	22	122	19	125	30	90	77	12	3	0.59
River Water	Value(ppm)					39.6	80.9		36.4	6.9	1.4	5.3		4.2	2.0	1.7	0.3	179	0.97	

Table 3.6: Statistics of minor and rare earth element (REE) contents of calcite cements. The REE values of seawater from Nothdurft (2004) and those of river water from Goldstein and Jacobsen (1988) are also included. The Ce/Ce* is calculated based on de Baar et al (1985).

CHAPTER IV

DISCUSSION

4.1 Diagenesis and Paragenetic Sequence

4.1.1 Introduction

The post-depositional diagenetic changes in clastic rocks and their impact on reservoir quality have been studied by many authors (Blatt, 1979; Bjørlykke, 1983; Pettijohn et al, 1987; Worden and Burley, 2003; Taylor et al., 2010; Morad et al., 2010). The paragenetic sequence is a chronological order of the main diagenetic events that occurred during the burial history of sediments. It is based on the relationship between the rock components concluded from petrographic examination (Worden and Burley, 2003; Boggs, 2009). For instance, cemented sandstones with high volumes of minus-cements porosity (intergranular volume, IGV) tend to indicate that cement has precipitated before burial compaction. The early-formed cement to some extent appears to retard the rate of the compaction and constrains the subsequent rock-fluid contact. Therefore, reconstruction and interpretation of the sequence of diagenetic processes is a significant segment in reservoir diagenetic history.

The Ti-3 member sandstones formed through a fining-upward depositional cycle that occurred in a fluvial to estuarine environment (fluvio-marine) during a transgression (Haynes et al., 2013). Mud and clay (matrix) in the sandstones were likely washed away in the high hydrodynamic fluvial environment, while more silt and mud drapes occurred in the estuarine environment (Clifton, 1982). A shift from fluvial to estuarine settings created a wider and muddier down channel with mixing of marine and fresh waters (Cobb, 1993). The relatively rapid initial subsidence accelerated clastic sedimentation into suboxic/anoxic zones.

Geochemical changes based on the availability of organic matter and concentration of oxygen and sulphates had been discussed by Curtis (1978), Berner (1981), Coleman and Raiswell (1993) and Morad (1998). These restricted zones can be subdivided into bacterial sulphate-reduction zone, microbial methanogenesis zone and thermal decarbonylation zone.

Morad et al (2010) proposed that carbonate cement is pervasive in transgressive system tract sandstones because of abundance of carbonate bioclasts and organic matter with lower sedimentary rates. Studies conducted by Taylor et al (2000), Al-Ramadan et al (2005) and Taylor et al (2010) indicate that there is a broad link between carbonate cementation and the changing of sea-level. The source of carbonate cements can also be externally provided by fluids containing calcium and biogenic carbonate from overlying calcareous mudstone (Dutton et al., 2003).

Figure 4.1 summarizes the paragenetic sequence for the Ti-3 sandstones based on petrographic relationships. The current compositions of sandstones are likely altered relative to those at the time of deposition due to diagenetic processes (e.g. Burley et al, 1985; Brown et al., 1989). The general paragenetic sequence of sandstones inferred from petrographic examination is as follows: (1) early leaching of unstable minerals by meteoric waters, (2) corrosion of quartz grains followed by precipitation of siderite, (3) pervasive precipitation of calcite cements along with early pyrite, (4) major calcite cement dissolution due to migration of hydrocarbon, and (5) precipitation of minor dolomite and late pyrite.

4.1.2 Quartz Overgrowth

Minor quartz grains with silica overgrowths were enclosed by poikilotopic calcite cements (Figure 3.3 d), which indicates that some overgrowths predated massive calcite cementation. Early silica overgrowths may also be inherited since the Flemish Pass sandstones are possibly

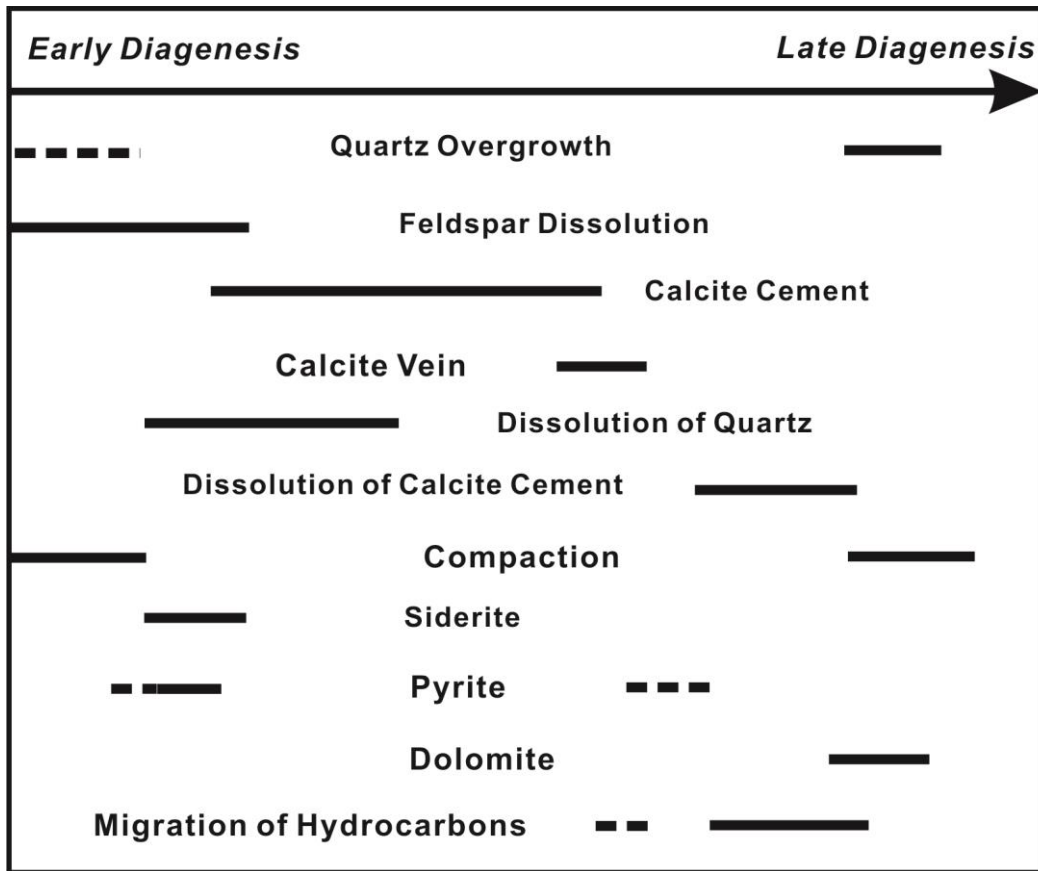


Figure 4.1: Paragenetic sequence of the Ti-3 sandstones of the Bodhrán Formation based on petrographic relationships.

derived from reworked sediments particularly when the overgrowths are scarce and have abraded morphology (e.g., Hutcheon et al., 1985; Pettijohn et al., 1987; Brown, et al., 1989; Lowe et al., 2011; Basu et al., 2013). The infrequent occurrence of silica overgrowths in pervasive calcite cemented intervals suggests that the precipitation of early calcite might have inhibited quartz from forming syntaxial overgrowths.

However, some silica cements might also occur at the late diagenetic stage after calcite dissolution as indicated by the euhedral texture of some overgrowths and the absence of poikilotopic calcite around them (Figure 3.3 c). McBride (1989) and Bjørlykke and Egeberg (1993) suggested that the chemical compaction is an essential process for providing silica

sources for quartz overgrowths in deep burial settings. However, sutured grain-grain contacts are very rare in the Ti-3 sandstones and thus the extra silica unlikely originated from pressure solution but provided by fluids released from adjacent silty mudstone beddings in the sequence by mechanical compaction (e.g., Bjørlykke et al., 1979; McBride, 1989) or in-situ dissolution of feldspars (e.g., Walderhaug, 1990; Worden and Morad, 2000). In addition, silica released from local dissolution of quartz and/or mica is possibly another supply (e.g., Walker, 1960; McBride, 1989).

4.1.3 Quartz Grain Corrosion

The quartz grains exhibit dissolution textures in association with poikilotopic calcite precipitation. They appear with irregular pitted, corroded grain boundaries, and embayment margins (Figure 3.3 b). Some edges of corroded quartz exhibit a sign of partial replacement (Figure 3.3 e).

This process occurs alkaline conditions, which suit for calcite precipitation and usually occurs in sedimentary rocks that have not been deeply buried (e.g., Epstein and Freidman, 1982; Normore, 2006; Zaid and Gahtani, 2015). Earlier studies of the same feature (Friedman et al., 1976, Bennett and Siegel, 1987; Gorbushina and Palinska, 1999) suggested that the increased pH produced by biological activities facilitate the dissolution of silica and silicate minerals (e.g., quartz, feldspar). Thus, co-occurring algae in the Ti-3 sandstones probably contributed to quartz corrosion since the photosynthesis by algae might have enhanced the alkaline conditions as well as supersaturated fluids with respect to calcite (e.g., Friedman et al., 1976; Epstein and Freidman, 1982; Brehm et al., 2005). The quartz deposited in shallow marine sediments exhibits the same corrosion textures similar to those formed in the lab condition by biofilm growth (Brehm et al., 2005), which supports that microbial activities are capable of quartz breakdown. However, high

alkaline environment is not common in nature and quartz dissolution could be therefore carried out by causes other than pH variations such as the crystallography and free energy of the quartz grains, which can be a potential sub-factor contributing to the extent of dissolution (Burley and Kantorowicz, 1986).

Accordingly, it suggests that quartz grain dissolution commenced with the precipitation of calcite cement associated with late biological activity and/or possible alkaline condition.

4.1.4 Calcite Cementation

Petrographic examination suggests that the poikilotopic calcite was precipitated during an early stage of burial, which is inferred by high intergranular volume (IGV; ~32%; Appendix 1), commonly well-preserved bioclasts, and loosely compacted framework grains with “floating” texture (Figure 3.2 a; e.g., Loucks et al., 1977; Hesse and Abid, 1998; Wanas, 2008; Liu et al., 2014; Nyman et al., 2014). The continuous twinning planes passing through sediment grains (Figure 3.7 d) suggest that the cement engulfed those grains in-situ (Blamey et al., 2014).

Similar early carbonate cementation has been petrographically and geochemically studied in adjacent Jeanne d’Arc Basin by Hutcheon et al. (1985), Brown et al. (1989) and Hesse and Abid (1998). These studies show that as the depositional environment shifts from braided fluvial to restricted nearshore marine, the rate of deposition becomes slower and this prolonged subsidence process will benefit cement precipitation (Raiswell, 1987; Morad et al., 2010).

Fracture-filling calcite likely developed in late burial settings, which is indicated by the sharp cut and clear boundaries of the fracture through sediments (Figure 3.8 c). Minor bluish fluorescent spots can be traced in the calcite cements under ultraviolet light (Figure 4.2 a), which

may indicate relatively early emplacement of hydrocarbon following calcite precipitation (e.g., Parnell et al., 2001).

4.1.5 Precipitation of pyrite and siderite

Based on petrographic examination, authigenic pyrite is suggested to have precipitated during both the early and late depositional stages of the Flemish Pass Ti-3 sandstones. Early pyrite occurs as replacement of bioclasts or forms on fossil fragments as subeuhedral to euhedral cubes or fine crystals. Late pyrite precipitated after calcite dissolution, filling interstitial spaces and replacing calcite remnants (Figure 3.9 b-d). Emery and Rittienberg (1952), Love (1967), Curtis (1978) and Morad (1998) demonstrated that the formation of pyrite in marine sediments need to occur in the bacterial sulphate reduction (BSR) regime, in which anaerobic bacteria is active, reducing sulphate to sulphur. Therefore, relatively slow burial rate associated with nearshore marine depositional environment allows sediments to enter into sulphate reduction zone, which results in the precipitation of early pyrite. Worden et al. (2003) suggested that thermochemical sulphate reduction can be another H₂S-generating processes when sediments are deeply buried (over 3500m), at temperature of >120°C. Based on the burial depth of the Ti-3 sandstones (3300-3400m) and higher homogenization temperature (T_h) of two-phase fluid inclusion in the fracture-filling (Table 3.3), this thermal-reduction scenario could be response for late formed pyrite after calcite dissolution. To confirm this, basinal sedimentary history and sulfur isotope ratios need to be examined in further studies.

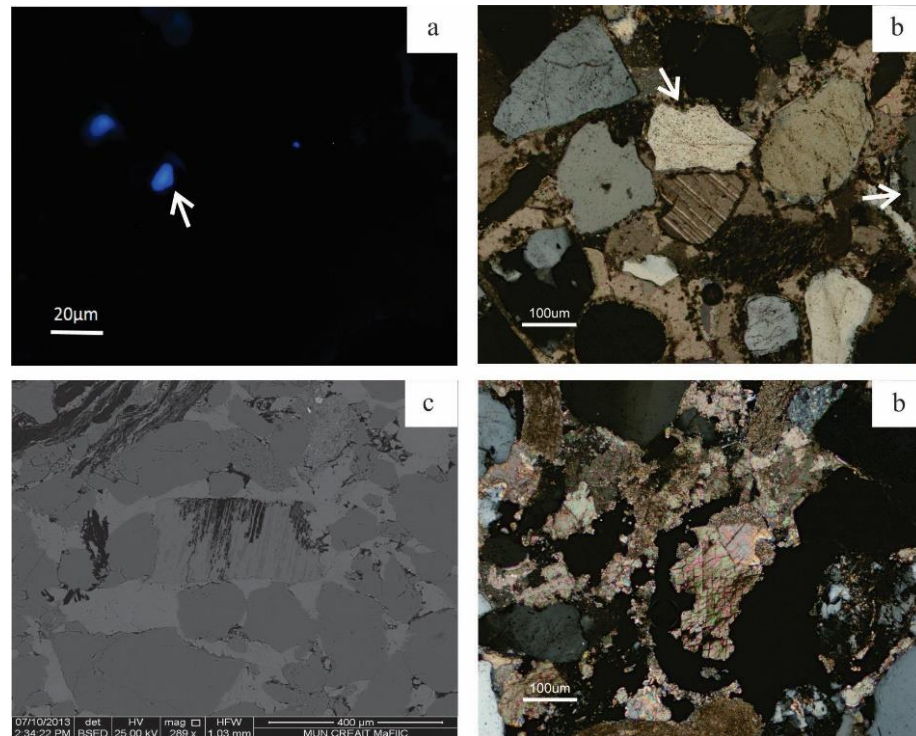


Figure 4.2: Photomicrographs of petrographic features of the Ti-3 sandstones. (a) Bluish ultraviolet fluorescence (arrow) in calcite cement, Sample# 3367.8, (b) Siderites growing into the corroded margin of detrital quartz, Sample# 3385.7, crossed polars, (c) Preferential dissolution along the replaced cleavage planes of albitized K-feldspar, Sample# 3382.8, SEM, and (d) Partially dissolved calcite resulting in development of secondary pores, Sample# 3382.8, crossed polars.

Spherulitic siderite is disseminated in calcite cements and occur as grain-rimming of framework grains. Petrographic examination reveals spherulitic siderites that followed quartz corrosion since some siderite grains occur along the quartz embayment (Figure 4.2 b). The occurrence of contacts between embayed qtz grains and siderite might indicate that the pore fluid that corroded the qtz was the source for both the siderite precipitation and then calcite precipitation. Normally, siderite occurs after deposition of early pyrite, in more reduced microbial methanogenesis zone (Gautier and Claypool, 1984; Curtis, 1978). Alternatively, siderite may have formed in the regime of sulphate reduction when the rate of Fe^{3+} reduction

exceeds the rate of sulphate reduction (Pye et al., 1990). The dull CL of samples having both calcite and siderite (Figure 3.7 f and 3.8 a) indicates precipitation from Fe-rich pore water.

4.1.6 Precipitation of dolomite

Authigenic dolomite usually occurs in the investigated sandstone intervals that lack calcite cements (Figure 3.8 d, e). In addition, authigenic dolomite can grow as a rim outside calcite remnants (Figure 3.8 f). These indicate that dolomite was formed after the onset of calcite dissolution. In the relatively late stages of diagenesis, some altered minerals (e.g., silicates) may supply sufficient Mg^{2+} ions; therefore, the essential Mg^{2+} source for forming dolomite was likely provided from outside system, such as the trapped marine water (Giroir et al., 1989).

4.1.7 Albitization of K-Feldspars

Petrographically, most of partial albitized k-feldspars are engulfed by poikilotopic calcite cements (Figure 3.4 b). Since early precipitated calcite tends to impede fluids exchange, it implies that the albitization happens before or during calcite precipitation. Interpretation of the origin of albitization is not included in this research; nevertheless, we provide two possible hypotheses for its generation. Morad et al (1990) and Baccar et al (1993) explain that albitization of K-feldspar appears more likely at greater burial and higher temperatures ($>90^{\circ}C$). We can therefore assume that albitization may be provenance-related, and inherited from source rocks due to the petrographic evidence (monophase inclusions) of early cementation at low temperatures. Another hypothesis is that the albitization may occur in situ as diagenetic product, as Saigal et al (1988) and González-Acebrón et al (2010) document that albitization can start at relatively lower temperature from 60 to $83^{\circ}C$. Sodium could be sourced from seawater, conversion of smectite-to-illite in the interbedded shales and detrital sodium plagioclase dissolution (Land, 1984; Abid et al., 2004; González-Acebrón et al., 2010).

4.1.8 Dissolution

Two main episodes of dissolution during diagenesis have been recognized in this study. Petrographic examinations suggest minor partially-dissolved feldspar residuals occurring in the early calcite cement appear to provide a scenario of early dissolution due to meteoric water leaching (Figure 3.3 f). The albitized K-feldspars retain skeletal textures, suggesting that the leaching started along cleavage planes (Figure 4.2 d). In addition, illite is recorded in some samples filling in the secondary pores close to feldspar remnants (Figure 3.7 b).

A second major dissolution has followed the precipitation of poikilotopic calcite cement. It happened at late diagenetic stage, and is recorded by the occurrence of corroded quartz in uncemented intervals, abundant secondary pores and remnants of calcite cement crystals (Figure 4.2 d and Figure 4.3 a). This large-scale dissolution affects not only calcite cement, but also framework and accessory minerals and, therefore, altered the original composition of the sandstone. Diagenetic fluids responsible for this major dissolution are possibly related to up-moving acids generated from the maturation of hydrocarbon (e.g., Brown et al., 1989; Taylor et al., 2000; Dutton, 2008). In addition, Taylor et al. (2000) had discovered that uncemented leaching zones appear to be underlain coal beds in Book Cliffs, Utah-Colorado. Since coal stringers can be traced in the upper section of Ti-3 Member of the Bodhrán Formation (Figure 2.1; C-NLOPB, 2014), it suggests that organic acids generated from coals could also be responsible for calcite dissolution. This late stage calcite dissolution effectively improves porosity and permeability of the investigated clastic interval.

4.1.9 Compaction

Although the early calcite cement has, to some extent, retarded mechanical compaction by the overlying sediment loads, microcracks are still occurred in some detrital quartz (Figure 4.3 b).

Minor quartz grains are even fractured, and enclosed by poikilotopic calcite (Figure 4.3 c). This suggests that the early calcite cementation occurred after the onset of burial, which caused quartz grains to fracture. In some uncemented intervals, a few quartz grains exhibit concavo-convex or sutured contacts (Figure 4.3 d), which is consistent with the expected continuous compaction with progressive burial after major calcite dissolution.

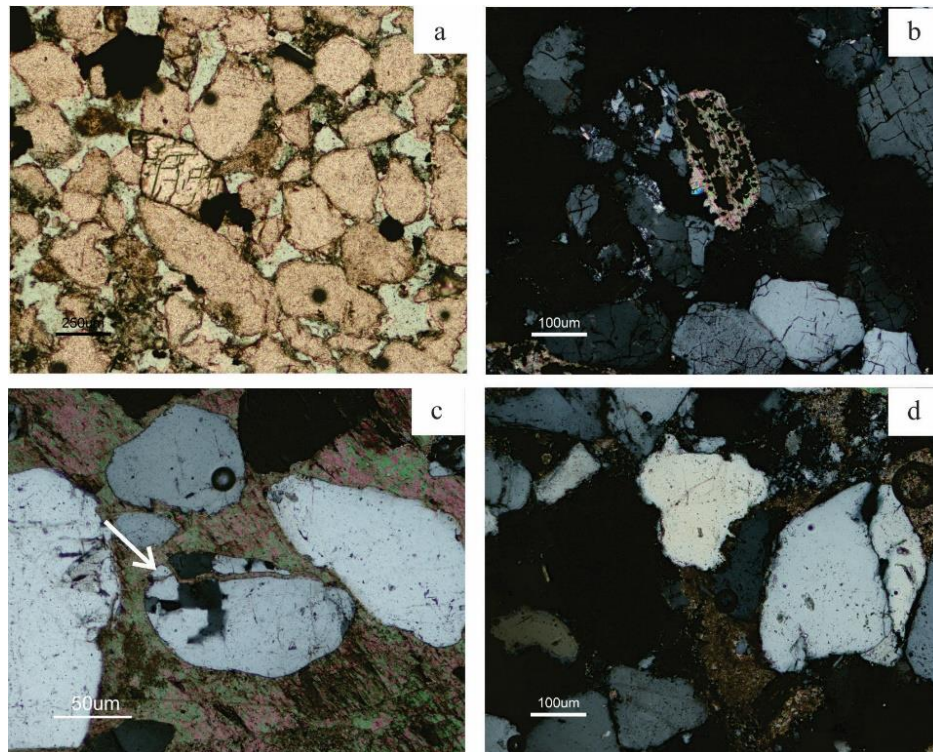


Figure 4.3: Photomicrographs of petrographic features of the Ti-3 sandstones. (a) Cement remnant, Sample# 3339.3, polarized light, (b) Microcracks occurring in quartz grains, Sample# 3387.8, crossed polars, (c) Quartz fracture healed by calcite cement (arrow), Sample# 3379.7, crossed polars, and (d) Sutured grain contact, Sample# 3382.8, crossed polars.

4.2 Origin of Calcite Cement

Similar early diagenetic calcite has been also documented and studied in the Jeane d'Arc Basin by Hutcheon et al (1985), Brown et al (1989), Hesse and Abid (1998). This cement may have formed by the recrystallization of micritic cements (Saigal and Bjorlykke, 1987), due to the

dissolution and recrystallization of abundant bioclasts (e.g., Bjørkum and Walderhaug, 1990; McBride et al., 1995). A previous depositional study suggested that the presumed transgressive nature of this depositional sequence would bring saline waters into sediments originally filled with mixed fresh-saline fluids (estuarine) and, eventually, into sediments originally filled with fresh waters (the lower fluvial section) (Haynes et al., 2013). When depositional environment shifts from braided fluvial upward to restricted nearshore marine, the rate of deposition became slower and this prolonged subsidence would have enhanced calcite cement precipitation (Raiswell, 1987; Morad et al., 2010).

4.2.1 Oxygen and Carbon Isotopes

Stable isotope analysis of oxygen and carbon is an essential tool for better understanding the depositional environments and diagenetic history of sedimentary rocks, since oxygen and carbon isotope compositions record changes in diagenetic environments (Anderson and Arthur, 1983; Longstaffe, 1983). Oxygen and carbon isotopes are used in this study for the interpretation of origin of calcite cements in Ti-3 sandstones.

Longstaffe (1987) and Morad et al. (1990) showed that variations of oxygen isotopic ratios in carbonates are influenced by (1) oxygen composition and salinity of pore-fluids during deposition; (2) temperature of deposition; and (3) water-rock interaction ratio (closed vs. open system).

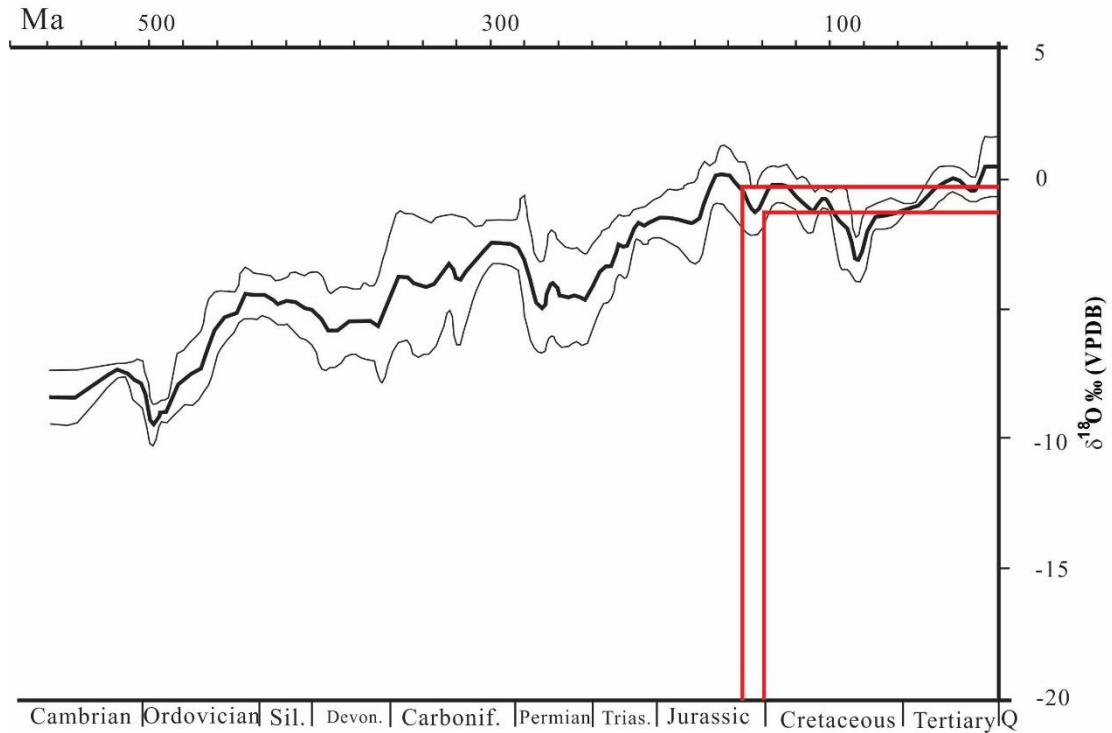


Figure 4.4: Phanerozoic $\delta^{18}\text{O}$ trend of well-preserved marine biogenic carbonates. An estimated range of $\delta^{18}\text{O}$ of -1.5 to -0.5‰ VPDB during the Tithonian. The outlining area around the mean include 68% of all data (modified from Veizer et al., 1999).

Veizer et al (1999) reconstructed the $\delta^{18}\text{O}$ Phanerozoic trend in seawater using well-preserved biogenic carbonates (Figure 4.4). The estimated $\delta^{18}\text{O}$ values of Thithonian seawater are between -0.5 to -1.5‰ VPDB (Figure 4.4). Wilkinson (1991) conducted a stable isotopic study on calcite concretions in Jurassic sandstones and provided interpretations regarding different $\delta^{18}\text{O}$ values: -6 to -10‰ of $\delta^{18}\text{O}$ VPDB of calcite cement sourced from meteoric fluids, -4 to -6‰ of $\delta^{18}\text{O}$ VPDB of calcite cement sourced from mixed marine-meteoric waters, and -1 to -4‰ of $\delta^{18}\text{O}$ VPDB of calcite cement sourced from marine pore-waters. Wadleigh and Veizer (1992) suggested that post-depositional processes that result in $\delta^{18}\text{O}$ -enrichment are rare. The $\delta^{18}\text{O}$ ratios in diagenetic carbonates normally exhibit a depletion trend because alteration is commonly influenced by meteoric waters or occurred at elevated temperatures (e.g., Land, 1980;

Machemer and Hutcheon, 1988; Scotchman, 1991; Mozley and Burns, 1993; Veizer et al., 1997; Longinelli et al., 2002). Land (1995) denoted that meteoric and burial diagenesis could shift the $\delta^{18}\text{O}$ of sediments toward lower values during depositional period. Friedman and O'Neil (1977) establish a relation between diagenetic evolution of calcite, parent fluids and temperature:

$$1000\ln\alpha_{\text{calcite-fluid}}=2.78*10^6*T^{-2}-2.89,$$

$$\text{Where } \alpha_{\text{calcite-fluid}}=(1+(\delta^{18}\text{O}_{\text{calcite}}/1000))/(1+(\delta^{18}\text{O}_{\text{fluid}}/1000)).$$

Therefore, the oxygen isotopic composition of diagenetic fluids can be estimated by using the abovementioned formula.

The oxygen isotopic compositions for intergranular calcite cements (-11.0 to -5.3‰ VPDB; Figure 4.5) are significantly lower than the composition of the best preserved Tithonian marine carbonates (-1.5 to -0.5‰ VPDB; Veizer et al., 1999). As the mixing marine water with meteoric fluids might account for a similar depletion of $\delta^{18}\text{O}$ values in an offshore environment (e.g., Hutcheon et al., 1985; Scotchman, 1991; Land, 1995). This implies that the calcite cement in the Ti-3 sandstones precipitated from modified marine waters of most likely a fluvio-shallow marine environment (e.g., Hesse and Abid, 1998, Haynes et al., 2013). The $\delta^{18}\text{O}$ values of fracture-filling calcites tend to be more depleted relative to their intergranular counterparts (Figure 4.5). This implies that they formed in later burial setting of higher temperature, which is consistent with their petrographic features. Very few $\delta^{18}\text{O}$ values of intergranular calcite are depleted as those of the fracture-filling one indicates that poikilotopic calcite continuously precipitated during the progressive burial.

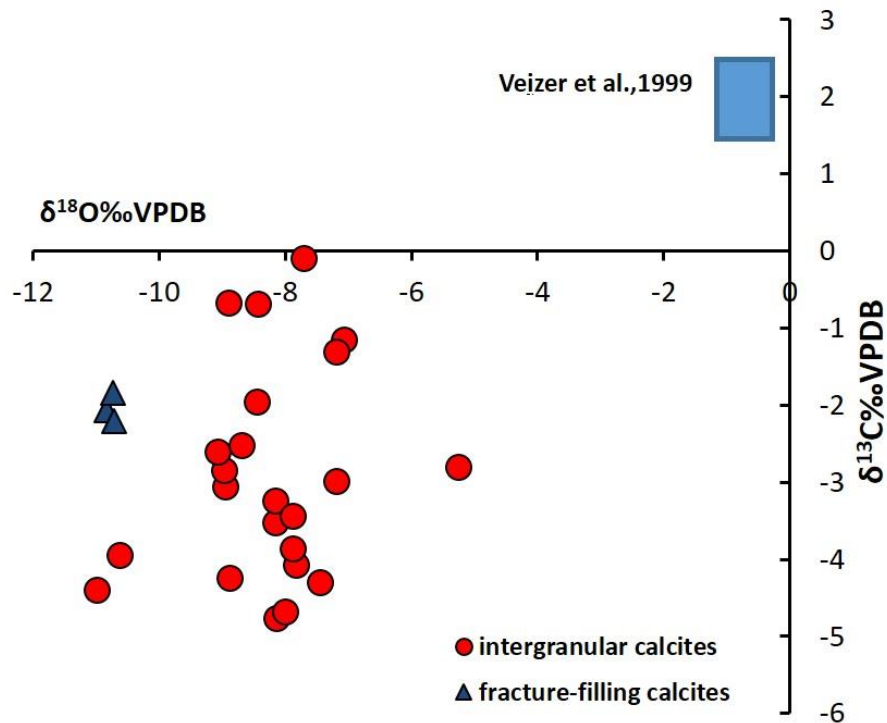


Figure 4.5: Scatter diagram of $\delta^{18}\text{O}$ vs. $\delta^{13}\text{C}$ for calcite cements. The square represents the estimated range of isotopic composition of well-preserved marine carbonates during the Tithonian Stage (Veizer et al., 1999).

The occurrence of all-liquid fluid inclusions particularly in the core of those intergranular cement crystals suggests that they precipitated at near surface temperature possibly between 25 and 40°C (Goldstein and Reynolds, 1994; Hesse and Abid, 1998; Azomani et al., 2013; Nyman et al., 2014). However, the crystals grew with progressive burial as indicated by the entrapment of primary two-phase fluid inclusions along the rims of some of those crystals. Using the equation of Friedman and O'Neil (1977) the oxygen isotopic composition of the parent fluids of the calcite cements has been calculated with the calcite-water equilibrium relationship based on temperature shown in Figure 4.6. The measured $\delta^{18}\text{O}$ of the early

calcite cements and their suggested approximate temperature of precipitation (25-40°C) imply that the $\delta^{18}\text{O}$ values of their parent diagenetic fluids approximately between -8 and 1.1‰ VSMOW (Figure 4.6). Clark and Fritz (1997) suggested that the average $\delta^{18}\text{O}$ value of present-day meteoric waters is ~4‰ VSMOW lower than that of modern tropical seawater. Assuming that this difference was consistent during the Jurassic times, the $\delta^{18}\text{O}$ values of Jurassic meteoric waters would be -5 to -4‰ VSMOW assuming the $\delta^{18}\text{O}$ values of Jurassic marine water ranged from -1 to 0‰ VSMOW (e.g., Shackleton and Kennett, 1975; Holmden and Hudson, 2003; Brigaud et al., 2009). Thus, the estimated $\delta^{18}\text{O}$ values of diagenetic fluids generally fall within the range between the values of the Jurassic marine water and that of meteoric waters. Calculated low salinity estimates for all-liquid fluid inclusions (Table 3.3; 3.5 eq. wt.% NaCl for modern sea water salinity) also support the precipitation from a mix of marine and meteoric waters, which is also consistent with sediments' fluvio-estuarine depositional facies (Haynes et al., 2013). However, the $\delta^{18}\text{O}$ and T_h values of the calcite cements with primary two-phase fluid inclusions (some intergranular and fracture-filling) reflect hydrothermal ^{18}O -enriched parent fluids (-1.2 to 10.3‰ VSMOW; Figure 4.6), which is expected for circulated hot basinal fluids of relatively deeper burial settings (e.g., Azmy et al. 2009; Conliffe et al., 2010; Azomani et al., 2013; Olanipekun et al., 2014). This is also consistent with the fracture-filling calcite that yields even higher T_h values and salinities estimates (Table 3.3). In summary, the $\delta^{18}\text{O}$ composition of the intergranular and deep burial fracture-filling calcite cements suggest that they primarily precipitated from mixed marine and meteoric waters that became hotter and more ^{18}O -enriched with progressive burial and circulation in the basin. Figure 4.7 shows a brief sketch that summarizes the stages of fluid inclusions formation in the investigated cements, based on petrographic and stable isotope analyses.

Carbon-isotope ratios are used to trace carbon sources and, therefore, to interpret the origin of carbonates. The $\delta^{13}\text{C}$ values of carbonate cements generally fall within -12 to 4‰ (Talma and Netterberg, 1983). Carbonates of biogenic origin have $\delta^{13}\text{C}$ values of -4‰ to -11‰ VPDB (Mack et al., 1991; Spötl and Wright, 1992). Carbonates sourced from organics have more depleted $\delta^{13}\text{C}$ values, ranging from -33 to -18‰ (Mack et al., 1991). Veizer et al (1999) reconstructed the $\delta^{13}\text{C}$ profile of the Phanerozoic seawater (Figure 4.8), the Thithonian seawater has estimated $\delta^{13}\text{C}$ values of +1.6 to +2.5‰ VPDB (Figure 4.8).

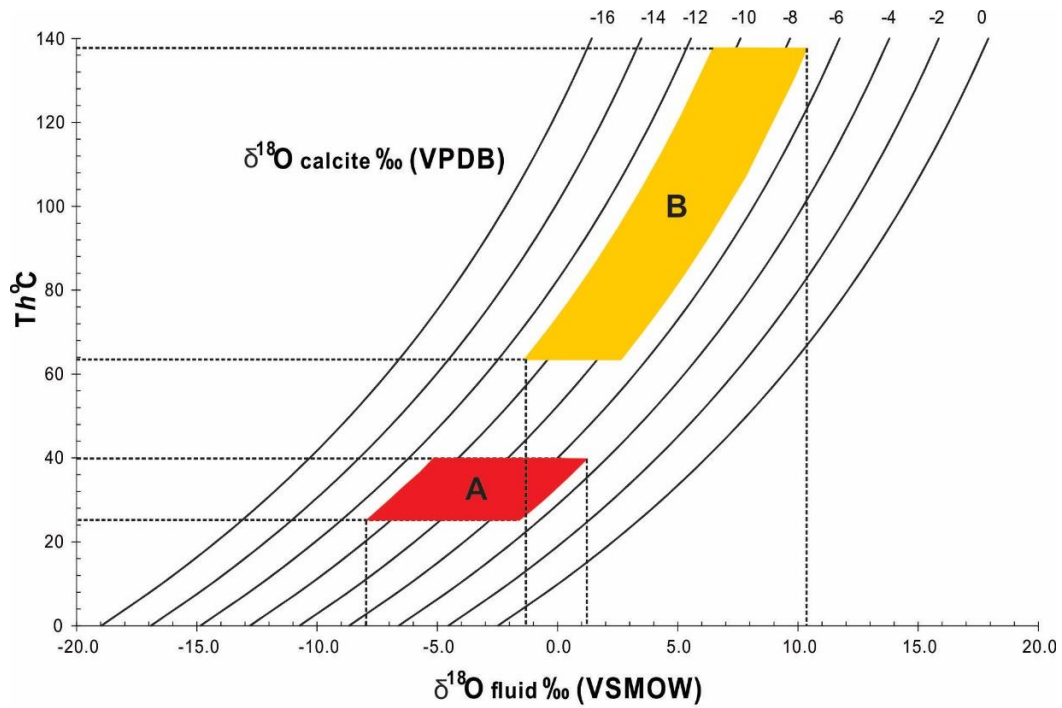


Figure 4.6: Temperature (T) vs. $\delta^{18}\text{O}_{\text{digenetic fluid}}$ for various $\delta^{18}\text{O}_{\text{calcite}}$ values that were reconstructed from the following equation: $10^3 \ln a_{(\text{calcite-water})} = 2.78 \cdot 10^6 T^{-2} - 2.89$ (Friedman and O'Neil, 1977). The vertical bars indicate the $\delta^{18}\text{O}_{\text{fluid}}$ compositions based on the ranges of $\delta^{18}\text{O}_{\text{calcite}}$ values and homogenization Temperature (T_h) of each identified calcite cement phase. Details in text. Field A refers to the early intergranular poikilotopic calcite and B to the late and fracture-filling calcite.

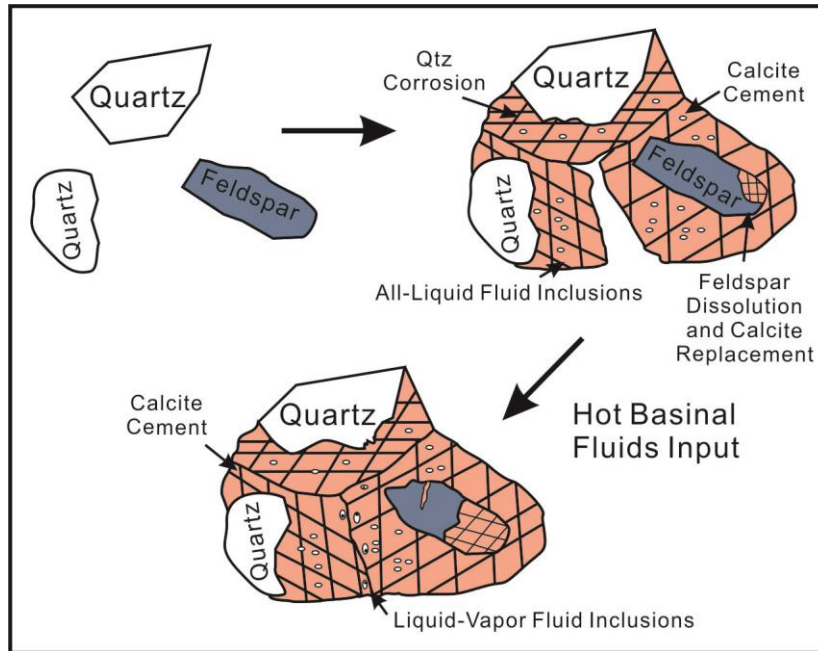


Figure 4.7: Schematic diagram summarizing the stages of formation of fluid inclusions in the calcite cements of the investigated sandstones. All-liquid fluid inclusions occur in the cores of poikilotopic calcite that precipitated at shallow burial, while liquid-vapor fluid inclusions form later in the crystal rims with progressive burial.

Morad (1998) proposed geochemical zones for marine carbonates during progressive burial, each with distinctive carbon isotopic signatures. In oxic zone, carbon is sourced from the decay of plants and atmospheric CO_2 , with values normally between -10 to -3‰ . Marine oxic carbonates have similar $\delta^{13}\text{C}$ contents to those of seawater during their time of precipitation. The $\delta^{13}\text{C}$ values of suboxic marine carbonates ($>-6\text{‰}$) are influenced by seawater and the oxidation of organic matter. The $\delta^{13}\text{C}$ values of marine carbonates formed in the bacterial sulphate reduction zone are also dominated by the oxidation of organic matter as well as dissolution of biogenic carbonates. Due to isotopic fractionation during microbial methanogenesis, CO_2 inherits heavy $\delta^{13}\text{C}$ up to $+15\text{‰}$ (Irwin et al., 1977). In the later thermocatalytic decarboxylation zone, carbonate can be precipitated in the early stage of degradation of organic matter due to buffering carboxylic acids (Morad, 1998). The carbon is sourced from organic matter resulting in light

$\delta^{13}\text{C}$ values. This thermocatalytic decarboxylation requires higher temperature (120-150°C; Hesse, 1990).

Biogenic carbonates are one of major sources for carbonate cements in sandstones or mudstones since the Upper Jurassic sandstones often contain plentiful calcite cements that were mainly sourced from calcareous organisms on the sea-floor (e.g., Bjørlykke and Jahren, 2010). The carbon isotopic values of the currently investigated calcites range between -4.8 to -0.1‰ VPDB, which imply that they were originated mostly from seawater and dissolution of bioclasts (e.g. Hesse and Abid, 1998; Wanas, 2008; Dutton et al., 2012; Nyman et al., 2014). The lack of significantly depleted $\delta^{13}\text{C}$ values $< -20\text{‰}$) implies that the carbon was not derived from thermocatalytic decarboxylation of organic matter (Irwin et al., 1977). However, the decarboxylation of organic matter during early burial stage may have released light (^{12}C -enriched) CO_2 , which explains some of the slightly low $\delta^{13}\text{C}$ values of the Ti-3 sandstones calcites (Figure 4.6; Irwin et al., 1977; Morad, 1998; Faure and Mensing, 2005). The abundance of bioclasts within the Ti-3 sandstones provides a solid evidence for a biogenic origin of calcite cements. In addition, calcareous siltstones adjacent to the Ti-3 sandstones (Figure 2.1) may provide additional external sources for the calcite via pore fluids expelled by compaction (e.g. Dutton et al., 2000; McBride et al., 1995). The Ca^{2+} can be also provided by the early dissolution of plagioclase, although its occurrence in Ti-3 sandstones is limited.

4.2.2 Minor and Rear Earth Elements

It is well known that Fe and Mn concentrations are the major factor controlling the luminescent degree in diagenetic calcites (Barnaby and Rimstidt, 1989). Since Mn has been identified as the main activator while Fe as the quencher of luminescence, the intensity of CL is mainly controlled by the Mn/Fe ratio of calcite (Heydari and Moore., 1993). Generally, calcite

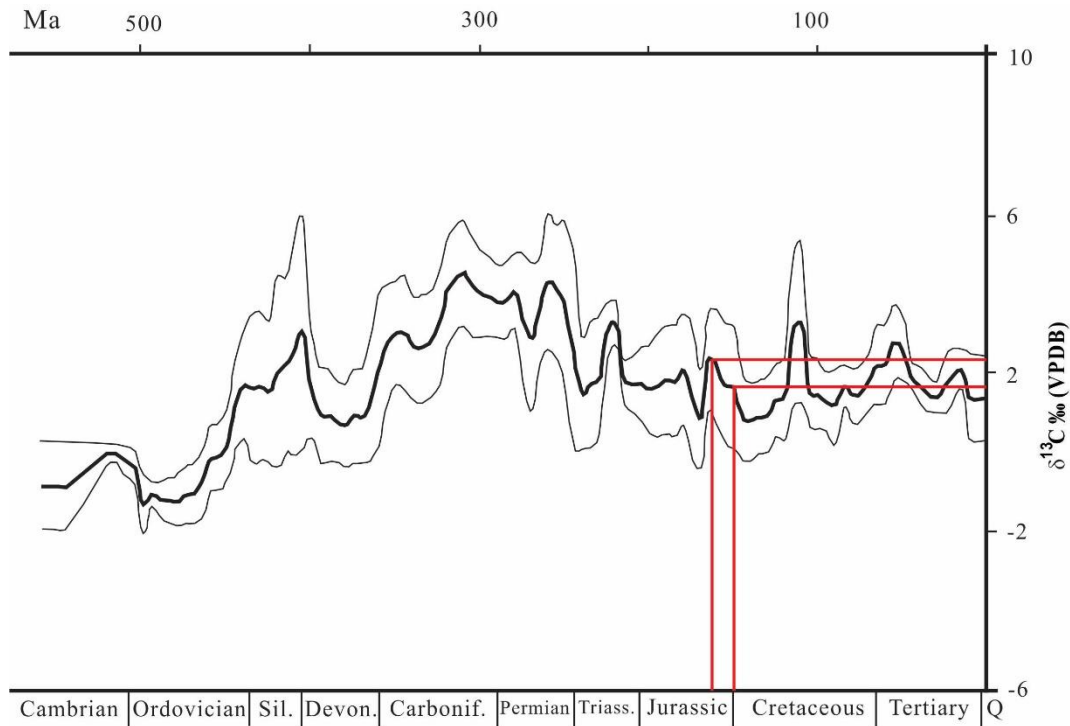


Figure 4.8: Phanerozoic $\delta^{13}\text{C}$ trend of well-preserved marine biogenic carbonates. An estimated range of $\delta^{13}\text{C}$ of 1.5 to 2.5‰ VPDB during Tithonian. The outlining area around the mean include 68% of all data (modified from Veizer et al., 1999).

with $\text{Mn} > \text{Fe}$ exhibits brighter luminescence and vice versa (Machel et al., 1991). In addition, Mn and Fe contents associated with calcite luminescence reflect the redox conditions during cement precipitation (e.g., Frank et al 1982; Barnaby and Rimstidt, 1989). The Mn contents of the intergranular calcite are commonly more enriched than Fe (Table 3.6), which is consistent with their dull/moderate to bright CL images. This implies that early-burial calcite cements with dull CL likely precipitated in shallow-burial and less reducing environment but those, which exhibit bright CL reflect the late burial settings (Figure 3.7 e). The Sr contents of the intergranular calcite cement are high (from 653 to 1725ppm), and may reflect influence of marine water (Banner, 1995; Taylor et al, 2000). High Sr concentrations ($>1000\text{ppm}$) also suggest that calcite

cement could be sourced from dissolution of aragonitic shells (e.g., Kinsman, 1969; Hutcheon et al., 1985; Dickson, 1990; Thomas et al., 2004).

Rare earth elements (REE) consist of fifteen lanthanide ions (from La to Lu) and have a relatively short oceanic residence time (less than 10^3 yrs; Alibo and Nozaki, 1999). All REE are naturally trivalent except for Cerium (Ce) and Europium (Eu) (Ce^{4+} and Eu^{2+} , respectively), which are sensitive indicators of redox conditions (e.g., Elderfield and Greaves, 1982; German and Elderfield, 1990; Sholkovitz et al., 1994; Zhong and Mucci, 1995). Since REE are lithophile elements, their compositions in the water can reflect several exogenic sources, such as, mid-ocean ridge hydrothermal circulation, atmospheric/volcanic dust deposition, precipitation/adsorption processes, and inputs from river water (e.g., Goldstein and Jacobsen, 1988; Klinkhammer et al., 1994; Holser, 1997). Therefore, REEs have been widely used as a proxy of depositional environment of sediments and redox conditions (e.g., Piper, 1974; Elderfield and Greaves, 1982; Nothdurft et al., 2004; Azmy et al., 2011). The general PAAS-normalized distribution patterns of seawater REE_{SN} (Post Archean Australian Shale; Nothdurft et al., 2004) are characterized by (1) light REE (La to Nd) depletion, (2) a negative Ce anomaly, and (3) a slight positive La anomaly (e.g., Elderfield and Greaves, 1982; Bau and Dulski, 1996; Azmy et al., 2011). De Baar et al. (1988) suggested that shallow oxic waters exhibit a negative Ce anomaly but, anoxic waters tend to show a slightly positive Ce anomaly. Sholkovitz and Schneider (1991) also indicated that Ce oxidation likely takes place in the upper ocean. This is supported by Alibo and Nozaki (1999), who studied Ce concentrations in seawater and suggested that adsorption and oxidation of Ce largely takes place in the surface water where biological activity is high. The Ce anomaly can record oxic/reducing interface instantaneously at the time of deposition (e.g., Elderfield and Sholkovitz 1987; de Baar et al., 1988; German et al., 1991).

Bau and Dulski (1996) noticed that positive Eu_{SN} anomalies could occur in Transvaal seawater, which has been influenced by high-temperature hydrothermal components. Klinkhammer et al (1994) studied several samples from deep-sea hydrothermal areas and noticed that the shale-normalized REE patterns exhibit positive Eu anomaly, but are different with seawater.

Zhong and Mucci (1995) suggested that REE have a relatively narrow range of partition coefficient values, thus variations in the series could reflect the chemical changes of fluid input and other processes. Azmy et al (2011) indicated that REE enrichment is most likely attributed to REE composition of the diagenetic fluids. Therefore, the various PAAS-normalized distribution patterns of rare earth elements (REE_{SN}) in carbonates have been utilized as a tool for identifying different diagenetic fluid compositions, since they can mimic the patterns of ambient fluids when carbonates precipitated (e.g., Azmy et al., 2011; Azomani et al., 2013). For example, the REE_{SN} trends of burial calcite cement exhibit LREE enrichment coupled with a HREE depletion resembling a “chevron” shape (Azmy et al., 2011). Nothdurft et al (2004) measured the REE_{SN} patterns of ancient limestones precipitated from coastal/estuarine waters in Western Australia, and found that they are differentiated from those of more open seawaters.

The REE_{SN} patterns of the currently investigated calcites from various depths of the studied borehole exhibit similar and almost parallel profiles (Figure 3.12). Combined with the stable isotope and fluid inclusion results, the REE results confirm that the calcite cements in the Ti-3 sandstones precipitated from the same parent diagenetic fluids that were circulated through the basin during burial. The REE_{SN} patterns of the investigated cements generally exhibit slight negative Ce anomalies and positive Eu anomalies (Figure 3.12). They are not parallel to the typical seawater profile characterized by a remarkable negative Ce anomaly and depleted LREE (light REE, La to Nd) relative to HREE (heavy REE, Ho to Lu) (Figure 3.12; e.g. Elderfield and

Greaves, 1982; Bau and Dulski, 1996; Nothdurft et al., 2004; Azmy et al., 2011), but similar to river-water profile with MREE enrichment (medium REE, Sm to Dy) (Figure 3.12; Goldstein and Jacobsen, 1988). The scenario of Ce anomaly caused by removal of Ce by Fe-hydroxides to be enriched in chlorite and sphene (e.g., Blamey et al., 2014) is unlikely, because those minerals are very rare in the Ti-3 sandstones. Alternatively, the Ce anomaly occurs in shallow seawater environment due to oxidation of soluble Ce^{3+} to insoluble Ce^{4+} through bacterial mediation (Elderfield and Greaves, 1982; German and Elderfield, 1990; Alibo and Nozaki, 1999). Thus, the Ce anomaly reflects the influence of contribution of marine water to the parent diagenetic fluids, which is consistent with the fluvio-estuarine sedimentary environment (Haynes et al., 2013) and also agrees with the suggestion of mixed meteoric and seawaters origin for the diagenetic fluids. In addition, the calculated Ce anomaly values (Table 3.6) confirm that less soluble Ce^{3+} existed in the diagenetic fluids at that period, which suggests a suboxic condition during precipitation of calcites (e.g., de Baar et al., 1988; Azomani et al., 2013). Positive Eu anomaly has been documented by earlier studies in fluids from hydrothermal vents at the seafloor and their associated carbonates (e.g., Elderfield and Greaves, 1982; Hongo and Nozaki, 2001; Bau et al 2010). Also, Sverjensky (1984) and Bau et al (2010) proposed that divalent europium (Eu^{2+}) is dominant in marine hydrothermal fluids. Thus, the positive Eu anomaly (Figure 3.12) reflects the contribution from the dissolution of plagioclase in sandstones by diagenetic fluids during burial (Lee et al., 2003; Bau et al., 2010).

4.2.3 Fluid-Inclusion Gas Analysis

Major, minor and noble gases are trapped in fluid inclusions during precipitation of crystal phase (Goldstein and Reynolds, 1994) and the compositions of those gases tend to provide additional information about the nature of parent diagenetic fluids (e.g., Giggenbach, 1986;

Norman and Musgrave, 1994; Norman and Moore, 1999; Blamey and Norman, 2002; Norman et al., 2002). Researchers have recently paid attention to the fluid-inclusion gas analysis, particularly applied to mineral exploration (e.g., Shepherd and Waters, 1984; Landis and Hofstra, 1991; Jones and Kesler, 1992; Moore et al., 2001; Mao et al., 2003; Norman and Blamey, 2005) and diagenetic studies (e.g., Azomani et al., 2013). Azomy and Blamey (2013), Azomani et al (2013) and Olanipekun et al (2014) have applied this quantitative gas analysis to carbonates to shed the light on the origin of diagenetic fluids. Azomy and Blamey (2013) tested fluid-inclusion gas analyses on marine carbonates and found the results to be consistent with previous studies, which proved that the application of fluid inclusion gas ratios is reliable. N_2/Ar ratios can be utilized in differentiating meteoric water or basinal fluids ($N_2/Ar=38$; Giggenbach, 1986) from magmatic fluids ($N_2/Ar=100\sim 1000$; Norman et al., 2002). Giggenbach (1986) introduced the N_2 -Ar-He ternary diagram to discern the sources of geothermal fluids, but because of the ambiguity of He contents the diagram had been updated by Norman et al (1996) into the N_2 -Ar- CH_4 ternary diagram. Norman and Moore (1999) showed that some gases with high N_2/Ar ratios may be interpreted as geothermal gases, despite the waters being meteoric. Therefore, they introduced the CO_2/CH_4 versus N_2/Ar diagram, which is an effective tool to differentiate between fluid sources by classifying data into three general zones: meteoric, crustal (basinal) and magmatic fluids. A field labeled the “organic” was introduced to the crustal area when Norman and Moore (1999) proved that excess nitrogen will be yielded in some geothermal systems. Blamey and Norman (2002) also introduced a N_2 , Ar and He based diagram to avoid high-nitrogen basinal fluids being falsely plotted.

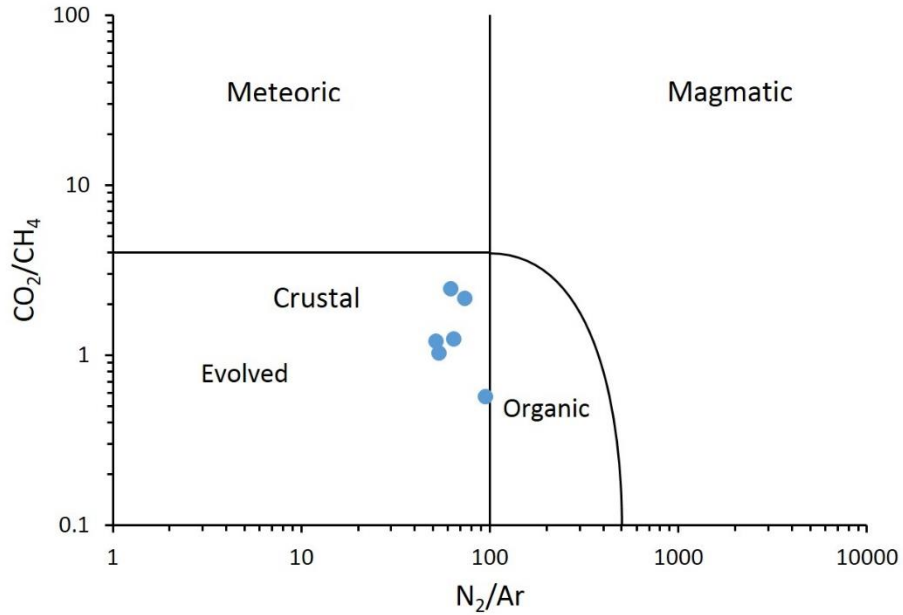


Figure 4.9: Plot of CO_2/CH_4 vs. N_2/Ar for gas-inclusion analyses of the intergranular calcite cements from the Ti-3 sandstones (modified from Norman and Moore, 1999).

The CO_2/CH_4 and N_2/Ar ratios of the calcite cements in the Ti-3 sandstones are presented in Figure 4.9, showing that all data are well constrained in the crustal zone. This suggests that calcite cements originated from crustal (basinal) fluids, i.e. modified marine fluids, which is consistent with the conclusions from stable isotopes, minor and trace elements, fluid-inclusion studies and petrography. However, one of the samples has a higher N_2/Ar ratio that plots nearly at the boundary of the “organic” field (Figure 4.9, Table 3.4), which implies that the disintegration of some organic matter might have released some extra N_2 that contributed to the ratio (Norman and Moore 1999; Azmy and Blamey, 2013). This is consistent with the correlated low CO_2/CH_4 of the same sample since N_2 and CH_4 are by products of protein decay particularly in the late stages of diagenesis (Norman and Moore, 1997, 1999; Azomani et al., 2013; Azmy and Blamey, 2013).

4.3 Impacts on Sandstone Porosity

Calcite cementation has been the focus of reservoir studies because it significantly influences the reservoir quality (e.g., Saigal and Bjørlykke, 1987; Bjørlykke et al, 1989; Taylor, 1990; Dutton et al., 2000, Longstaffe et al., 2003; Nyman et al., 2014; Liu et al., 2014). In the Ti-3 sandstones, over 75% original porosity loss was primarily due to calcite cementation (Figure 4.10). A negative correlation between calcite cement contents and porosity suggests that pervasive calcite cementation was the dominant diagenetic mineral affecting porosity reduction (Figure 4.11).

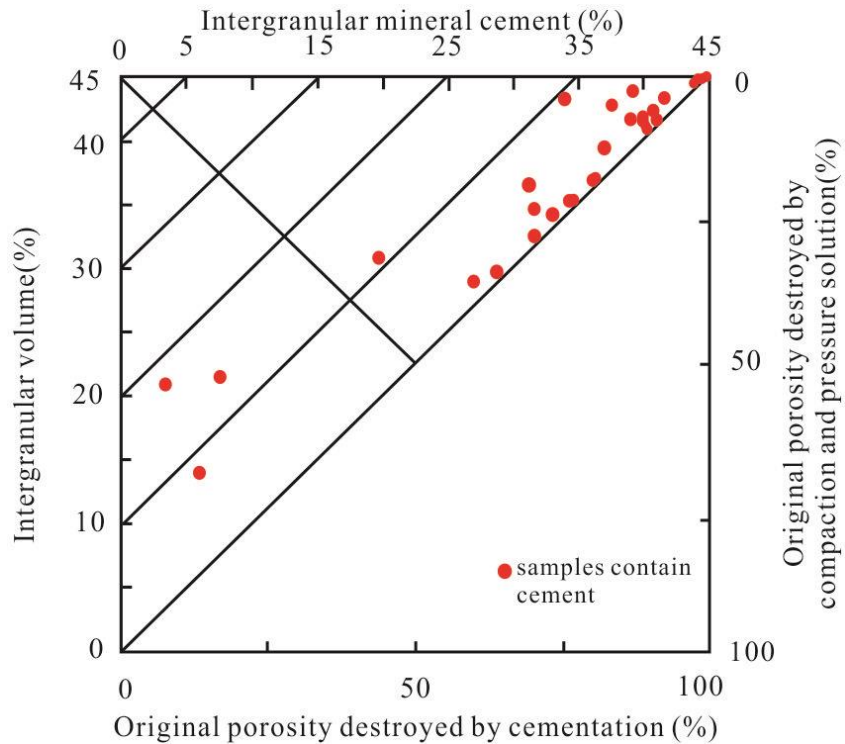


Figure 4.10: Diagram showing the intergranular volume vs. calcite cement volume in the Ti-3 sandstones, modified from Lundegard (1992).

The early precipitated calcite cement leads to rigid framework, and retards the adverse impact by overburden compaction. In addition, secondary pores and throats reopened by calcite

dissolution were important in improving reservoir quality after deep burial. In the high porosity sandstone intervals, over 90% pores are mainly secondary in origin. Successive high porosity horizons underlie silty mudstone beds with coal stringers (Figure 2.1 and Figure 4.1). Thus, the uncemented horizons may be the result of leaching process by organic acids released from coals (e.g. Percival 1983; van Keer et al., 1998; Taylor et al., 2000). The secondary porosity evolution may also be related to organic-acids produced from hydrocarbon maturation particularly when the Tithonian sandstones in the Flemish Pass Basin contain interbedded shales with 8% to 12% TOC (Haynes et al., 2012). Thus, despite well-developed early calcite cementation, some Ti-3 sandstone intervals are porous and demonstrate a good reservoir quality.

Petrographic examination indicates that oil traces (Enachescu and Geoph, 2014) exhibit signs of early emplacement of hydrocarbon. The microthermometric measurements of T_h (70 to 137 °C) provide values within the oil window (50-150°C), which implies that oil migration might have occurred prior to diagenesis completion, and the Ti-3 sandstones could have been a hydrocarbon pathway (e.g. Parnell et al., 2001). The pervasive calcite cement brings important predictions in reservoir quality; however, in order to further understand the impacts of calcite cement on a basinal scale, modeling of calcite concretion distribution need to be extensively taken into account in future studies.

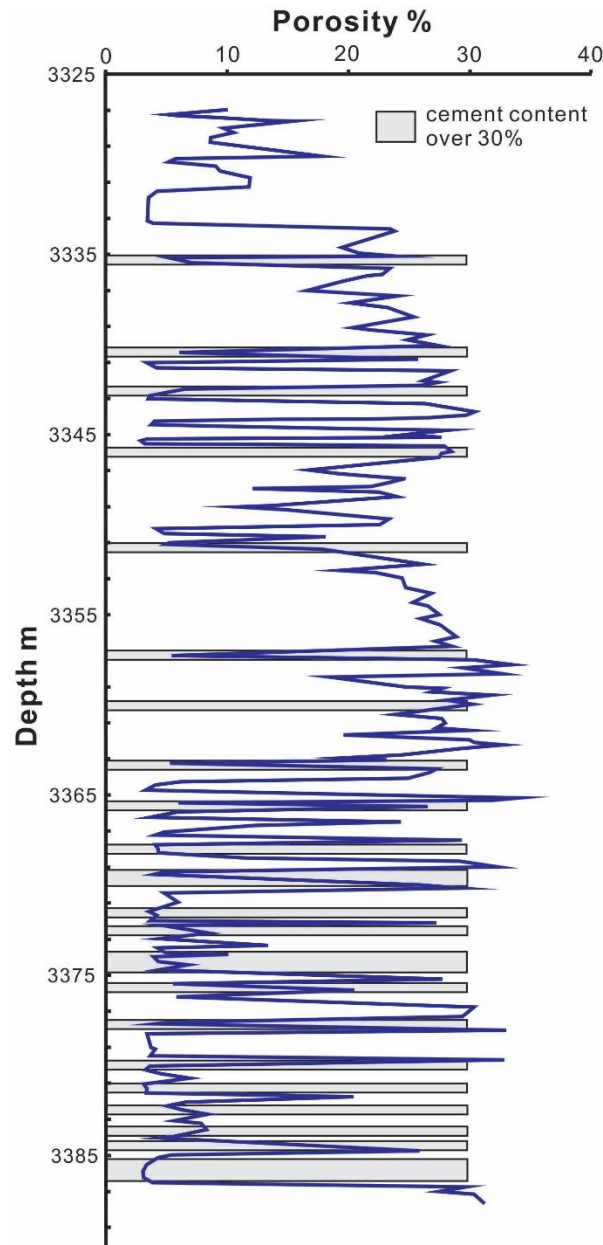


Figure 4.11: Diagram showing the relationship between porosity distribution in sandstones intervals and calcite-cemented zones. The gray bar represents intervals with calcite cements over 30%. The porosity data are acquired from Natural Resources Canada website (http://basin.gdr.nrcan.gc.ca/index_e.php).

CHAPTER V

CONCLUSIONS

The Upper Jurassic Ti-3 sandstones of the Flemish Pass Basin consist of sublitharenites with various diagenetic minerals, including calcite, pyrite, quartz overgrowth, dolomite and siderite. Petrographic analysis shows that the dominant cement is poikilotopic (300-500 μ m) calcite. Based on the volume of calcite cement, the investigated sandstones can be classified into (1) calcite-cemented intervals (>20% calcite), and (2) poorly calcite-cemented intervals (porous).

Petrographic examinations suggest that the poikilotopic calcite cements started forming at early diagenesis and kept precipitating with progressive burial, which is consistent with their stable isotope compositions analyses and fluid inclusion microthermometry, while the fracture-filling calcite developed at deep burial settings with higher T_h and salinity estimates.

The origin and geochemical compositions of calcites were controlled by the diagenetic environment and sediment compositions. The calculated estimates of the $\delta^{18}\text{O}$ composition of parent diagenetic fluids, the fluid-inclusion gas ratios and Ce anomaly values suggest that the calcite cements precipitated from modified seawater that was mixed with meteoric water in suboxic conditions.

The $\delta^{13}\text{C}$ ratios and high Sr contents reflect contributions from in-situ dissolution of bioclasts (possibly aragonitic shells) and positive Eu anomaly reflects some contributions from the dissolution of plagioclase during diagenetic burial. The similarity in the REE_{SN} patterns suggests that the cements developed from basinal fluids that their composition evolved through the circulation in the sediments.

Despite the early cementation of the Flemish Basin Ti-3 sandstones that blocked significant volume of the pore space, the acidic fluids generated by maturation of organic matter during burial resulted in significant dissolution of the calcite cements and the development of high secondary porosity of up to 28% in some horizons, particularly those associated with silty mudstones beds.

REFERENCES

- Abid, I. A., Hesse, R., Harper, J. D., 2004. Variations in mixed-layer illite/smectite diagenesis in the rift and post-rift sediments of the Jeanne d'Arc Basin, Grand Banks offshore Newfoundland, Canada. *Canadian Journal of Earth Sciences* 41, 401-429.
- Adams, A. E., MacKenzie, W. S., Guilford, C., 1984. Atlas of sedimentary rocks under the microscope. Wiley, New York.
- Alibo, D. S., Nozaki, Y., 1999. Rare earth elements in seawater: particle association, shale-normalization, and Ce oxidation. *Geochimica et Cosmochimica Acta* 63, 363-372.
- Al-Ramadan, K., Morad, S., Proust, J. N., Al-Aasm, I., 2005. Distribution of diagenetic alterations in siliciclastic shoreface deposits within a sequence stratigraphic framework: evidence from the Upper Jurassic, Boulonnais, NW France. *Journal of Sedimentary Research* 75, 943-959.
- Anderson, T. F., Arthur, M. A., 1983. Stable isotopes of oxygen and carbon and their application to sedimentologic and paleoenvironmental problems. In: Arthur, M. A., Anderson, T. F., Kaplan, I. R., Verzer, J., Land, L. S., (Eds.), *Stable Isotopes in Sedimentary Geochemistry: Society of Economic Palaeontologists and Mineralogists Short course 10*, pp. 1.1-1-151.
- Azmy, K., Blamey, N. J. F., 2013. Source of diagenetic fluids from fluid-inclusion gas ratios. *Chemical Geology* 347, 246-254.

- Azmy, K., Brand, U., Sylvester, P., Gleeson, S. A., Logan, A., Bitner, M. A., 2011. Biogenic and abiogenic low-Mg calcite (bLMC and aLMC): evaluation of seawater-REE composition, water masses and carbonate diagenesis. *Chemical Geology* 280, 180-190.
- Azmy, K., Knight, I., Lavoie, D., Chi, G., 2009. Origin of dolomites in the Boat Harbour Formation, St. George Group, in western Newfoundland, Canada: implications for porosity development. *Bulletin of Canadian Petroleum Geology* 57, 81-104.
- Azomani, E., Azmy, K., Blamey, N., Brand, U., Al-Aasm, I., 2013. Origin of Lower Ordovician dolomites in eastern Laurentia: Controls on porosity and implications from geochemistry. *Marine and Petroleum Geology* 40, 99-114.
- Baccar, M. B., Fritz, B., Made, B., 1993. Diagenetic albitization of K-feldspar and plagioclase in sandstone reservoirs; thermodynamic and kinetic modeling. *Journal of Sedimentary Research* 63, 1100-1109.
- Banner, J. L., 1995. Application of the trace element and isotope geochemistry of strontium to studies of carbonate diagenesis. *Sedimentology* 42, 805-824.
- Banner, J. L., Hanson, G. N., 1990. Calculation of simultaneous isotopic and trace element variations during water-rock interaction with applications to carbonate diagenesis. *Geochimica et Cosmochimica Acta* 54, 3123-3137.
- Barnaby, R. J., Rimstidt, J. D., 1989. Redox conditions of calcite cementation interpreted from Mn and Fe contents of authigenic calcites. *Geological Society of America Bulletin* 101, 795-804.

- Basu, A., Schieber, J., Patranabis-Deb, S., Dhang, P. C., 2013. Recycled Detrital Quartz Grains Are Sedimentary Rock Fragments Indicating Unconformities: Examples from the Chhattisgarh Supergroup, Bastar Craton, India. *Journal of Sedimentary Research* 83, 368-376.
- Bau, M., Balan, S., Schmidt, K., Koschinsky, A., 2010. Rare earth elements in mussel shells of the Mytilidae family as tracers for hidden and fossil high-temperature hydrothermal systems. *Earth and Planetary Science Letters* 299, 310-316.
- Bau, M., Dulski, P., 1996. Distribution of yttrium and rare-earth elements in the Penge and Kuruman iron-formations, Transvaal Supergroup, South Africa. *Precambrian Research* 79, 37-55.
- Bennett, P.C., Siegel, D.I., 1987. Increased solubility of quartz in water due to complexing by organic compounds. *Nature (Lond.)* 326, 684–686.
- Berner, R. A., 1981. Authigenic mineral formation resulting from organic matter decomposition in modern sediments. *Fortschritte der mineralogy* 59, 117-135.
- Bjørkum, P. A., Walderhaug, O., 1990. Geometrical arrangement of calcite cementation within shallow marine sandstones. *Earth-Science Reviews* 29, 145-161.
- Bjørlykke, K., 1983. Diagenetic reactions in sandstones. In: Parker, A., Sellwood, B. W., (Eds.), *Sediment diagenesis*. Springer Netherlands, pp. 169-213.
- Bjørlykke, K., Egeberg, P. K., 1993. Quartz cementation in sedimentary basins. *AAPG bulletin* 77, 1538-1548.

- Bjørlykke, K., Jahren, J., 2010. Sandstones and sandstone reservoirs. In: Bjørlykke, K. (Ed.), *Petroleum Geoscience: From Sedimentary Environments to Rock Physics*. Springer, Amsterdam, pp. 113-140
- Bjørlykke, K., Land, L. S., Dutton, S. P., Boles, J. R., Franks, S. G., 1979. Cementation of sandstones; discussion and replies. *Journal of Sedimentary Research* 49, 1358-1362.
- Bjørlykke, K., Ramm, M., Saigal, G. C., 1989. Sandstone diagenesis and porosity modification during basin evolution. *Geologische Rundschau* 78, 243-268.
- Blamey, N. J. F., 2012. Composition and evolution of crustal, geothermal and hydrothermal fluids interpreted using quantitative fluid inclusion gas analysis. *Journal of Geochemical Exploration* 116, 17-27.
- Blamey, N., Norman, D. I., 2002. New Interpretations of Geothermal Fluid Inclusion Volatiles: Ar/He and N₂/Ar ratios-A Better Indicator of Magmatic Volatiles, and Equilibrium Gas Geothermometry. In *Proceedings: Twenty-seventh Workshop on Geothermal Reservoir Engineering*, Stanford University, Stanford, California.
- Blamey, N. J. F., Azmy, K., Brand, U., 2014. Provenance and burial history of cement in sandstones of the Northbrook Formation (Carboniferous), western Newfoundland, Canada: A geochemical investigation. *Sedimentary Geology* 299, 30-41.
- Blatt, H., 1979. Diagenetic processes in sandstones. In: Scholle, P. A., Schluger, P. R., (Eds.), *Aspects of Diagenesis*. SEPM Special Publication 26, pp. 141-458.

- Bodnar, R. J., 2003. Interpretation of Data from Aqueous-Electrolyte Fluid Inclusion. In Samson, I., Anderson, A., Marshal, D. (Eds.), *Fluid Inclusions: Analysis and Interpretation*. Mineralogical Association of Canada Short Course 32, pp. 81-100.
- Boggs, S., 2009. *Petrology of sedimentary rocks*. Cambridge University Press, Cambridge, UK, 2009.
- Boggs, S., Krinsley, D., 2006. *Application of cathodoluminescence imaging to the study of sedimentary rocks*. Cambridge University Press, New York.
- Brehm, U., Gorbushina, A., Mottershead, D., 2005. The role of microorganisms and biofilms in the breakdown and dissolution of quartz and glass. *Palaeogeography, Palaeoclimatology, Palaeoecology* 219, 117-129.
- Brigaud, B., Durllet, C., Deconinck, J. F., Vincent, B., Thierry, J., Trouiller, A., 2009. The origin and timing of multiphase cementation in carbonates: impact of regional scale geodynamic events on the Middle Jurassic Limestones diagenesis (Paris Basin, France). *Sedimentary Geology* 222, 161-180.
- Brown, D. M., McAlpine, K. D., Yole, R. W., 1989. Sedimentology and sandstone diagenesis of Hibernia Formation in Hibernia oil field, Grand Banks of Newfoundland. *AAPG Bulletin* 73, 557-575.
- Burley, S. D., Kantorowicz, J. D., 1986. Thin section and SEM textural criteria for the recognition of cement-dissolution porosity in sandstones. *Sedimentology* 33, 587-604.

- Burley, S. D., Kantorowicz, J. D., Waugh, B., 1985. Clastic diagenesis. In: Brenchley, P. J., Williams, B. P. J., (Eds.), *Sedimentology: Recent Developments and Applied Aspects*. Geological Society of London, Special Publications 18, pp. 189-226.
- Burley, S. D., Mullis, J. T., Matter, A., 1989. Timing diagenesis in the Tartan Reservoir (UK North Sea): constraints from combined cathodoluminescence microscopy and fluid inclusion studies. *Marine and Petroleum Geology* 6, 98-120.
- Canada-Newfoundland and Labrador Offshore Petroleum Board (C-NLOPB), 2004 & 2014. Schedule of wells: Newfoundland and Labrador area. <http://www.cnlopb.ca/>
- Chowdhury A. H, Noble J. P. A., 1996. Origin, distribution and significance of carbonate cements in the Albert Formation reservoir sandstones, New Brunswick, Canada. *Marine and petroleum geology* 13, 837-846.
- Clark, I. D., Fritz, P., 1997. *Environmental isotopes in hydrogeology*. Lewis, New York.
- Clifton, H. E., 1982. Estuarine Deposits. In: Scholle, P. A., Spearing, D., (Eds.), *Sandstone Depositional Environments*. AAPG Memoir 31, pp. 179-189.
- Cobb, J. C., Cecil, C. B., 1993. Modern and ancient coal-forming environments. Geological Society of America, Special Paper 286, 1-198.
- Coleman, M. L., Raiswell, R., 1993. Microbial mineralization of organic matter: mechanisms of self-organization and inferred rates of precipitation of diagenetic minerals. *Philosophical Transactions of the Royal Society of London*, A344 , 69-87.

- Conliffe, J., Azmy, K., Gleeson, S. A., Lavoie, D., 2010. Fluids associated with hydrothermal dolomitization in St. George Group, western Newfoundland, Canada. *Geofluids*, 10, 422-437.
- Curtis, C. D., 1978. Possible links between sandstone diagenesis and depth-related geochemical reactions occurring in enclosing mudstones. *Journal of the Geological Society* 135, 107-117.
- de Baar, H. J. W., Bacon, M. P., Brewer, P. G., Bruland, K. W., 1985. Rare earth elements in the Pacific and Atlantic Oceans. *Geochimica et Cosmochimica Acta* 49, 1943-1959.
- Denniston, R. F., Shearer, C. K., Layne, G. D., Vaniman, D. T., 1997. SIMS analyses of minor and trace element distributions in fracture calcite from Yucca Mountain, Nevada, USA. *Geochimica et cosmochimica acta* 61, 1803-1818.
- DeSilva, N. R., 1999. Sedimentary basins and petroleum systems offshore Newfoundland and Labrador. In: Fleet, A.J., Boldy, S.A.R., (Eds.), *Petroleum geology of northwest Europe: Proceedings of the fifth conference*. The Geological Society, London, pp. 501–515
- DeSilva, N. R., 2000. Flemish Pass Basin: Hydrocarbon Prospectivity and Potential Deep Water Development. *Terra Nova* 64, 2-2.
- Dickson, T., 1990. Carbonate mineralogy and chemistry. In: Tucker, M.E., Wright, V.P. (Eds.), *Carbonate Sedimentology*. Blackwell Scientific Publications, Oxford, pp. 284–313.
- Dutton, S. P., 2008. Calcite cement in Permian deep-water sandstones, Delaware Basin, west Texas: Origin, distribution, and effect on reservoir properties. *AAPG bulletin* 92, 765-787.

- Dutton, S. P., Flanders, W. A., Barton, M. D., 2003. Reservoir characterization of a Permian deep-water sandstone, East Ford field, Delaware basin, Texas. AAPG bulletin 87, 609-627.
- Dutton, S. P., Loucks, R. G., Day-Stirrat, R. J., 2012. Impact of regional variation in detrital mineral composition on reservoir quality in deep to ultradeep lower Miocene sandstones, western Gulf of Mexico. *Marine and Petroleum Geology* 35, 139-153.
- Dutton, S. P., Willis, B. J., White, C. D., Bhattacharya, J. P., 2000. Outcrop characterization of reservoir quality and interwell-scale cement distribution in a tide-influenced delta, Frontier Formation, Wyoming, USA. *Clay Minerals* 35, 95-105.
- Elderfield, H., Greaves, M. J., 1982. The rare earth elements in seawater. *Nature* 296, 214-218.
- Elderfield, H., Sholkovitz, E. T., 1987. Rare earth elements in the pore waters of reducing nearshore sediments. *Earth and Planetary Science Letters* 82, 280-288.
- Emery, K. O., Rittenberg, S. C., 1952. Early diagenesis of California basin sediments in relation to origin of oil. *AAPG Bulletin* 36, 735-806.
- Enachescu, M. E., 1987. Tectonic and structural framework of the northeast Newfoundland continental margin. In: Beaumont, C., Tankard, A. J., (Eds.), *Sedimentary basins and basin forming mechanisms*. Canadian Society of Petroleum Geologists, memoirs 12, pp. 117-146.
- Enachescu, M. E., 1988. Extended basement beneath the intracratonic rifted basins of the Grand Banks of Newfoundland. *Canadian Journal of Exploration Geophysics* 24, 48-65.

- Enachescu, M., 2014. Petroleum Exploration Opportunities in the Flemish Pass Basin, Newfoundland and Labrador Offshore Area: Call for Bids NL13-01, Area “C”–Flemish Basin, Parcel. <http://www.nr.gov.nl.ca/nr/invest/nl1301flemishpassbasinenachescu.pdf>
- Enachescu, M. E., Hogg, J. R., 2005. Exploring for Atlantic Canada’s next giant petroleum discovery. CSEG Recorder 30, 19-30.
- Enachescu, M. E., Kearsy, S., Hardy, V., Sibuet, J., Hogg, J., Srivastava, S., Fagan, A., Thompson, T., Ferguson, R., 2005. Evolution and petroleum potential of Orphan Basin, offshore Newfoundland, and its relation to the movement and rotation of Flemish Cap based on plate kinematics of the North Atlantic. In: Post, P. J. R., Norman, C., Olson, S. L., Plames, S. L., Lyons, K.T., Newton, G. B., (Eds.), 25th annual Gulf Coast section SEPM Foundation, Bob F. Perkins research conference, symposium on petroleum systems of divergent continental margin basins, Society for Sedimentary Geology, Gulf Coast Section 25, Dallas, Texas, pp. 7-8.
- Epstein, S. A., Friedman, G. M., 1982. Processes controlling precipitation of carbonate cement and dissolution of silica in reef and near-reef settings. *Sedimentary Geology* 33, 157-171.
- Faure, G., Mensing, T. M., 2005. *Isotopes: principles and applications*. John Wiley & Sons Inc., Hoboken, New Jersey.
- Flügel, E., 2004. *Microfacies of Carbonate Rocks*. Springer, Berlin.
- Folk, R. L., 1980. *Petrology of sedimentary rocks*. Hemphill Publishing Co., Austin, Texas.
- Foster, D. G., Robinson, A. G., 1993. Geological history of the Flemish Pass Basin, offshore Newfoundland. *AAPG Bulletin* 77, 588-609.

- Frank, J. R., Carpenter, A. B., Oglesby, T. W., 1982. Cathodoluminescence and composition of calcite cement in the Taum Sauk Limestone (Upper Cambrian), Southeast Missouri. *Journal of Sedimentary Research* 52, 631-638.
- Friedman, G. M., Ali, S. A., Krinsley, D. H., 1976. Dissolution of quartz accompanying carbonate precipitation and cementation in reefs; example from the Red Sea. *Journal of Sedimentary Research* 46, 970-973.
- Friedman, I., O'Neil, J. R., 1977. Compilation of stable isotope fractionation factors of geochemical interest. In: Fleischer, M., (Ed.), *Data of Geochemistry*. USGPO, Washington, D.C, pp. 1-12
- Gautier, D. L., Claypool, G. E., 1984. Interpretation of methanic diagenesis in ancient sediments by analogy with processes in modern diagenetic environments. In: McDonald, D. A., Surdam, R. C., (Eds.), *Clastic Diagenesis*. AAPG Memoir 37, pp. 111-123.
- German C. R., Elderfield H., 1990. Application of the Ce anomaly as a paleoredox indicator: the ground rules. *Paleoceanography*, 5, 823-833.
- German, C. R., Holliday, B. P., Elderfield, H., 1991. Redox cycling of rare earth elements in the suboxic zone of the Black Sea. *Geochimica et Cosmochimica Acta* 55, 3553-3558.
- Giggenbach, W. F., 1986. The use of gas chemistry in delineating the origin of fluids discharges over the Taupo Volcanic Zone. *International Volcanological Congress*, Hamilton, New Zealand, pp. 47-50.

- Giroir, G., Merino, E., Nahon, D., 1989. Diagenesis of Cretaceous sandstone reservoirs of the South Gabon rift basin, West Africa; mineralogy, mass transfer, and thermal evolution. *Journal of Sedimentary Research* 59, 482-493.
- Gladney, E. S., O'Malley, B.T., Roelandts, I., Gills, T.E., 1987. Compilation of elemental concentration data for NBS clinical, biological, geological, and environmental standard reference materials. NBS Special Report 260-111.
- Goldstein S. J., Jacobsen S. B., 1988. Rare earth elements in river waters. *Earth Planet Science Letters* 89, 35–47.
- Goldstein, R. H., 2003. Petrographic analysis of fluid inclusions. In: Samson, I., Anderson, A., Marshall, D., (Eds.), *Fluid Inclusions: Analysis and Interpretation*. Mineral Assco. Can., Short Course 32, pp. 9-54.
- Goldstein, R.H., Reynolds, T.J., 1994. Systematics of Fluid Inclusions in Diagenetic Minerals. *Society for Sedimentary Geology Short Course Notes* 31, 199 pp.
- González-Acebrón, L., Arribas, J., Mas, R., 2010. Role of sandstone provenance in the diagenetic albitization of feldspars: A case study of the Jurassic Tera Group sandstones (Camerus Basin, NE Spain). *Sedimentary Geology* 229, 53-63.
- Gorbushina, A. A., Palinska, K. A., 1999. Biodeteriorative processes on glass: experimental proof of the role of fungi and cyanobacteria. *Aerobiologia*, 15, 183-192.
- Gruschwitz, K., Haynes, S. R., McDonough, M., Johnson, T., Stacey, E., 2013. Mizzen – the first oil discovery in the Flemish Pass Basin, offshore Newfoundland. In *Abstracts of Integration: CSEG, CSPG and CWLS GeoConvention 2013*, Calgary, Canada.

- Hayes M. J, Boles J. R., 1993. Evidence for meteoric recharge in the San Joaquin basin, California provided by isotope and trace element chemistry of calcite. *Marine and petroleum geology* 10, 135-144.
- Haynes, S. R, Gruschwitz, K., Johnson, T., McDonough, M., Stacey, E., 2012. Mizzen - An Overview of the First Oil Discovery in the Flemish Pass Basin, East Coast Offshore Newfoundland, Atlantic Continental Margin. Third Conjugate Margins Conference 2012, Central and North Atlantic, Trinity College, Dublin, Ireland, Abstract Volume, p. 51.
- Haynes, S. R., Marshall, J., Imsland-Wathne, E., Minielly, G., Mortlock, E. Walderhaug, O, and Johnson, T. 2013. Depositional Interpretation and Reservoir Characterization of the Tithonian in Mizzen F-09, Flemish Pass Basin, Canada. In *Abstracts of Integration: CSEG, CSPG and CWLS GeoConvention 2013*, Calgary, Canada.
- Hesse, R., 1990. Pore-water anomalies in gas hydrate-bearing sediments of the deeper continental margins: facts and problems. *Journal of Inclusion phenomena and molecular recognition in chemistry* 8, 117-138.
- Hesse, R., Abid, L. A., 1998. Carbonate cementation-the key to reservoir properties of four sandstone levels (Cretaceous) in the Hibernia Oilfield, Jeanne d'Arc Basin, Newfoundland, Canada. In: Morad, S., (Ed.), *Carbonate Cementation in Sandstones: Distribution Patterns and Geochemical Evolution*. International Association of Sedimentologists Special Publication 26, pp. 363-393.
- Heydari, E., Moore, C. H., 1993. Zonation and geochemical patterns of burial calcite cements; upper Smackover Formation, Clarke County, Mississippi. *Journal of Sedimentary Research* 63, 44-60.

- Hogg, J. R., Enachescu, M. E., 2007. Exploration potential of the deep-water petroleum systems of Newfoundland and Labrador Margins. Offshore Technology Conference, Houston Texas.
- Holmden, C., Hudson, J. D., 2003. $^{87}\text{Sr}/^{86}\text{Sr}$ and Sr/Ca Investigation of Jurassic mollusks from Scotland: Implications for paleosalinities and the Sr/Ca ratio of seawater. Geological Society of America Bulletin, 115, 1249-1264.
- Holser, W. T., 1997. Evaluation of the application of rare-earth elements to paleoceanography. *Palaeogeography, Palaeoclimatology, Palaeoecology* 132, 309-323.
- Hongo, Y., Nozaki, Y., 2001. Rare earth element geochemistry of hydrothermal deposits and Calyptogena shell from the Iheya Ridge vent field, Okinawa Trough. *Geochemical Journal* 35, 347-354.
- Huppertz, T. J., Piper, D. J., 2009. The influence of shelf-crossing glaciation on continental slope sedimentation, Flemish Pass, eastern Canadian continental margin. *Marine Geology* 265, 67-85.
- Hutcheon, I., Nahnybida, C., Krouse, H. R., 1985. The Geochemistry of Carbonate Cements in the Avalon Sand, Grand Banks of Newfoundland. *Mineralogical Magazine* 49, 457-467.
- Irwin, H., Coleman, M., Curtis, C. D, 1977. Isotopic evidence for source of diagenetic carbonates formed during burial of organic-rich sediments. *Nature* 269, 209-213.
- Jones, H. D., Kesler, S. E., 1992. Fluid inclusion gas chemistry in east Tennessee Mississippi Valley-type districts: evidence for immiscibility and implications for depositional mechanisms. *Geochimica et Cosmochimica Acta* 56, 137-154.

- Kennard, L., Schafer, C., Carter, L., 1990. Late Cenozoic evolution of Sackville Spur: a sediment drift on the Newfoundland continental slope. *Canadian Journal of Earth Sciences* 27, 863-878.
- Kinsman, D. J., 1969. Interpretation of Sr^{+2} concentrations in carbonate minerals and rocks. *Journal of Sedimentary Research* 39, 486-508.
- Klinkhammer, G. P., Elderfield, H., Edmond, J. M., Mitra, A., 1994. Geochemical implications of rare earth element patterns in hydrothermal fluids from mid-ocean ridges. *Geochimica et Cosmochimica Acta* 58, 5105-5113.
- Krumbein, W. C., Pettijohn, F. J., 1938. *Manual of sedimentary petrography*. D. Appleton-Century, New York.
- Land, L. S., 1980. The isotopic and trace element geochemistry of dolomite: the state of the art. In: Zenger, D. H., et al., (Eds.), *Concepts and Models of Dolomitisation*. SEPM Special Publication 28, 87-110
- Land, L. S., 1984. Frio sandstone diagenesis, Texas Gulf Coast: a regional isotopic study. In: McDonald, D.A., Surdan, R.C., (Eds.), *Clastic Diagenesis*, AAPG Memoirs 37, pp. 47-62.
- Land, L.S., 1995. Oxygen and carbon isotopic composition of Ordovician brachiopods: implications for coeval seawater: discussion. *Geochimica et Cosmochimica Acta* 59, 2843–2844.
- Landis, G. P., Hofstra, A. H., 1991. Fluid inclusion gas chemistry as a potential minerals exploration tool: Case studies from Creede, CO, Jerritt Canyon, NV, Coeur d'Alene

- district, ID and MT, southern Alaska mesothermal veins, and mid-continent MVT's. *Journal of Geochemical Exploration* 42, 25-59.
- Lawler, J. P., Crawford, M. L., 1983. Stretching of fluid inclusions resulting from a low-temperature microthermometric technique. *Economic Geology*, 78, 527-529.
- Lee, S. G., Lee, D. H., Kim, Y., Chae, B. G., Kim, W. Y., Woo, N. C., 2003. Rare earth elements as indicators of groundwater environment changes in a fractured rock system: evidence from fracture-filling calcite. *Applied Geochemistry* 18, 135-143.
- Lindholm, R. C., Finkelman, R. B., 1972. Calcite Staining: Semiquantitative Determination of Ferrous Iron: NOTES. *Journal of Sedimentary Research* 42.
- Liu, S., Huang, S., Shen, Z., Lü, Z., Song, R., 2014. Diagenetic fluid evolution and water-rock interaction model of carbonate cements in sandstone: An example from the reservoir sandstone of the Fourth Member of the Xujiahe Formation of the Xiaoquan-Fenggu area, Sichuan Province, China. *Science China Earth Sciences* 57, 1077-1092.
- Longinelli, A., Iacumin, P., Ramigni, M., 2002. $\delta^{18}\text{O}$ of carbonate, quartz and phosphate from belemnite guards: implications for the isotopic record of old fossils and the isotopic composition of ancient seawater. *Earth and Planetary Science Letters* 203, 445-459.
- Longstaffe, F. J., 1983. Diagenesis, 4. Stable isotope studies of diagenesis in clastic rocks. *Geoscience Canada* 10, 44-58.
- Longstaffe, F. J., 1987. Stable isotope studies of diagenetic processes. In: Kyser, K., (Eds.), *Short course in stable isotope geochemistry of low temperature fluids*. Mineralogical Association of Canada Saskatoon, Vol. 13, pp. 187-257.

- Longstaffe, F. J., Calvo, R., Ayalon, A., Donaldson, S., 2003. Stable isotope evidence for multiple fluid regimes during carbonate cementation of the Upper Tertiary Hazeva Formation, Dead Sea Graben, southern Israel. *Journal of Geochemical Exploration* 80, 151-170.
- Loucks, R. G., Bebout, D. G., Galloway, W. E., 1977. Relationship of Porosity Formation and Preservation to Sandstone Consolidation History--Gulf Coast Lower Tertiary Frio Formation (1). *Gulf Coast Association of Geological Societies Transactions* 27, 109-120.
- Love, L. G., 1967. Early diagenetic iron sulphide in recent sediments of the Wash (England). *Sedimentology* 9, 327-352.
- Lowe, D. G., 2009. Provenance and paleodrainage of Late Jurassic and Early Cretaceous reservoir sandstones in the Flemish Pass and Orphan Basins. Unpublished Master's thesis, Memorial University of Newfoundland, St. John's, Canada, 323 pp.
- Lowe, D. G., Sylvester, P. J., Enachescu, M. E., 2011. Provenance and paleodrainage patterns of Upper Jurassic and Lower Cretaceous synrift sandstones in the Flemish Pass Basin, offshore Newfoundland, east coast of Canada. *AAPG bulletin* 95, 1295-1320.
- Machel, H. G., 2000. Application of cathodoluminescence to carbonate diagenesis. In: Pagle, M., Barbin, V., Balnc, P., Ohnenstetter, D., (Eds.), *Cathodoluminescence in geosciences*. Springer, Berlin Heidelberg, pp. 271-301.
- Machel, H. G., Burton, E. A., 1991. Factors governing cathodoluminescence in calcite and dolomite, and their implications for studies of carbonate diagenesis. In: Barker, C, E., Kopp, O, C., (Eds.), *Luminescence microscopy and spectroscopy: qualitative and quantitative applications*. SEPM Short Course 25, pp. 9-25.

- Machel, H. G., Mason, R. A., Mariano, A.N., Mucci, A., 1991. Causes and emission of luminescence in calcite and dolomite. In: Barker, C.E., Kopp, O.C. (Eds.), *Luminescence microscopy: quantitative and qualitative aspects*. Society of Economic Paleontologists and Mineralogists, Short Course notes 25, pp. 9–25.
- Machemer, S. D., Hutcheon, I. D., 1988. Geochemistry of early carbonate cements in the Cardium Formation, central Alberta. *Journal of Sedimentary Research* 58, 136-147.
- Mack, G. H., Cole, D. R., Giordano, T. H., Schaal, W. C., Barcelos, J. H., 1991. Paleoclimatic controls on stable oxygen and carbon isotopes in caliche of the Abo Formation (Permian), south-central New Mexico, USA. *Journal of Sedimentary Research* 61, 458-472.
- Magoon, L. B., Hudson, T. L., Peters, K. E., 2005. Egret-Hibernia (!), a significant petroleum system, northern Grand Banks area, offshore eastern Canada. *AAPG bulletin* 89, 1203-1237.
- Mao, J., Li, Y., Goldfarb, R., He, Y., Zaw, K., 2003. Fluid inclusion and noble gas studies of the Dongping gold deposit, Hebei Province, China: a mantle connection for mineralization?. *Economic Geology*, 98, 517-534.
- McAlpine, K. D., 1990. Mesozoic Stratigraphy, Sedimentary Evolution, and Petroleum Potential of the Jeanne d'Arc Basin, Grand Banks of Newfoundland. Geological Survey of Canada, special paper 89, 50 pp.
- McBride, E. F., 1987. Diagenesis of the Maxon Sandstone (Early Cretaceous), Marathon region, Texas; a diagenetic quartzarenite. *Journal of Sedimentary Research* 57, 98-107.
- McBride, E. F., 1989. Quartz cement in sandstones: a review. *Earth-Science Reviews* 26, 69-112.

- McBride, E. F., Milliken, K. L., Cavazza, W., Cibin, U., Fontana, D., Picard, M. D., Zuffa, G. G., 1995. Heterogeneous distribution of calcite cement at the outcrop scale in Tertiary sandstones, northern Apennines, Italy. *AAPG bulletin* 79, 1044-1062.
- McCracken, J. N., Barnwell, A. C., Haager, A., Kubica, P., Saunders, K. I., Zwach, C., 2001. Exploring the Outer Limits of the Upper Jurassic Source Rocks on the Grand Banks of Newfoundland, Canada. AAPG Annual Meeting.
- McCracken, J. N., Haager, A., Saunders, K. I., Veilleux, B. W., 2000. Late Jurassic source rocks in the northern Flemish Pass basin. In *Grand Banks of Newfoundland: Canadian Society of Exploration Geophysicists Conference*, Abstract.
- McDonough, M. R., Sylvester, P., Bruder, N., Lo, J., O'Sullivan, P., 2011. Provenance of reservoir sandstones in the Flemish Pass and Orphan Basins (Canada): U-Pb dating of detrital zircons using the laser ablation method. *CM 2010-Abstracts*, 5.
- McLemore, V., Barker, J. M., 1987. Some geological applications of cathodoluminescence. *New Mexico Geology*, 37-40
- McLennan, S. M., 1989. Rare earth elements in sedimentary rocks: influence of provenance and sedimentary processes. In: Lipin, B. R., McKay, G. A (Eds.), *Geochemistry and Mineralogy of Rare Earth Elements: Reviews in Mineralogy*. Mineralogical Society of America, pp. 169-200.
- Meyers, W. J., 1989. Trace element and isotope geochemistry of zoned calcite cements, Lake Valley Formation (Mississippian, New Mexico): insights from water-rock interaction modelling. *Sedimentary geology* 65, 355-370.

- Moore, J. N., Norman, D. I., Kennedy, B. M., 2001. Fluid inclusion gas compositions from an active magmatic–hydrothermal system: a case study of The Geysers geothermal field, USA. *Chemical Geology* 173, 3-30.
- Morad, S., 1998. Carbonate Cementation in Sandstones: Distribution Patterns and Geochemical Evolution. In: Morad, S., (Ed.), *Cementation in Sandstones: Distribution Patterns and Geochemical Evolution*. International Association of Sedimentologists Special Publication 26, pp. 1-26.
- Morad, S., Al-Ramadan, K., Ketzer, J. M., De Ros, L. F., 2010. The impact of diagenesis on the heterogeneity of sandstone reservoirs: A review of the role of depositional facies and sequence stratigraphy. *AAPG bulletin*, 94, 1267-1309.
- Morad, S., Bergan, M., Knarud, R., Nystuen, J. P., 1990. Albitization of detrital plagioclase in Triassic reservoir sandstones from the Snorre Field, Norwegian North Sea. *Journal of Sedimentary Research* 60, 411-425.
- Mozley, P. S., Burns, S. J., 1993. Oxygen and carbon isotopic composition of marine carbonate concretions; an overview. *Journal of Sedimentary Research* 63, 73-83.
- Natural Resourced Canada, 2014. Well-BASIN Database:
http://basin.gdr.nrcan.gc.ca/wells/well_query_e.php.
- Norman, D. I., Blamey, N. J. F., 2001. Quantitative analysis of fluid inclusion volatiles by a two mass spectrometer system. In: Noronha, F., Doria, A., Guedes, A., (Eds.), *European Current Research on Fluid Inclusions, Porto 2001 (XVI ECROFI)*: Faculdade de Ciencias do Porto, Departamento de Geologia, Memoria 7, pp. 341-344.

- Norman, D. I., Blamey, N., 2005. Methane in Carlin-type gold deposit fluid inclusions. *Geochimica et Cosmochimica Acta Supplement* 69, A124.
- Norman, D. I., Moore, J. N., 1997. Gaseous species in fluid inclusions: a fluid tracer and indicator of fluid processes. *European Current Research on Fluid Inclusions*, No. XIV, Nancy, France, Abstracts, pp. 243 –244.
- Norman, D. I., Moore, J. N., 1999. Methane and Excess N₂ and Ar in Geothermal Fluid Inclusions. In: *Proceedings: Twenty-fourth Workshop of Geothermal Reservoir Engineering*. Stanford University, Stanford, California, pp. 233-240.
- Norman, D. I., Musgrave, J. A., 1994. N₂-Ar-He compositions in fluid inclusions: Indicators of fluid source. *Geochimica et Cosmochimica Acta* 58, 1119-1131.
- Norman, D. I., Blamey, N., Moore, J. N., 2002. Interpreting geothermal processes and fluid sources from fluid inclusion organic compounds and CO₂/N₂ ratios. *Proceedings: Twenty-seventh Workshop on Geothermal Reservoir Engineering* Stanford University, Stanford, California.
- Norman, D.I., Moore, J.N., Yonaka, B., Musgrave, J., 1996, Gaseous species in fluid inclusions: A tracer of fluids and an indicator of fluid processes. *Proceedings: Twenty-first Workshop of Geothermal Reservoir Engineering*, Stanford University, Stanford, California, January 22-24, p. 233-240.
- Normore, L. S., 2006. Origin, distribution and paragenetic sequence of carbonate cements in the Ben Nevis Formation, White Rose Field, Jeanne d'Arc Basin, offshore Newfoundland, Canada. Unpublished Master's thesis, Memorial University of Newfoundland, St. John's, Canada, 214pp.

- Nothdurft, L. D., Webb, G. E., Kamber, B. S., 2004. Rare earth element geochemistry of Late Devonian reefal carbonates, Canning Basin, Western Australia: confirmation of a seawater REE proxy in ancient limestones. *Geochimica et Cosmochimica Acta* 68, 263-283.
- Nyman, S. L., Gani, M. R., Bhattacharya, J. P., Lee, K., 2014. Origin and distribution of calcite concretions in Cretaceous Wall Creek Member, Wyoming: Reservoir-quality implication for shallow-marine deltaic strata. *Cretaceous Research*, 48, 139-152.
- Olanipekun, B. J., Azmy, K., Brand, U., 2014. Dolomites of the Boat Harbour Formation in the Northern Peninsula, western Newfoundland, Canada: Implications for dolomitization history and porosity control. *AAPG bulletin* 98, 765-791.
- Parnell, J., Middleton, D., Honghan, C., Hall, D., 2001. The use of integrated fluid inclusion studies in constraining oil charge history and reservoir compartmentation: examples from the Jeanne d'Arc Basin, offshore Newfoundland. *Marine and Petroleum Geology* 18, 535-549.
- Pemberton, S. G., Spila, M., Pulham, A. J., Saunders, T., MacEachern, J. A., Robbins, D., & Sinclair, I. K., 2003. Ichnology and sedimentology of shallow marine to marginal marine systems: Ben Nevis & Avalon reservoirs, Jeanne d'Arc Basin. *Bulletin of Canadian Petroleum Geology* 51, 206-211.
- Percival, C.J., 1983, The Firestone Sill ganister, Namurian, Northern England—the A2 horizon of a podzol or podzolic palaeosol. *Sedimentary Geology* 36, 41–49.
- Pettijohn, F. J., Potter, P. E., Siever, R., 1987. *Sand and sandstone*. Springer-Verlag, New York.

- Piper, D. Z., 1974. Rare earth elements in the sedimentary cycle: a summary. *Chemical Geology* 14, 285-304.
- Pye, K., Dickson, J. A. D., Schiavon, N., Coleman, M. L., Cox, M., 1990. Formation of siderite-Mg-calcite-iron sulphide concretions in intertidal marsh and sandflat sediments, north Norfolk, England. *Sedimentology* 37, 325-343.
- Raiswell, R., 1987. Non-steady state microbiological diagenesis and the origin of concretions and nodular limestones. In: Marshall, J. D., (Ed.), *Diagenesis of Sedimentary Sequences*, Geological Society Special Publication 36, pp, 41-54.
- Roedder, E., 1984. *Fluid inclusions: an introduction to studies of all types of fluid inclusions, gas, liquid, or melt, trapped in materials from earth and space, and their application to the understanding of geologic processes*. Mineralogical Society of America, Vol. 12, 644pp.
- Saigal, G. C., Bjørlykke, K., 1987. Carbonate cements in clastic reservoir rocks from offshore Norway—relationships between isotopic composition, textural development and burial depth. In: Marshall, J.D., (Ed.), *Diagenesis of Sedimentary Sequences*. Geological Society Special Publications 36, pp. 313-324.
- Saigal, G. C., Morad, S., Bjorlykke, K., Egeberg, P. K., Aagaard, P., 1988. Diagenetic albitization of detrital K-feldspar in Jurassic, Lower Cretaceous, and Tertiary clastic reservoir rocks from offshore Norway; I, Textures and origin. *Journal of Sedimentary Research* 58, 1003-1013.
- Scotchman, I. C., 1991. The geochemistry of concretions from the Kimmeridge Clay Formation of southern and eastern England. *Sedimentology* 38, 79-106.

- Selley, R. C., 1996. Ancient sedimentary environments and their sub-surface diagnosis, 4th ed. Chapman & Hall, London.
- Seyedolali, A., Krinsley, D. H., Boggs, S., O'Hara, P. F., Dypvik, H., Goles, G. G., 1997. Provenance interpretation of quartz by scanning electron microscope–cathodoluminescence fabric analysis. *Geology* 25, 787-790.
- Shackleton, N.J., Kennett, J.P., 1975. Late Cenozoic oxygen and carbon isotopic change at DSDP site 284: implications for the glacial history of the Northern Hemisphere. In: Kennett, J.P., et al. (Eds.), *Initial Reports of the Deep Sea Drilling Project* 29, pp. 801-807.
- Shepherd, T. J., Waters, P., 1984. Fluid inclusion gas studies, Carrock Fell tungsten deposit, England: Implications for regional exploration. *Mineralium Deposita* 19, 304-314.
- Shepherd, T. J., Rankin, A. H., Alderton, D. H. M., 1985. *A Practical Guide to Fluid Inclusions*. Blackie, London, UK.
- Sholkovitz, E. R., Schneider, D. L., 1991. Cerium redox cycles and rare earth elements in the Sargasso Sea. *Geochimica et Cosmochimica Acta* 55, 2737-2743.
- Sholkovitz, E. R., Landing, W. M., Lewis, B. L., 1994. Ocean particle chemistry: the fractionation of rare earth elements between suspended particles and seawater. *Geochimica et Cosmochimica Acta* 58, 1567-1579.
- Sinclair I K., 1988. Evolution of Mesozoic-Cenozoic sedimentary basins in the Grand Banks area of Newfoundland and comparison with Falvey's (1974) rift model. *Bulletin of Canadian Petroleum Geology*, 36, 255-273.

- Sinclair, I. K., 1993. Tectonism: the dominant factor in mid-Cretaceous deposition in the Jeanne d'Arc Basin, Grand Banks. *Marine and petroleum geology* 10, 530-549.
- Sinclair, I. K., 1995. Sequence stratigraphic response to Aptian-Albian rifting in conjugate margin basins: a comparison of the Jeanne d'Arc Basin, offshore Newfoundland, and the Porcupine Basin, offshore Ireland. *Geological Society Special Publications* 90, pp. 29-49.
- Sippel, R. F., 1968. Sandstone petrology, evidence from luminescence petrography. *Journal of Sedimentary Research* 38, 530-554.
- Spötl, C., Wright, V. P., 1992. Groundwater dolocretes from the Upper Triassic of the Paris Basin, France: a case study of an arid, continental diagenetic facies. *Sedimentology* 39, 1119-1136.
- Sprunt, E. S., Nur, A., 1979. Microcracking and healing in granites: new evidence from cathodoluminescence. *Science* 205, 495-497.
- Statoil Canada Resources, 2011. Mizzen F-09 - End of Well Report. C-NLOPB file record number INV-119385. Available at the C-NLOPB library, TD Place, 140 Water Street, St. John's, Newfoundland, Canada, 195 pp.
- Sverjensky, D. A., 1984. Europium redox equilibria in aqueous solution. *Earth and Planetary Science Letters* 67, 70-78.
- Talma, A. S., Netterberg, F., 1983. Stable isotope abundances in calcretes. *Geological Society, London, Special Publications* 11, 221-233.

- Tankard, A. J., Welsink, H. J., 1989. Mesozoic extension and styles of basin formation in Atlantic Canada. Extensional tectonics and stratigraphy of the North Atlantic margins. AAPG Memoir 46, pp. 175-195.
- Taylor, K. G., Gawthorpe, R. L., Curtis, C. D., Marshall, J. D., Awwiller, D. N., 2000. Carbonate cementation in a sequence-stratigraphic framework: Upper Cretaceous sandstones, Book Cliffs, Utah-Colorado. *Journal of Sedimentary Research* 70, 360-372.
- Taylor, T. R., 1990. The influence of calcite dissolution on reservoir porosity in Miocene sandstones, Picaroon Field, offshore Texas Gulf Coast. *Journal of Sedimentary Research* 60, 322-334.
- Taylor, T. R., Giles, M. R., Hathon, L. A., Diggs, T. N., Braunsdorf, N. R., Birbiglia, G. V., et al., 2010. Sandstone diagenesis and reservoir quality prediction: Models, myths, and reality. *AAPG bulletin* 94, 1093-1132.
- Thomas, C., Graham, C., Ellam, R., Fallick, A., 2004. $^{87}\text{Sr}/^{86}\text{Sr}$ chemostratigraphy of Neoproterozoic Dalradian limestones of Scotland and Ireland: constraints on depositional ages and time scales. *Journal of the Geological Society* 161, 229-242.
- Trouw, R. A., Passchier, C. W., Wiersma, D. J., 2009. Crystal-Plastic Deformation, Recovery and Recrystallisation of Quartz. In *Atlas of Mylonites-and related microstructures*. Springer, Berlin, pp. 241-262
- Tucker, M. E., 2009. *Sedimentary petrology: an introduction to the origin of sedimentary rock*, 3rd ed. Blackwell Science, Malden.

- Van der Pluijm, B. A., Kaars-Sijpesteijn, C. H., 1984. Chlorite-mica aggregates: morphology, orientation, development and bearing on cleavage formation in very-low-grade rocks. *Journal of structural geology* 6, 399-407.
- Van Keer, I., Muchez, P., Viaene, W., 1998, Clay mineralogical variations and evolutions in sandstone sequences near a coal seam and shales in the Westphalian of the Campine Basin (NE Belgium). *Clay Minerals* 33, 159–169.
- Veizer, J., Ala, D., Azmy, K., Bruckschen, P., Buhl, D., Bruhn, F., et al., 1999. $^{87}\text{Sr}/^{86}\text{Sr}$, $\delta^{13}\text{C}$ and $\delta^{18}\text{O}$ evolution of Phanerozoic seawater. *Chemical geology* 161, 59-88.
- Veizer, J., Bruckschen, P., Pawellek, F., Diener, A., Podlaha, O. G., Carden, G. A., et al., 1997. Oxygen isotope evolution of Phanerozoic seawater. *Palaeogeography, Palaeoclimatology, Palaeoecology*, 132, 159-172.
- Wadleigh, M. A., Veizer, J., 1992. $^{18}\text{O}/^{16}\text{O}$ and $^{13}\text{C}/^{12}\text{C}$ in lower Paleozoic articulate brachiopods: Implications for the isotopic composition of seawater. *Geochimica et Cosmochimica Acta* 56, 431-443.
- Walderhaug, O., 1990. A fluid inclusion study of quartz-cemented sandstones from offshore mid-Norway; possible evidence for continued quartz cementation during oil emplacement. *Journal of Sedimentary Research* 60, 203-210.
- Walker, T. R., 1960. Carbonate replacement of detrital crystalline silicate minerals as a source of authigenic silica in sedimentary rocks. *Geological Society of America Bulletin* 71, 145-152.

- Wanas, H. A., 2008. Calcite-cemented concretions in shallow marine and fluvial sandstones of the Birket Qarun Formation (Late Eocene), El-Faiyum depression, Egypt: field, petrographic and geochemical studies: implications for formation conditions. *Sedimentary Geology* 212, 40-48.
- Wilkinson, M., 1991. The concretions of the Berreraig Sandstone Formation: geometry and geochemistry. *Sedimentology* 38, 899-912.
- Williams, H., Turner, F. J., Gilbert, C. M., 1982. *Petrography: An introduction to the study of rocks in thin section*. WH Freeman and Company, San Francisco.
- Worden, R. H., Burley, S. D., 2003. Sandstone diagenesis: the evolution of sand to stone In: Burley, S. D., Worden, R. H., (Eds.), *Sandstone Diagenesis—Recent and Ancient*. Blackwell Publishing Ltd., USA, pp. 1-44.
- Worden, R. H., Morad, S., 2000. Quartz cementation in oil field sandstones: a review of the key controversies. *Quartz cementation in sandstones*. International Association of Sedimentologists Special Publications 29, 1-20.
- Worden, R. H., Morad, S., 2009. Clay minerals in sandstones: controls on formation, distribution and evolution. In: Worden, R. H., Morad, S., (Eds.), *Clay Mineral Cements in Sandstones*. International Association of Sedimentologists Special Publication 34. Blackwell Publishing, pp. 3–41.
- Worden, R. H., Smalley, P. C., Barclay, S. A., 2003. H₂S and diagenetic pyrite in North Sea sandstones: due to TSR or organic sulphur compound cracking?. *Journal of Geochemical Exploration* 78, 487-491.

Zaid, S. M., Al Gahtani, F., 2015. Provenance, diagenesis, tectonic setting, and geochemistry of Hawkesbury Sandstone (Middle Triassic), southern Sydney Basin, Australia. *Turkish Journal of Earth Sciences* 24, 72-98.

Zhong, S., Mucci, A., 1995. Partitioning of rare earth elements (REEs) between calcite and seawater solutions at 25 C and 1 atm, and high dissolved REE concentrations. *Geochimica et Cosmochimica Acta* 59, 443-453.

APPENDIX 1

Visual estimates of mineralogic composition (%) and porosity (%) of Ti-3 reservoir sandstones determined by optical microscope

Sampl es#	Ave. Grain Size (µm)	Grain Shape	Quartz* (%)	Feldspar *(%)	Lithic Fragment*(%)	Calcite Cement(%)	Pyrite(%)	Quartz Overgrowth(%)	Bioclast (%)	Porosity (%)
3327.1	very-fined grain									
3329.4	very-fined grain									
3330.1	very-fined grain									
3331.7	very-fined grain									
3332.6	very-fined grain									
3332.7	very-fined grain									
3333.2	very-fined grain									
3334.4	very-fined grain									
3335.6	40	angular- subangular	90	3	7	45	5	3	7	1
3336.6	very-fined grain									
3337.1	very-fined grain									
3337.6	very-fined grain									
3339.3	170	subangular- subrounded	83	7	10	0	13	2	10	15
3340.6	110	subangular- subrounded	88	2	10	32	4	3	7	6
3341.9	140	subangular	87	3	10	0	2	4	7	18
3342.6	180	subangular	92	2	6	40	0	2	3	2
3343.6	140	angular- subangular	86	2	12	0	2	1	9	22
3344.6	150	angular- subangular	88	3	9	47	2	2	9	1
3344.6- 2	160	angular- subangular	88	3	9	46	2	2	9	1

Sampl es#	Ave. Grain Size (µm)	Grain Shape	Quartz* (%)	Feldspar *(%)	Lithic Fragment*(%)	Calcite Cement(%)	Pyrite(%)	Quartz Overgrowth(%)	Bioclast (%)	Porosity (%)
3345.8	very-fined grain									
3346.6	very-fined grain									
3348.6	90	angular- subangular	90	4	6	5	4	1	13	8
3350.2	very-fined grain									
3351.3	100	angular- subangular	92	2	6	36	1	2	8	1
3352.5	very-fined grain									
3354.2	150	subangular- subrounded	94	2	4	0	4	3	5	18
3355.6	150	angular- subangular	85	7	8	7	6	3	3	15
3356.4	180	subangular- subrounded	91	4	5	0	3	2	8	7
3357.2	130	angular- subangular	97	1	2	40	4	3	4	1
3357.7	200	subangular- subrounded	89	1	10	0	6	4	5	20
3360.4	110	angular- subangular	91	1	8	32	2	2	12	4
3361.1	160	angular- subangular	85	5	10	0	2	3	8	14
3362.6	130	subangular- subrounded	86	3	11	0	6	2	6	17
3361.6	180	subangular- subrounded	92	1	7	0	5	3	5	15
3363.4	100	angular- subangular	86	3	11	37	1	1	7	4
3364.2	220	subangular	88	1	11	0	13	3	8	28
3365.9	300	angular- subangular	85	2	13	36	3	2	8	1
3367.8	330	subangular	92	2	6	46	4	1	6	1
3368.6	230	subangular- subrounded	91	1	8	0	17	4	7	18

Sampl es#	Ave. Grain Size (µm)	Grain Shape	Quartz* (%)	Feldspar *(%)	Lithic Fragment*(%)	Calcite Cement(%)	Pyrite(%)	Quartz Overgrowth(%)	Bioclast (%)	Porosity (%)
3369.4	180	angular- subangular	84	2	14	33	4	2	10	2
3369.9	220	angular- subangular	85	1	14	26	5	1	15	3
3371.1	240	subangular- subrounded	86	4	10	46	9	0	13	2
3372.5	240	angular- subangular	87	1	12	34	3	1	7	1
3374	350	angular- subangular	85	1	14	32	2	0	7	1
3375	220	angular- subangular	77	7	16	28	5	2	12	1
3375	230	angular- subangular	79	5	16	34	6	1	15	1
3375.8 5	320	subangular	79	1	20	34	5	1	16	10
3377.1	270	subangular	94	1	5	0	10	5	9	20
3377.9	310	subangular- subrounded	88	1	11	37	1	3	8	7
3379.7	300	subangular- subrounded	82	1	17	42	2	2	9	3
3381.1	320	subangular	81	1	18	40	2	6	11	2
3382.2	230	subangular- subrounded	79	1	20	3	2	2	6	17
3382.8	280	subangular	89	3	8	41	2	3	10	2
3383.4	320	subangular	83	1	16	39	2	2	8	7
3384.5	160	angular- subangular	72	10	18	19	13	0	13	12
3384.8	170	subangular	69	7	24	39	2	2	10	3
3385.7	230	subangular	74	10	16	40	3	1	9	2
3386.5	220	angular- subangular	69	8	23	41	1	1	11	1
3387.4	210	subangular	87	3	10	0	2	5	10	20

Sampl es#	Ave. Grain Size (µm)	Grain Shape	Quartz* (%)	Feldspar *(%)	Lithic Fragment*(%)	Calcite Cement(%)	Pyrite(%)	Quartz Overgrowth(%)	Bioclast (%)	Porosity (%)
3387.8	210	subangular- subrounded	81	4	15	0	5	7	7	23
3388.9	very-fined grain									
3389.6	very-fined grain									

Note: Quartz* + Feldspar* + Lithic Fragment* =100%

APPENDIX 2

Fluid inclusion microthermometric measurements of calcite cement in Ti-3 sandstones

Sample#	Host mineral	Occurrence	T_h °C	T_l °C	T_m °C	Eq.wt% NaCl (Bodnar, 2003)
Monophase1	Poikilotopic Calcite	Cluster			-0.3	0.53
Monophase2	Poikilotopic Calcite	Cluster		-40.3	-0.3	0.53
Monophase3	Poikilotopic Calcite	Cluster		-42.2	-0.4	0.70
Monophase4	Poikilotopic Calcite	Cluster			-0.5	0.88
Monophase5	Poikilotopic Calcite	Cluster			-0.6	1.05
Monophase6	Poikilotopic Calcite	Cluster			-0.7	1.22
Monophase7	Poikilotopic Calcite	Cluster		-47.9	-0.7	1.22
Monophase8	Poikilotopic Calcite	Cluster			-0.9	1.57
Monophase9	Poikilotopic Calcite	Cluster			-0.9	1.57
Monophase10	Poikilotopic Calcite	Cluster		-45.8	-1	1.74
Monophase11	Poikilotopic Calcite	Cluster			-1.3	2.24
Monophase12	Poikilotopic Calcite	Cluster		-48.3	-1.5	2.57
Monophase13	Poikilotopic Calcite	Cluster			-1.5	2.57
Monophase14	Poikilotopic Calcite	Cluster			-1.6	2.74
Monophase15	Poikilotopic Calcite	Cluster			-1.7	2.90
Monophase16	Poikilotopic Calcite	Cluster		-50.6	-1.9	3.23
Monophase17	Poikilotopic Calcite	Cluster			-2	3.39
Monophase18	Poikilotopic Calcite	Cluster		-33.8	-2	3.39
Monophase19	Poikilotopic Calcite	Cluster		-38.7	-2.1	3.55
Monophase20	Poikilotopic Calcite	Cluster			-2.6	4.34
Monophase21	Poikilotopic Calcite	Cluster			-2.7	4.49
Monophase22	Poikilotopic Calcite	Cluster			-2.7	4.49
Monophase23	Poikilotopic Calcite	Cluster		-47.4	-2.8	4.65
Monophase24	Poikilotopic Calcite	Cluster			-3	4.96
Monophase25	Poikilotopic Calcite	Cluster			-3	4.96
Monophase26	Poikilotopic Calcite	Cluster			-3.2	5.26
Monophase27	Poikilotopic Calcite	Cluster			-4	6.45
Monophase28	Poikilotopic Calcite	Cluster			-4	6.45
33446-T1	Poikilotopic Calcite	Individual	64.8	-34.7	-4.5	7.17
33446-T2	Poikilotopic Calcite	Individual	68.2		-4.6	7.31
33446-T3	Poikilotopic Calcite	Individual	65.2	-55.2	-5.1	8.00
33446-T4	Poikilotopic Calcite	Individual	63.9			
33572-T1	Poikilotopic Calcite	Individual	76.4			
33572-T2	Poikilotopic Calcite	Individual	75.9			

Sample#	Host mineral	Occurrence	T_h °C	T_i °C	T_m °C	Eq.wt% NaCl (Bodnar, 2003)
33572-T3	Poikilotopic Calcite	Individual	75.3			
33572-T4	Poikilotopic Calcite	Individual	76.2			
33678-T1	Poikilotopic Calcite	Individual	75.3			
33678-T2	Poikilotopic Calcite	Individual	66.3		-5.4	8.41
33678-T3	Poikilotopic Calcite	Individual	73.8			
33678-T4	Poikilotopic Calcite	Individual	68.7		-5.8	8.95
33678-T5	Poikilotopic Calcite	Individual	74.7	-46.3	-5.2	8.14
33678-T6	Poikilotopic Calcite	Individual	65.7		-5.3	8.28
3374-T1	Poikilotopic Calcite	Individual	83.1			
3374-T2	Poikilotopic Calcite	Individual	71.1	-45.2	-5.5	8.55
3374-T3	Poikilotopic Calcite	Individual	80.4			
3374-T4	Poikilotopic Calcite	Individual	64.1			
3374-T5	Poikilotopic Calcite	Individual	76.7	-53.7	-5.9	9.08
3374-T6	Poikilotopic Calcite	Individual	72.9		-6	9.21
33779-T1	Poikilotopic Calcite	Individual	66.4	-38.6	-6.9	10.36
33779-T2	Poikilotopic Calcite	Individual	77.2			
33779-T3	Poikilotopic Calcite	Individual	80.8	-53.2	-7.2	10.73
33779-T4	Poikilotopic Calcite	Individual	72			
33779-T5	Poikilotopic Calcite	Individual	67.8			
33779-T6	Poikilotopic Calcite	Individual	73.3		-7.6	11.22
33779-T7	Poikilotopic Calcite	Individual	76.6			
Fracture-T1	Fracture-filling Calcite	Individual	92	-48.3	-5.8	8.95
Fracture-T2	Fracture-filling Calcite	Individual	135	-53.9	-5.3	8.28
Fracture-T3	Fracture-filling Calcite	Individual	117.6			
Fracture-T4	Fracture-filling Calcite	Individual	138.1			
Fracture-T5	Fracture-filling Calcite	Individual	89.4		-5.3	8.28
Fracture-T6	Fracture-filling Calcite	Individual	133.2	-50.6	-9.3	13.18
Fracture-T7	Fracture-filling Calcite	Individual	76.4			
Fracture-T8	Fracture-filling Calcite	Individual	75.3			
Fracture-T9	Fracture-filling Calcite	Individual	91.6	-46.5	-5.5	8.55
Fracture-T10	Fracture-filling Calcite	Individual	105.6			

Sample#	Host mineral	Occurrence	T_h °C	T_i °C	T_m °C	Eq.wt% NaCl (Bodnar, 2003)
Fracture-T11	Fracture-filling Calcite	Individual	84.7			
Fracture-T12	Fracture-filling Calcite	Individual	122.3		-6	9.21
Fracture-T13	Fracture-filling Calcite	Individual	76.2			
Fracture-T14	Fracture-filling Calcite	Individual	75.9			
Fracture-T15	Fracture-filling Calcite	Individual	97.3	-52.4	-7.8	11.46
Fracture-T16	Fracture-filling Calcite	Individual	105.1		-8.3	12.05

APPENDIX 3

Quantitative fluid-inclusion gas analysis of individual crushes for calcite cement of Ti-3 sandstones

Sample 33448									Weighted Mean
Crush#	9360a	9360b	9360c	9360d	9360e	9360f	9360g	9360h	
H ₂	0.013	0.014	0.017		0.014	0.027	0.029	0.027	0.021
He	0.000	0.000	0.000		0.000	0.001	0.000	0.001	0.000
CH ₄	2.229	3.120	2.693		1.861	3.283	2.806	3.108	2.718
H ₂ O	95.196	92.948	94.060		94.897	91.696	92.734	92.768	93.405
N ₂	0.453	0.746	0.696		0.568	1.086	0.765	0.817	0.744
O ₂	0.000	0.000	0.000		0.001	0.000	0.000	0.001	0.000
Ar	0.006	0.009	0.000		0.008	0.011	0.010	0.010	0.008
CO ₂	1.128	1.965	1.267		1.251	2.112	1.853	1.448	1.564

Sample 33445									Weighted Mean
Crush#	9361a	9361b	9361c	9361d	9361e	9361f	9361g	9361h	
H ₂	0.002	0.007	0.011	0.024	0.038	0.038	0.052	0.084	0.032
He	0.000	0.000	0.000	0.000	0.001	0.000	0.000	0.001	0.000
CH ₄	0.947	2.083	0.952	2.123	2.810	1.402	1.402	1.883	1.751
H ₂ O	95.357	92.479	94.418	91.564	89.596	93.691	93.113	92.264	92.599
N ₂	0.448	0.778	0.632	0.868	0.941	0.668	0.617	0.827	0.739
O ₂	0.004	0.000	0.059	0.001	0.000	0.003	0.006	0.002	0.009
Ar	0.006	0.011	0.009	0.010	0.015	0.009	0.010	0.010	0.010
CO ₂	2.687	3.756	3.033	4.200	5.219	3.241	3.671	3.841	3.804

Sample 33678									Weighted Mean
Crush#	9362a	9362b	9362c	9362d	9362e	9362f	9362g	9362h	
H ₂	0.039	0.122	0.061	0.019	0.047	0.087	0.082	0.120	0.074
He	0.000	0.001	0.000	0.000	0.001	0.000	0.001	0.001	0.001
CH ₄	3.550	5.491	1.916	6.455	3.763	4.879	4.358	6.269	4.858
H ₂ O	87.028	83.827	90.540	87.929	89.719	87.462	86.652	83.599	87.079
N ₂	2.048	2.122	0.670	0.626	0.693	0.934	1.618	1.534	1.158
O ₂	0.067	0.066	0.013	0.000	0.000	0.021	0.021	0.016	0.018
Ar	0.023	0.032	0.017	0.013	0.017	0.019	0.027	0.030	0.022

CO ₂	6.201	6.194	5.552	3.772	4.094	5.199	5.264	5.766	5.036
-----------------	-------	-------	-------	-------	-------	-------	-------	-------	-------

Sample 33779									Weighted Mean
Crush#	9363a	9363b	9363c	9363d	9363e	9363f	9363g	9363h	
H ₂	0.031	0.045	0.039	0.042	0.111	0.075	0.086	0.083	0.065
He	0.000	0.000	0.000	0.000	0.000	0.000	0.001	0.001	0.000
CH ₄	1.442	2.006	1.476	1.532	2.282	2.848	6.478	3.466	2.825
H ₂ O	94.916	92.402	94.941	92.767	90.842	90.778	87.091	90.776	91.807
N ₂	0.507	0.641	0.324	0.809	0.884	0.630	1.082	0.798	0.702
O ₂	0.010	0.007	0.006	0.011	0.037	0.000	0.009	0.007	0.009
Ar	0.007	0.007	0.006	0.011	0.015	0.014	0.014	0.014	0.011
CO ₂	2.385	4.330	2.501	4.276	5.142	3.982	4.179	3.235	3.518

Sample 33797									Weighted Mean
Crush#	9364a	9364b	9364c	9364d	9364e	9364f	9364g	9364h	
H ₂	0.188	0.066	0.090	0.059	0.030	0.119			0.091
He	0.000	0.000	0.000	0.001	0.000	0.001			0.000
CH ₄	6.906	5.869	4.900	9.290	6.668	3.296			6.429
H ₂ O	85.380	80.936	77.888	81.032	84.666	85.547			83.285
N ₂	1.174	1.411	1.629	1.162	0.491	0.918			1.025
O ₂	0.024	0.005	0.011	0.060	0.013	0.042			0.025
Ar	0.014	0.034	0.041	0.019	0.009	0.025			0.020
CO ₂	5.422	8.572	12.242	7.645	7.635	8.732			7.804

Sample 33811									Weighted Mean
Crush#	9365a	9365b	9365c	9365d	9365e	9365f	9365g	9365h	
H ₂	0.000	0.000	0.000	0.000	0.003	0.000	0.000	0.002	0.000
He	0.000	0.000	0.000	0.000	0.000	0.000	0.000	0.000	0.000
CH ₄	0.282	0.164	0.199	0.202	0.138	0.203	0.497	0.685	0.282
H ₂ O	98.348	99.105	98.400	98.345	99.289	99.267	98.206	98.237	98.533
N ₂	0.143	0.087	0.131	0.114	0.087	0.069	0.252	0.162	0.129
O ₂	0.067	0.031	0.057	0.055	0.007	0.007	0.017	0.012	0.042
Ar	0.003	0.001	0.002	0.002	0.001	0.001	0.003	0.001	0.002
CO ₂	0.681	0.450	0.827	0.807	0.290	0.378	0.915	0.800	0.696

APPENDIX 4

Trace element analysis results of calcite cement by SIMS

Sample#	SIMS Spot	Fe(ppm)	Mn(ppm)	Sr(ppm)	
Sample 3344.6	A-1	120.05	595.51	498.55	
	A-2	68.37	568.45	1113.69	
	B-1	322.80	617.36	453.96	
	B-2	77.54	818.72	444.34	
	B-3	397.06	652.60	754.05	
	C-1	36.55			
	C-2	149.62			
	C-3	41.08			
	D-1	176.68			
	D-2	38.62			
	D-3	42.66			
	Sample 3367.8	A-1	32.53	359.83	1620.84
		A-2	47.40	294.91	1746.82
A-3		46.71	321.69	1771.36	
A-4		51.58	373.47	1759.08	
B-1		41.55			
B-2		37.83			
B-3		27.66			
B-4		29.98			
B-5		35.85			
C-1		33.27			
C-2		57.62			
Sample 3371.1		A-1	224.90	180.60	2260.06
		A-2	157.20	243.00	786.10
	B-1	90.36			
	B-2	201.60			
	B-3	103.96			
	B-4	64.86			
	C-1	138.25	235.37	640.06	
	C-2	78.56	194.73	1395.75	
	D-1	62.39			
	D-2	43.82			
	E-1	208.40	255.53	645.17	
	F-1	82.57			
	F-2	99.21			
Sample 3379.1	A-1	314.70	55.15	1851.23	

Sample#	SIMS Spot	Fe(ppm)	Mn(ppm)	Sr(ppm)
	A-2	278.25	54.18	1910.37
	A-3	250.07	55.14	1963.54
	B-1	493.59		
	B-2	166.27		
	C-1	125.08	77.34	446.08
	C-2	134.85	64.58	1324.84
	C-3	151.69	58.59	1933.97
	D-1	387.68		
	D-2	145.28		
	D-3	70.01		
	D-4	254.66		
	D-5	104.00		
	D-6	186.21		
	D-7	451.95		
	D-8	83.36		
Sample 3386.5	A-1	64.74	1629.66	1863.67
	A-2	88.50	1768.73	987.55
	A-3	126.49	1021.77	2217.55
	A-4	46.38	1689.09	675.95
	B-1	45.79		
	B-2	37.76		
	B-3	41.56		
	B-4	33.62		
	B-5	73.78		
	B-6	44.12		

Standard	Fe(ppm)	Mn(ppm)	Sr(ppm)
oka c 1 Dec 5 2013	337.5	2340.2	13920.3
oka c 2 Dec 5 2013	343.6	2317.2	14219.1
oka_c@1	306.6	2307.0	14337.8
oka_c@2	317.5	2289.4	13751.9
oka_c@3	352.0	2308.8	13922.6
oka c1 Dec 6 2013	341.1	2086.6	14298.0
oka c2 Dec 6 2013	338.6	2544.9	13591.0
oka_c_1_Aug_26_2014@1	394.5	2348.1	14857.5
oka_c_1_Aug_26_2014@2	361.2	2319.6	13718.9
oka_c_1_Aug_26_2014@3	324.1	2304.4	14171.9

APPENDIX 5

REE concentrations of calcite cement of Ti-3 sandstones

Samples#	SIMS Spot	La (ppm)	Ce (ppm)	Nd (ppm)	Sm (ppm)	Eu (ppm)	Dy (ppm)	Er (ppm)	Yb (ppm)	Σ Total REE (ppm)
Sample 3344.6	A-1	5.04	7.80	3.64	0.82	0.29	0.35	0.05	0.11	18.09
	A-2	2.83	5.85	3.22	0.82	0.32	0.53	0.03	0.19	13.80
	A-3	1.87	3.38	2.05	0.55	0.18	0.26	0.10	0.06	8.45
	B-1	2.09	4.54	2.96	0.58	0.29	0.58	0.20	0.10	11.33
	B-2	2.81	6.46	3.87	1.23	0.35	0.63	0.18	0.13	15.67
	B-3	5.82	10.30	4.95	1.21	0.43	0.62	0.29	0.11	23.72
Sample 3367.8	A-1	0.37	1.02	0.84	0.28	0.06	0.14	na	0.04	2.76
	A-2	0.46	1.29	1.16	0.35	0.08	0.10	0.03	0.02	3.49
	A-3	0.25	1.02	0.75	0.35	0.05	0.14	na	0.02	2.58
	A-4	0.88	1.94	1.18	0.38	0.08	0.12	0.05	0.04	4.68
	B-1	0.35	1.29	0.94	0.18	0.04	0.08	0.01	na	2.88
	B-2	0.79	1.50	1.08	0.35	0.10	0.09	0.03	0.04	3.98
Sample 3371.1	B-3	0.54	1.45	1.01	0.31	0.07	0.13	0.01	0.01	3.52
	A-1	1.66	1.22	0.80	0.23	0.06	0.17	0.11	0.09	4.34
	A-3	1.02	0.69	0.55	0.25	0.12	0.19	0.04	0.04	2.89
	B-1	1.88	3.86	2.26	0.84	0.26	0.42	0.15	0.12	9.78
	B-2	2.91	5.93	3.52	0.75	0.23	0.32	0.16	0.17	13.99
	C-1	0.35	0.67	0.72	0.31	0.05	0.12	0.05	0.05	2.32
	C-2	1.58	2.43	1.65	0.32	0.11	0.15	0.07	0.04	6.34
	D-1	8.94	18.97	10.00	2.88	0.80	1.50	0.59	0.69	44.36
	D-2	6.21	13.74	7.50	2.59	0.67	1.64	0.60	0.61	33.58
	D-3	8.30	16.60	7.70	2.27	0.67	1.39	0.48	0.47	37.89
E-1	1.15	2.75	2.43	0.69	0.21	0.40	0.12	0.09	7.85	
E-2	1.11	2.72	2.54	0.57	0.15	0.22	0.15	0.07	7.53	

Samples#	SIMS Spot	La (ppm)	Ce (ppm)	Nd (ppm)	Sm (ppm)	Eu (ppm)	Dy (ppm)	Er (ppm)	Yb (ppm)	Σ Total REE (ppm)
Sample 3379.1	E-3	2.00	2.94	1.70	0.42	0.14	0.23	0.07	0.10	7.60
	E-4	0.35	0.85	0.67	0.39	0.08	0.10	0.04	0.05	2.52
	A-1	0.77	1.76	1.13	0.39	0.12	0.20	0.04	0.10	4.52
	A-2	1.14	2.47	1.66	0.53	0.20	0.28	0.07	0.11	6.46
	C-1	3.03	4.69	2.78	0.77	0.17	0.34	0.15	0.07	12.00
	C-2	0.43	0.89	0.82	0.23	0.08	0.12	0.02	0.03	2.62
	D-1	1.01	2.22	2.11	0.88	0.21	0.47	0.04	0.14	7.08
	D-2	1.54	3.43	2.60	0.83	0.49	0.33	0.01	0.15	9.39
	E-1	0.71	1.30	1.09	0.25	0.08	0.13	0.54	0.04	4.14
	E-2	0.99	1.88	1.31	1.30	0.12	0.20	0.06	0.07	5.94
Sample 3386.5	E-3	0.67	1.41	0.89	0.42	0.08	0.15	0.21	0.02	3.85
	E-4	1.30	2.25	1.36	0.43	0.13	0.17	0.04	0.06	5.73
	A-1	0.15	0.21	0.08	0.02	na	na	na	na	0.46
	A-2	0.12	0.22	0.13	na	na	na	na	na	0.48
	B-1	0.53	1.15	1.01	0.21	0.07	0.09	0.07	na	3.13
	B-2	0.81	1.26	0.65	0.14	0.03	0.02	na	na	2.91
	C-1	0.24	0.30	0.23	0.16	0.04	0.06	0.06	0.04	1.12
	D-1	1.04	1.71	1.02	0.26	0.07	0.12	0.02	0.04	4.26
	D-2	1.79	3.92	1.96	0.55	0.19	0.41	0.13	0.12	9.06

Note: "na" means concentration that cannot be detected

Standard	La (ppm)	Ce (ppm)	Nd (ppm)	Sm (ppm)	Eu (ppm)	Dy (ppm)	Er (ppm)	Yb (ppm)
oka_c_Jan_22_2014@1	448.42	532.24	148.80	21.51	8.65	5.12	1.92	2.44
oka_c_Jan_22_2014@2	447.92	533.87	152.49	22.16	10.04	4.83	2.22	2.96
oka_c_Jan_22_2014@3	445.36	522.91	145.66	20.20	9.88	5.23	2.24	2.70
oka_c_Jan_22_2014@5	434.65	513.65	143.76	20.85	9.37	4.79	2.06	2.77
oka_c_Jan_22_2014@6	438.72	517.73	146.75	20.21	9.33	4.59	2.26	2.61
oka_c_Jan_23_2014@3	436.95	518.88	140.06	20.64	7.94	5.09	2.13	2.66
oka_c_Jan_23_2014@2	438.89	530.30	139.43	20.94	9.27	5.06	2.15	2.92
oka_c_Jan_27_2014@3	451.77	534.83	150.67	19.93	8.76	4.90	2.13	2.62
oka_c_Jan_27_2014@2	447.74	534.56	147.26	20.90	8.92	5.43	2.38	2.76
oka_c_aug_27_2014@2	440.12	521.83	146.31	22.42	8.48	4.93	2.02	2.46
oka_c_aug_27_2014@1	445.08	532.29	150.59	22.38	8.60	5.16	2.03	2.25
oka c 2 Aug 28 2014	460.83	542.33	142.18	22.15	7.52	5.13	2.17	2.47
oka c 1 Aug 28 2014	425.57	503.55	134.90	19.75	10.78	4.92	2.35	2.48
oka_c_Sept_4_2014@3	441.75	522.08	149.24	21.26	8.54	4.75	2.11	2.28
oka_c_Sept_4_2014@4	442.93	528.27	153.79	21.65	8.68	5.41	2.22	2.55
oka_c_Sept_4_2014@5	444.02	524.66	149.39	21.77	9.01	5.32	2.28	2.79
oka c 2 Sept 5 2014	442.90	525.00	144.34	21.34	8.90	4.94	2.44	2.51